

University of Windsor

Scholarship at UWindor

Electronic Theses and Dissertations

Theses, Dissertations, and Major Papers

2009

Analysis of Second-Phase Particle Fracture in Hypereutectic Aluminum-Silicon Alloys

Sandeep Bhattacharya
University of Windsor

Follow this and additional works at: <https://scholar.uwindsor.ca/etd>

Recommended Citation

Bhattacharya, Sandeep, "Analysis of Second-Phase Particle Fracture in Hypereutectic Aluminum-Silicon Alloys" (2009). *Electronic Theses and Dissertations*. 175.
<https://scholar.uwindsor.ca/etd/175>

This online database contains the full-text of PhD dissertations and Masters' theses of University of Windsor students from 1954 forward. These documents are made available for personal study and research purposes only, in accordance with the Canadian Copyright Act and the Creative Commons license—CC BY-NC-ND (Attribution, Non-Commercial, No Derivative Works). Under this license, works must always be attributed to the copyright holder (original author), cannot be used for any commercial purposes, and may not be altered. Any other use would require the permission of the copyright holder. Students may inquire about withdrawing their dissertation and/or thesis from this database. For additional inquiries, please contact the repository administrator via email (scholarship@uwindsor.ca) or by telephone at 519-253-3000ext. 3208.

**ANALYSIS OF SECOND-PHASE PARTICLE FRACTURE
IN HYPEREUTECTIC ALUMINUM-SILICON ALLOYS**

by

SANDEEP BHATTACHARYA

A Thesis

**Submitted to the Faculty of Graduate Studies
through Engineering Materials
in Partial Fulfillment of the Requirements for
the Degree of Master of Applied Science at the
University of Windsor**

Windsor, Ontario, Canada

2009

© 2009 Sandeep Bhattacharya

**ANALYSIS OF SECOND-PHASE PARTICLE FRACTURE
IN HYPEREUTECTIC ALUMINUM-SILICON ALLOYS**

by

Sandeep Bhattacharya

APPROVED BY:

Outside Program Reader **Dr. A. Fartaj** (Mechanical Engineering),
Department of Mechanical, Automotive and
Materials Engineering.

Program Reader **Dr. A. Edrisy** (Engineering Materials),
Department of Mechanical, Automotive and
Materials Engineering.

Co-Advisors **Dr. A. T. Alpas** (Engineering Materials),
Department of Mechanical, Automotive and
Materials Engineering.

Dr. A. R. Riahi (Engineering Materials),
Department of Mechanical, Automotive and
Materials Engineering.

Chair of Defense **Dr. V. Stoilov** (Engineering Materials),
Department of Mechanical, Automotive and
Materials Engineering.

25 May 2009

AUTHOR'S DECLARATION OF ORIGINALITY

I hereby certify that I am the sole author of this thesis and that no part of this thesis has been published or submitted for publication.

I certify that, to the best of my knowledge, my thesis does not infringe upon anyone's copyright nor violate any proprietary rights and that any ideas, techniques, quotations, or any other material from the work of other people included in my thesis, published or otherwise, are fully acknowledged in accordance with the standard referencing practices. Furthermore, to the extent that I have included copyrighted material that surpasses the bounds of fair dealing within the meaning of the Canada Copyright Act, I certify that I have obtained a written permission from the copyright owner(s) to include such material(s) in my thesis and have included copies of such copyright clearances to my appendix.

I declare that this is a true copy of my thesis, including any final revisions, as approved by my thesis committee and the Graduate Studies office, and that this thesis has not been submitted for a higher degree to any other University or Institution.

ABSTRACT

Vickers micro-indentation tests were performed on second-phase particles of Al-18.5wt.%Si and results were compared with those of monolithic silicon. Damage microstructures beneath indented second-phase silicon particles were studied to determine the crack morphologies causing particle fracture, and also to identify the role of indentation-induced phase transformations on subsurface damage. Plastic deformation at low loads and volume expansion due to subsurface crack formation at high loads (>650 mN) were responsible for pile-up formations around the indentations. The probability of lateral cracks reaching the surface and causing particle fracture was shown to obey Weibull statistics with a low modulus. Diamond cubic Si-I transformed into bcc Si-III and rhombohedral Si-XII, under an estimated indentation pressure of 19.3 GPa. Cross-sectional FIB and TEM revealed a semi-circular plastic core and subsurface lateral crack pattern below the residual indents, in addition to a localized, amorphous silicon zone below the plastic core at the median crack edges.

DEDICATION

To my parents,

Kishore and Anuroma Bhattacharya

and to my sisters,

Sanjukta and Sudeshna Bhattacharya

for their love, unfailing support and encouragement.

ACKNOWLEDGEMENTS

My sincerest thanks and gratitude to Dr. A. T. Alpas for his supervision and valuable suggestions that guided me in this research for my M.A.Sc. at the University of Windsor, to Dr. A. R. Riahi for his valuable advice, constant help, support and encouragement in the most challenging times of this research.

Sincere thanks to my committee members, Dr. A. Fartaj and Dr. A. Edrisy, for their helpful suggestions. Dr. R. F. Aroca and Dr. N. P. W. Pieczonka's help with micro-Raman spectroscopy and Dr. X. Meng-Burany's contribution to discussions on TEM analyses are greatly appreciated. Technical help from Mr. John Robinson and Mr. Al Ditchburn is greatly acknowledged.

I appreciate all researchers of the NSERC/General Motors of Canada/University of Windsor Industrial Research Chair in Tribology of Lightweight Materials, for their help, constant support and encouragement.

Sincere thanks to the Natural Sciences and Engineering Research Council of Canada (NSERC) and General Motors of Canada Ltd. for their financial support.

TABLE OF CONTENTS

AUTHOR'S DECLARATION OF ORIGINALITY	iii
ABSTRACT	iv
DEDICATION	v
ACKNOWLEDGEMENTS	vi
NOMENCLATURE	xi
LIST OF FIGURES	xii
LIST OF TABLES	xxv
CHAPTER 1: Introduction	1
1.1. Background of this Research	1
1.2. Scope of this Work.....	3
1.3. Objective of Current Research.....	4
1.4. Organization of this Thesis	4
CHAPTER 2: Literature Survey	7
2.1. Introduction to this survey	7
2.2. Static Hardness.....	7
2.3. Indentation Stress Fields	9
2.3.1. Nature of Stress Distribution due to a Point Force; Boussinesq Solution	9
2.3.2. Hertzian Stress Distribution due to a Spherical Indenter	11
2.3.3. Comparison between the Boussinesq and Hertzian Fields	12
2.4. Onset of Plastic Deformation.....	13
2.5. The Indentation Experiment	14

2.5.1. Loading and Unloading Curves; Oliver and Pharr Model	14
2.5.2. Work of Indentation	15
2.5.3. ‘Sinking-in’ and ‘Piling-up’ Phenomena	16
2.6. Indentation Fracture Mechanics	17
2.6.1. Criteria for Crack Formation	17
2.6.2. Basic Indentation Fracture Systems	19
2.6.3. Blunt Indenter	20
2.6.4. Sharp Indenter	21
2.6.5. Indentation Fracture Toughness (K_{IC}); the Crack-Length Method	23
2.7. Vickers Indentation and Associated Elastic/Plastic Indentation Damage	26
2.8. Deformation and Fracture of Silicon in Al-Si Alloys during Sliding Contact	27
2.9. Statistical Analysis of Fracture: Weibull Modeling	28
2.9.1. Functional Deduction of Weibull’s Formula	29
2.9.2. Application of Weibull Modeling to Material Failure	34
2.10. Deformation-induced Phase Transformation in Silicon	35
2.11. Dislocation Mobility in Diamond Cubic (DC) Structure	36
2.11.1. Microhardness-induced Dislocation Generation	40
2.11.2. Investigation of Indentation Defect Structure in Silicon	41
2.12. Temperature-induced Phase Transformations in Silicon	42
2.12.1. High Temperature Deformation of Silicon due to Indentation	44
2.13. A Short Summary of the Literature Survey	44
CHAPTER 3: Experimental	74
3.1. Description and Preparation of Samples	74
3.1.1. Al-18.5wt.%Si Alloy	74
3.1.2. Monocrystalline Silicon Wafer	74
3.2. Microhardness Experiments	75

3.3. Calculation of Indentation Fracture Toughness: Measurements using the Crack-length Method	76
3.4. Temperature-induced Phase Transformation in Silicon Particles: Preparation of Encapsulated Al-Si Samples	77
3.5. Raman Micro-spectroscopy	78
3.6. Preparation of FIB-milled Cross-sectional Samples.....	78
CHAPTER 4: Results	91
4.1. Indentation Surface Morphology and Phenomenological Description of Silicon Particle Fracture	91
4.1.1. Pile-up formation due to Plastic Deformation and Lateral Crack formation..	91
4.1.2. Statistical Nature of Indentation Fracture	93
4.2. Subsurface Damage and Indentation Crack Patterns	94
4.3. Micro-Raman Spectroscopy of Residual Indentation Impressions.....	95
4.3.1. Results of Room Temperature Phase Transformations in Silicon Particles ...	95
4.3.2 Effect of Temperature on Phase Transformation in Silicon Particles.....	95
CHAPTER 5: Discussions	111
5.1. Comparison of Material Properties of Different Second Phases in Al-18.5wt.%Si with Monolithic Silicon: Weibull Statistical Analysis.....	111
5.1.1. Comparison of Hardness Values.....	111
5.1.2. Comparison of the Fracture Toughness (K_{IC}) Values.....	112
5.2. Pressure-induced Phase Transformations in Silicon Particles	112
5.3. Analysis of Subsurface Damage Mechanisms.....	114
CHAPTER 6: Summary and Conclusions.....	129
6.1. Summary	129

6.2. Conclusions.....	131
6.3. Future Work.....	132
REFERENCES.....	134
APPENDIX.....	142
VITA AUCTORIS	144

NOMENCLATURE

Abbreviations

DC	Diamond Cubic
BCC	Body Centered Cubic
FIB	Focused Ion Beam
LMIS	Liquid Metal Ion Source
SEM	Scanning Electron Microscope
ESEM	Environmental Scanning Electron Microscope
TEM	Transmission Electron Microscope
HRTEM	High Resolution Transmission Electron Microscope
SAED	Selected Area Electron Diffraction
FFT	Fast Fourier Transform
a-Si	Amorphous silicon

Symbols

σ	Principal stress
ν	Poisson's ratio
Ψ	Semi-angle of Vickers indenter
E	Elastic modulus
E^*	Modified elastic modulus
Y	Yield strength
H	Hardness
h_f	Penetration depth at complete unloading during indentation
h_m	Maximum penetration depth during indentation
h_c	The contact depth
S	Initial unloading slope of an indentation load vs. penetration depth curve
K_{IC}	Indentation fracture toughness
$P_f(L)$	Probability of fracture of silicon at load, L
m	Weibull modulus
P_m	Mean pressure on a symmetrical indent plastic core
c	Plastic core radius
α	Material constant signifying plastic work dissipated to heat
Si-I	Diamond cubic silicon

LIST OF FIGURES

CHAPTER 2

Fig.2.1	46
Elastic contact pressure distributions for various indentation systems; (a) point load, (b) sharp indenter, (c) flat punch, (d) sphere (or cylinder). P and a characterize the extent of applied loading and resulting contact respectively [13].	
Fig.2.2	47
Coordinate system for axially symmetric point loading, P . Expressions for the stress components indicated are given in the Appendix (p-138) [14].	
Fig.2.3	48
Half-surface view (top) and side view (bottom) of stress trajectories in Boussinesq field. Plotted for $\nu = 0.25$ [14].	
Fig.2.4	49
Contours of principal normal stresses, (a) σ_{11} , (b) σ_{22} , and (c) σ_{33} , in Boussinesq field, shown in plane containing contact axis. Plotted for $\nu = 0.25$. Unit of stress is p_o , contact “diameter” (arrowed) AA is $2a\sqrt{\alpha}$. Sharp minimum in σ_{11} and zero in σ_{22} are indicated by broken lines in (a) and (b) respectively [14].	
Fig.2.5	50
Angular variation of principal stress components in Boussinesq field, plotted in terms of dimensionless function $f(\phi)$ (Eq.2.6) (a) Principal normal stresses, σ_{11} , σ_{22} , and σ_{33} ; (b) Maximum principal shear stress σ_{13} or σ_{12} (broken line), and hydrostatic compression, p . Plotted for $\nu = 0.25$ [14].	

Fig.2.6	51
Pressure distribution over circle of contact when a flat surface is deformed elastically by a sphere [15].	
Fig.2.7	52
Elastic deformation of a flat surface by a sphere: the area of contact, A , is proportional to $w^{\frac{2}{3}}$ and the mean pressure P_m over the region of the contact is proportional to $w^{\frac{1}{3}}$ [15].	
Fig.2.8	53
Half-surface view (top) and side view (bottom) of stress trajectories in Hertzian field. Plotted for $\nu = 0.33$, contact diameter AA is $2a$ [19].	
Fig.2.9	54
Contours of principal normal stresses, (a) σ_{11} , (b) σ_{22} , and (c) σ_{33} , in Hertzian field, shown in plane containing contact axis. Plotted for $\nu = 0.33$. Unit of stress is p_o , contact diameter AA is $2a$ [19].	
Fig.2.10	55
Comparison of $\sigma_{\theta\theta}(z)$ stress terms for Boussinesq and Hertzian stress fields. Plotted for $\nu = 0.25$. Divergence of curves in vicinity of contact zone is observed (at $z \rightarrow 0$, $\sigma_{\theta\theta} \rightarrow \infty$ in the Boussinesq field, $\sigma_{\theta\theta} \rightarrow -1.125 p_o$ in the Hertzian field) [14].	
Fig.2.11	56
Elastic deformation of a flat surface by a sphere, showing the maximum shear stress in the bulk material below the deformed surface. The maximum shear stress occurs below the below the centre of the circle of contact has a value of $0.47P_{mean}$, where P_{mean} is the mean pressure. Plastic deformation first occurs at this point when the shear stress = $0.5Y$, i.e., when $P_{mean} \approx 1.1Y$, where Y is the yield stress of the material [15].	

Fig.2.12	57
Plastic deformation of an ideally plastic metal by a spherical indenter: (a) the onset occurs at a localized region Z when $p_o \approx 1.1Y$; (b) at a later stage the whole of the material around the indenter flows plastically [15].	
Fig.2.13	57
A schematic representation of a section through an indentation showing various quantities; P = the applied load; h = total displacement (Eq.2.16); h_c = the contact depth; h_s = the displacement of the surface at the perimeter of the contact; h_f = the final depth of the residual hardness impression, a = the contact radius [17].	
Fig.2.14	58
Schematic representation of load-displacement data for an indentation experiment [17]	
Fig.2.15	58
Definition of reversible work, W_u , irreversible work, W_p , and total work, W_{tot} [18]	
Fig.2.16	59
Schematic illustration of conical indentation with definition of terms [18].	
Fig.2.17	60
Illustration of the displacement incompatibility between the matrix and the inclusion, (a) before deformation, and, (b) after deformation of the matrix [11].	
Fig.2.18	60
Schematics of the energy and stress criterion for void nucleation [11].	
Fig.2.19	61
The two basic indentation fracture systems. (a) Cone crack system associated with a blunt indenter, and (b) median crack system associated with a sharp indenter [13].	

Fig.2.20	62
Hertzian cone crack in soda-lime glass; (a) view from beneath the fully-loaded specimen (light directed for specular reflection); (b) view in profile, after section-and-etch of unloaded specimen [94].	
Fig.2.21	63
Traces of Hertzian cracks on three low-index surfaces of silicon; (a) 100 (b) 111, and (c) 110; Specimens were lightly abraded, indented, etched, and viewed in normal reflected light. Diameter surface cracks 1.0 mm. Some abrasion scratches are still visible. Incomplete traces are due to small deviations from perpendicularity between specimen surface and the line of application of load [19].	
Fig.2.22	64
Partial cone crack damage track produced on soda-lime glass by sliding steel sphere (left to right), coefficient of friction, $\mu = 0.1$; (a) surface view; (b) profile view, after section-and-etch [9].	
Fig.2.23	65
Vickers indentation in soda-lime glass: (a) surface view; (b) side view. Radial and lateral crack systems are evident [9].	
Fig.2.24	66
Schematic of vent crack formation under point indentation. Median vent forms during loading (+) half cycle, lateral vents during unloading (-) half-cycle. Fracture initiates from inelastic deformation zone (dark region) [14].	

Fig.2.25	67
Vickers indentations in (a) soda-lime and (b) fused silica glasses in half-surface (top) and section (bottom) views. Specimens prepared by indenting across pre-existing hairline crack in glass surfaces, then breaking in order to obtain half-surface and section views. Indentation load = 30 N; Width of field = 220 μm . Crack components indicated: R = radial; L = lateral; C = cone. Different deformation zone configurations are noted (near-semi-circular region immediately below impression) in the section views [20].	
Fig.2.26	68
Scanning electron micrographs of Vickers indentations in three modifications of Al_2O_3 ; (a) grain size = 3 μm , (b) grain size = 20 μm , and (c) single crystal (sapphire) [21].	
Fig.2.27	69
(a) A schematic diagram illustrating the cross-sectional view of the contact between Vickers indenter and the particle. The pyramid indenter has a tip angle 2α [24]. (b) A Vickers indentation on $\text{Al}_{15}(\text{Mn,Fe})_3\text{Si}_2$ particle surface. Median cracks can be seen at each of the four corners of the indentation impression. The average crack length, $2c$, was used to calculate the fracture toughness of the particle, K_{IC} . Load = 25 g [24].	
Fig.2.28	70
Median/radial crack system, associated with a sharp indentation, showing (a) elastic/plastic configuration at full load subdivided into (b) elastic component at full load plus (c) residual component at complete unload [25].	
Fig.2.29	71
(a) A backscattered SEM image of a worn surface showing fracture and abrasive wear of silicon particles at 0.5 N after 6×10^5 sliding cycles, and (b) a high magnification	

secondary SEM image (20° tilt) of a worn surface showing Al pile-up on silicon particles at 1.0 N after 5×10^4 sliding cycles of a Al-25wt.%Si alloy. (c) A cross sectional SEM image of the wear track of Al-25wt.%Si showing the oil-residue layer on the contact surface with damage to silicon and Al-Si interface indicated [29].

Fig.2.30.....72

Schematic diagram of phase transformation that occur during hardness indentations and post-treatment in silicon [53]. During the loading stage of the indentation, silicon transforms from original diamond cubic Si-I structure to the hexagonal diamond Si-IV or the metallic β -Sn phase Si-II depending on local stress conditions. Upon unloading, due to pressure release, other polymorphic phases of silicon (Si-III and Si-XII) or an amorphous silicon forms depending on the unloading rate of the indenter. During annealing, there is a transition to Si-IV or, at higher temperatures, to Si-I.

Fig.2.31.....73

DC lattice projected onto $(1\bar{1}0)$ plane. Circles represent atoms in the plane of paper and crosses represent atoms in the plane below [61].

CHAPTER 3

Fig.3.1.....81

An optical microstructure of Al-18.5wt.%Si showing the different second phases. The silicon particles appear as dark brown with varying aspect ratios. The $Al_{15}(Fe,Mn)_3Si_2$ has a script-type morphology. The $\theta-Al_2Cu$ has the lightest contrast, appearing as small patches.

Fig.3.2	82
A SEM micrograph of a region in Al-18.5wt.%Si showing a large polyhedral silicon particle. A Vickers micro-indentation test has been performed on the silicon particle under a load of 350 mN.	
Fig.3.3	83
(a) SEM image of a 700 mN indentation on a silicon particle; (b) Optical profilometry image of the same indentation in (a); (c) High magnification (24,000X) SEM image of the deformed surface indicated in (a) by a red frame.	
Fig.3.4	84
(a) SEM image of a 300 mN indentation on a monolithic silicon {111}; (b) Optical profilometry image of the same indentation in (a); (c) High magnification (30,000X) SEM image of the deformed surface indicated in (a) by a red frame.	
Fig.3.5	85
Vickers hardness values for silicon in Al-18.5wt.%Si, plotted as a function of the indentation load, which is emphasized by a regression trend line. Indentation size effect (ISE) is observed from the hardness values at very low and high loads. (b) Optical microstructure showing a general view of the alloy; a 400 mN Vickers indent has been done on a silicon particle. (c) SEM image of a 750 mN indentation showing chipping-out fracture of silicon.	
Fig.3.6	86
Indentation fracture toughness (K_{IC}) measured using the crack length method of the (a) silicon particles and (b) $Al_{15}(Fe,Mn)_3Si_2$ phases shown in the inset.	

Fig.3.7	88
Diagram showing an encapsulated Al-Si sample prepared for heat-treatment and subsequent analysis of temperature-induced phase transformation in silicon.	
Fig.3.8	89
Renishaw InVia Raman Microscope.	
Fig.3.9	90
SEM images of the steps for preparing a TEM sample by FIB lift-out method, including (a) the ion milling of two trenches adjacent to the strip of carbon deposited on the membrane (TEM sample) containing the indentation, at which the membrane is connected at two points only; (b) a W needle is brought to the top of the membrane after another end is made free; (c) the needle is welded with the membrane by depositing carbon; (d) the other end of the membrane is freed after proper welding; (e) lifting out the TEM sample; (f) carrying the TEM sample to a Cu grid; (g) welding the sample to the grid and separating the needle from the sample; and (h) further fine ion-milling of the indented region to make it transparent to electrons.	

CHAPTER 4

Fig.4.1	97
(a) Indentation load vs. penetration depth curves generated from the Vickers micro-indentation of silicon particles in Al-18.5wt.%Si. 3-dimensional surface profilometry images of (b) 400 mN, (c) 600 mN, (d) 700 mN, and (e) 800 mN Vickers micro-indentations for different silicon particles. The amount of plastic deformation and crack formation in the silicon particles increased with the indentation load.	

Fig. 4.2	99
Ratio of the penetration depth at complete unloading, h_f , and the maximum penetration depth, h_m , as a function of indentation load. The h_f/h_m ratios decrease slightly with increasing load. This predicts the increased tendency of work hardening behaviour in silicon particles with load.	
Fig.4.3	100
Plot showing the influence of the indentation load on the measured elastic moduli of silicon particles. This change in the values can be explained by the change of the slope of the unloading curve of the indentation experiments as in Fig. 4.1(a).	
Fig.4.4	101
Plot depicting the plasticity (ratio of the plastic work done to the total work) involved in the silicon particles expressed as a function of the indentation load. Results indicate that this ratio decreases with load and thus the work of indentation is also load dependent.	
Fig.4.5	102
Plot showing that the ratio of the elastic modulus (E) and the Vickers hardness no. (H_V) of silicon particles (obtained from Figs. 4.3 and 3.5, respectively) is indentation load independent.	
Fig.4.6	103
(a) 2-dimensional profiles of indentation pile-ups starting from the centre of indentations to the silicon in Al-18.5wt.%Si, plotted as a function of the indentation load. A schematic explaining the limits of the 2-dimensional profiles is shown as an inset in (a). (b) Plot of indentation load vs. top points of the pile-ups found on silicon particles, and the depth of penetration.	

Fig.4.7.....105

(a) Plot showing the probability of subsurface lateral cracks in silicon particles reaching the surface [$P_f(L)$], as a function of the indentation load (L). An exponential curve fits the experimental data. (b) A Weibull distribution function plotted with the data points of the exponential trend in (a), and a Weibull probability curve is the inset which gave a modulus of 3.5.

Fig.4.8.....107

(a) An SEM image of a 475 mN Vickers indentation on a silicon particle, revealing the deformed surface of the residual indent. (b) A 3-dimensional surface profilometry image of the same indentation in (a), showing the halo due to subsurface lateral crack formation. The region of the FIB-milled trench has been shown with a dotted frame. (c) A SEM image of the FIB-milled region (cross-sectional view) of the same indentation as in (a) and (b), showing a semi-circular plastic core below the residual indent, and the subsurface crack pattern of the silicon particle.

Fig.4.9.....109

Raman spectra collected from silicon particles in Al-18.5wt.%Si. The gray curve is the spectrum obtained from a non-indented silicon particle, having Raman bands at 522.4 cm^{-1} (strong and sharp) and 306 cm^{-1} (weak and broad). The black curve is the spectrum obtained from the centre of a 475 mN Vickers micro-indentation on a silicon particle shown in the inset, having Raman bands (due to metastable crystalline phases of silicon in the indentation deformed surface) at 168.5 cm^{-1} , 186.2 cm^{-1} , 354.8 cm^{-1} , 377.5 cm^{-1} , 387 cm^{-1} , 399 cm^{-1} , 438.6 cm^{-1} , 496 cm^{-1} and 525.5 cm^{-1} . Objective, 50X.

Fig.4.10	110
Micro-Raman spectra from indented silicon particles (400 mN) in Al-18.5wt.%Si samples and heat treated at five different temperatures for 2 hrs with subsequent air-cooling.	

CHAPTER 5

Fig.5.1	117
Weibull statistical analysis involving the hardness values of Si in Al-18.5wt.%Si ($m = 8.24$) and Si single crystal {111} ($m = 8.78$). The Weibull moduli in both the cases were comparable although the hardness values of Si single crystal were relatively less variable.	
Fig.5.2	118
Weibull statistical analysis involving the hardness values of $Al_{15}(Fe,Mn)_3Si_2$ (Fe-phase; $m = 8.3$) and the θ - Al_2Cu (Cu-phase; $m = 4$) particles in Al-18.5wt.%Si. The Weibull moduli suggested that the hardness values of $Al_{15}(Fe,Mn)_3Si_2$ showed much less variation than those of θ - Al_2Cu .	
Fig.5.3	119
Weibull statistical analysis involving the K_{IC} values of Si particles in Al-18.5wt.%Si calculated using Eqs.1 and 2 of Table-3.1 .	
Fig.5.4	120
Weibull statistical analysis involving the K_{IC} values of Si single crystal {111} calculated using Eqs.1 and 2 of Table-3.1 . Comparing the Weibull moduli, K_{IC} values in this case were much less variable than the Si particles in Al-18.5wt.%Si (Fig. 5.2).	

Fig.5.5	121
Weibull statistical analysis involving the K_{IC} values of $Al_{15}(Fe,Mn)_3Si_2$ in Al-18.5wt.%Si calculated using Eqs.1 - 3 of Table-3.1 .	
Fig.5.6	122
A schematic diagram of an indentation model for the calculation of pressure exerted by the plastic core. L , indentation load; P_m , the mean pressure in the plastic core; c , radius of the plastic core.	
Fig.5.7	123
(a) A low magnification, bright-field TEM image of the deformed region underneath a 475 mN Vickers indentation. (b) SAED pattern obtained from plastically deformed region indicated as (b) in (a) with [011] zone axis. (c) and (d) are bright-field images of the regions indicated as (c) and (d), respectively, in (a), showing the existence of dislocations in the defect structure.	
Fig.5.8	126
(a) A bright-field, TEM image showing the V-shaped, plastically deformed region underneath a Vickers indentation. (b) HRTEM image of the region indicated as (b) in (a), showing the lattice fringes corresponding to the {111} planes of Si-I, with a measured interplanar distance of 0.313 nm. (c) HRTEM image of the regions indicated as (c) in (a), on the median crack boundary showing an amorphous region at the crack edge. (d) and (e) are FFT-derived diffraction patterns confirming the amorphous and crystalline region respectively seen in (c).	

CHAPTER 6

Fig.6.1.....130

A schematic diagram depicting the deformation and phase transformation related phenomena occurring in the silicon particles of Al-18.5wt.%Si during the loading and unloading stages of Vickers indentations.

LIST OF TABLES

CHAPTER 2

Table 2.1	24
Proposed relationships between K_{IC} , E and data obtained from Vickers hardness measurements. H_v = Vickers hardness number, P = Test load, $2a$ = the indentation mark diagonal, and $l = c-a$, where c is total crack length from centre of hardness mark [22].	
Table 2.2	25
Materials and mechanical properties for which Eqs.2.28-2.31 in Table-2.1 were developed [22].	

CHAPTER 3

Table 3.1	77
Calculation of the indentation fracture toughness (K_{IC}) of silicon particles using models [22] involving E = elastic modulus, H_v = Vickers hardness value, L = indentation load, $2a$ = the indentation mark diagonal, and $l = (c-a)$, where c is total crack length from centre of the residual indent as shown in Fig. 4.8(a) .	

CHAPTER 1: Introduction

1.1. Background of this Research

Lightweight Al-Si alloys are used in a variety of industries, particularly automotive [1, 2], because of their high strength-to-weight ratio. Introducing silicon to Al-Si alloys reduces the thermal expansion coefficient and improves their casting and machining characteristics, compared to the cast aluminum alloys in other series. Hypereutectic Al-Si alloys contain coarse, angular primary silicon particles and eutectic silicon particles. Apart from silicon, commercial Al-Si alloys also contain elements like Cu, Mn, Fe, etc. which have high solubilities in aluminum at elevated temperatures. During solidification and consequent heat-treatment processes, decrease from high to low concentration levels of these constituents prompts the precipitation of secondary intermetallic phases, like θ -Al₂Cu and Al₁₅(Fe,Mn)₃Si₂ [3]. These secondary phases present in Al-Si alloys, typically used to manufacture internal combustion engine cylinder liner material, carry majority of the imposed load. This leads to not only elastic and plastic deformation of the second phase particles, causing them to sink in the ductile aluminum matrix, but also triggers their fracture. It is for this reason that research on contact loading of these second phase particles, especially silicon, in Al-Si alloys is of such great importance.

High wear rates of Al-Si castings in components subjected to contact stresses compared to cast iron, however, impose a limitation on their powertrain applications. Wear rates in an internal combustion (IC) engine, measured using radionuclide techniques (RNT) [4] and radiotracer methods [5] should be as low as 1 nm/hr [6] to

maintain acceptable engine durability. Insight into deformation and fracture characteristics of second phase particles can be gained through static indentation experiments. When Vickers or Berkovich-type sharp indenters are used, the greatest concentration of tensile stress occurs directly below the indenter point, which coincides with the location of crack nucleation [7], and a plastic zone forms in the subsurface region in materials like fused silica and other glassy materials [8]. In case of loading with a blunt indenter, such phenomenon is possible only at high loads [8]. It is well known that, when a critical load is attained by application of a sharp indenter, radial (median) cracks form during the loading stage [9, 10] and propagate to form half-penny shaped cracks along the indent diagonals. A residual-stress field is normally considered to be responsible for formation of a lateral crack system in the subsurface region during unloading [7]. “Chipping-out” fracture, due to extensive lateral crack propagation, is a characteristic feature of sharp indentation and is detrimental [10].

Complexities in heat transfer during solidification process leave these particles arranged in a very random manner; an important reason why indentation-contact mechanics analyses of such particles results in large variations in the experimental data. Also, research with individual silicon particles in Al-Si alloys is definitely more challenging than that with monocrystalline silicon with a known orientation. So investigation of the defect structure underneath Vickers indentations on silicon particles in Al-Si alloys is vital due to reasons like revelation of the crack pattern in the subsurface region which causes fracture of silicon particles and understanding of deformation-induced phase transformations in silicon due to application of high pressure by means of indentation.

1.2. Scope of this Work

Al-Si alloys are used in applications that require surface durability where the applied stress is often carried by the silicon particles located on the contact surfaces. Consequently understanding the mechanisms of particle fracture is important. In this research, an investigation of micromechanisms of damage occurring in the silicon particles of cast Al-Si alloys has been provided.

Static Vickers indentation tests were performed, and indentation-induced surface and subsurface damage was investigated in detail using complementary analytical material characterization techniques. Characteristic damage features around the indentations (e.g., pile-up formations) were investigated by non-contact optical surface profilometry and the frequency of subsurface cracks reaching the surface as a function of the applied load was determined. Site specific FIB cross-sections viewed using (HR) TEM and SEM revealed subsurface damage microstructures with high precision including crack morphologies and dislocation structures in silicon particles. Raman micro-spectroscopy confirmed the role of indentation-induced phase transformations on damage events. This work depicts a comprehensive picture of the prevalent damage mechanisms.

In summary, this research contributes to the rationalization of the silicon particle fracture by providing a phenomenological analysis of statistical nature of the silicon particle fracture, and offering a detailed description of the micromechanisms leading to silicon particle fracture. Overall, the mechanical properties of silicon particles in Al-Si alloys have been better appreciated in this thesis.

1.3. Objective of Current Research

In this work, indentation-induced damage in the second-phases, namely, the silicon particles in a hypereutectic Al-Si alloy (Al-18.5wt.%Si) was studied by performing Vickers micro-indentation tests and examining the indentation surface morphologies with white light interferometry and electron microscopy. The material properties, namely, hardness and indentation fracture toughness, of Si, $\text{Al}_{15}(\text{Fe},\text{Mn})_3\text{Si}_2$ and $\theta\text{-Al}_2\text{Cu}$ phases of Al-18.5wt.%Si were determined and compared with those of monolithic Si {111} using Weibull statistics. The associated subsurface damage in the alloyed silicon particles was investigated using a combination of cross-sectional focused ion beam (FIB) microscopy and transmission electron microscopy (TEM). Indentation-induced phase transformations in these particles were determined using Raman micro-spectroscopy, and their roles in subsurface crack formation mechanisms were discussed. Temperature-induced phase transformation in micro-indented silicon particles was also observed by heat-treating encapsulated Al-18.5wt.%Si samples at different temperatures and subsequent micro-Raman spectroscopy of the residual indents.

1.4. Organization of this Thesis

This thesis consists of five chapters. The contents of this chapter have been described as below:

Chapter 1 is the introductory section starting with the background and followed by the scope and objective of this research including this current section.

Chapter 2 provides an insight into previous research work mainly related to the effects of sharp and blunt contacts on materials and the associated stress fields, deformation and damage types. It describes the Oliver and Pharr method of indentation experiments and the associated indentation fracture mechanics. A survey of statistical analysis of fracture has been provided along with microhardness induced damage in diamond cubic structured monolithic silicon. At the end of this chapter, a summary has been provided which highlights previous research yet defending the importance of the work to be done.

Chapter 3 describes the samples and the experimental procedure followed in this research, including microhardness measurements and indentation fracture toughness calculations of the different second phases in a cast Al-18.5wt.%Si alloy. Lastly, for subsurface defect investigation in silicon particles, a thorough description of the FIB in-situ “lift-out” technique of TEM membranes from silicon particles has been provided.

Chapter 4 depicts the results, showing indentation surface morphologies and providing a phenomenological description of silicon particle fracture. This is followed by the results of ion-milling, exposing subsurface damage and associated crack patterns in silicon particles. The results of micro-Raman spectroscopy of indented silicon particles at room and elevated temperatures are also presented.

Chapter 5 discusses the results of the previous chapter, beginning with Weibull statistical analyses used to compare material properties (hardness and indentation fracture toughness) of Si, $\text{Al}_{15}(\text{Fe},\text{Mn})_3\text{Si}_2$ and $\theta\text{-Al}_2\text{Cu}$ phases of Al-18.5wt.%Si, to those of

monolithic Si {111}. The pressure exerted by indentation was estimated and the role of phase transformation on subsurface damage mechanisms has been discussed.

Chapter 6 summarizes this entire research and presents the conclusions arising from this effort, including the scope of future work in this field of research.

CHAPTER 2: Literature Survey

2.1. Introduction to this survey

Many parameters affect the surface deformation mechanisms of materials. Hardness is frequently defined as an indicator of the material's resistance to deformation, and is still one of the most significant material properties in that regard. Apart from hardness, instrumented scratch testing has proven to be a useful tool to characterize surface deformation of materials. This survey deals with all previous important research on indentation contact mechanics, silicon indentation, pressure induced phase transformations in silicon, deformation mechanisms in silicon due to sharp contact both at room temperature and at elevated temperatures, and statistical nature of brittle fracture.

2.2. Static Hardness

Material surfaces exhibit two basic responses when an external force is applied [11], namely, surface/subsurface deformation and fracture. The hardness of a metal is often defined as its resistance to indentation [12]. In the Brinell hardness test, a hard steel ball is pressed under a fixed normal load on the smooth surface of the metal being tested. When equilibrium has been reached, the load and indenter are removed and the diameter of the permanent impression is measured. The hardness is then expressed as the ratio of the load to the curved area of the indentation (Brinell hardness), or as the ratio of the load to the projected area of the indentation (Meyer hardness). In both cases, the hardness values have the dimension of pressure. The relation between load and indentation size may be expressed by a number of empirical relations. The first of these, known as

Meyer's law, states that if P is the load applied and d the diameter of the impression left when the indenter is removed, then,

$$P = kd^n \quad (2.1)$$

where, k and n are constants for the material when the diameter of the ball is fixed.

The value of n is generally greater than 2, and usually lies between 2 and 2.5. For completely unworked materials, n has a value near 2.5, while for fully-worked materials, it is closer to 2. When balls of different diameters are used, the values of these constants change. For balls of diameters D_1, D_2, D_3, \dots , giving impressions of diameters d_1, d_2, d_3, \dots , a series of relations is obtained as,

$$P = k_1 d_1^{n_1} = k_2 d_2^{n_2} = k_3 d_3^{n_3} \quad (2.2)$$

In an extensive series of investigations, Meyer (1908) experimentally found that the index n was almost independent of D but that k decreased with increasing D in such a way that,

$$A = k_1 d_1^{n-2} = k_2 d_2^{n-2} = k_3 d_3^{n-2} = \dots, \quad (2.3)$$

where, A is a constant.

When conical or pyramidal indenters are used, such as the Ludwik and Vickers hardness tests respectively, a much simpler relationship is observed. Over a wide range of experimental conditions, it was found that,

$$P = kd^{2.0} \quad (2.4)$$

This is true for an indenter of constant angle. The power of d is fixed, but k depends on the angle of the cone or pyramid used.

2.3. Indentation Stress Fields

A closer look at the nature of the contact zone provides a good picture of the nature of the stress field within a loaded system (indenter and specimen). Here, the shape of the indenter is a vital factor in determining the boundary conditions for the field, as indicated in **Fig. 2.1**. The mean contact pressure, p_o , is given by [13],

$$p_o = \frac{P}{\alpha\pi a^2} \quad (2.5)$$

where, P is the applied load, a , the contact radius, and α is a dimensionless constant reflecting the indenter geometry.

2.3.1. Nature of Stress Distribution due to a Point Force; Boussinesq Solution

The indentation of a solid by a sharp indenter may be idealized as shown in **Fig. 2.2**. A concentrated point force P is applied at the origin of the cylindrical coordinate system (r, θ, z) , which is located on the surface of a semi-infinite solid. Due to the applied load, the elastic solid undergoes elastic deformation and a stress field is established. This is the Boussinesq problem, the solution for which is summarized in the Appendix (p-138). For an isotropic material of Poisson's ratio ν , the stress components in the curvilinear coordinate system of **Fig. 2.2** assume a simple, general form [14] as given by,

$$\sigma_{ij} = \left(\frac{P}{\pi R^2} \right) [f_{ij}(\phi)]_\nu \quad (2.6)$$

That is, the magnitude of the stresses is proportional to the applied load and to the inverse square of the radial distance, R , from the point of contact, times some independent angular function which is, itself, a function of the Poisson's ratio, ν .

It becomes convenient to rewrite the previous equation in alternative, normalized form,

$$\frac{\sigma_{ij}}{p_o} = \alpha \left(\frac{a}{R} \right)^2 [f_{ij}(\phi)]_v \quad (2.7)$$

The essential features of the field are illustrated in **Figs. 2.3** and **2.4**, for the case $\nu = 0.25$ (a typical value for brittle solids). We investigate the directions of the principal stresses, σ_{11} , σ_{22} and σ_{33} , by means of the stress-trajectory plots in **Fig. 2.3**. The three families of trajectories are labelled such that $\sigma_{11} \geq \sigma_{22} \geq \sigma_{33}$ nearly everywhere. Similarly, we investigate the distribution of the principal stresses by means of the contour plots in **Fig. 2.4**. The components σ_{11} and σ_{33} , acting within symmetry planes through the load axis, are entirely tensile and compressive, respectively. The component σ_{22} , a "hoop stress", is tensile in a region below the indenter ($\phi < 51.8^\circ$), but compressive near the surface. We note maxima in the tensile stresses at $\phi = \pi/2$ (σ_{11}) and $\phi = 0$ ($\sigma_{11} = \sigma_{22}$). The relative magnitudes of the three principal normal stresses are shown in **Fig. 2.5(a)**, in which just the angular function of Eq.2.6 is plotted. Similar plots are given for maximum principal shear stress and hydrostatic compression in **Fig. 2.5(b)**. It is also worth noting that σ_{33} actually exceeds σ_{22} in a shallow surface region $\phi < 77.2^\circ$, while σ_{12} replaces σ_{13} as the maximum shear stress.

It would appear that, given favourable initiation conditions, the tensile component of the point-indentation field might well be sufficiently large enough to sustain a brittle crack. In this context, the value of Poisson's ratio becomes an important consideration [14]. While the maximum principal shear and the hydrostatic compression are insensitive

to variations in this term, the same is not true of the tensile stress; at $\nu = 0.5$, the tensile component disappears completely.

2.3.2. Hertzian Stress Distribution due to a Spherical Indenter

We consider an isotropic, linear elastic half-space subjected to normal loading, P , by a smooth spherical indenter of radius, r . The pressure (or normal stress) across the circle of contact is not uniform, but at any point distant x from the centre of the indentation, the pressure has a value [15] of,

$$P = p_c \left(1 - \frac{x^2}{a^2} \right)^{\frac{1}{2}} \quad (2.8)$$

where, p_c is the pressure at the centre of the circle of contact (**Fig. 2.6**). It follows that,

$$p_c = \frac{3}{2} p_o \quad (2.9)$$

The Hertzian pressure is hemispherically distributed on a planar contact area with the contact radius, a ,

$$a = \left(\frac{3Pr}{4E^*} \right)^{\frac{1}{3}} \quad (2.10)$$

where, r is the radius of the sphere and E^* is the modified elastic modulus. E^* depends on Young's moduli, E_1 and E_2 , and on the Poisson's ratios, ν_1 and ν_2 , for the materials of the sphere (indenter) and of the plane (specimen) in the following way,

$$\frac{1}{E^*} = \frac{(1-\nu_1^2)}{E_1} + \frac{(1-\nu_2^2)}{E_2} \quad (2.11)$$

Thus the projected area of the indentation, A , is proportional to $P^{\frac{2}{3}}$ and the mean contact pressure, p_o , over the region of the contact is proportional to $P^{\frac{1}{3}}$ (**Fig. 2.7**).

As previously stated, the applied load is distributed as a hemisphere of compressive stress within the contact circle [Fig. 2.1(d)]. The maximum tensile stress in the specimen surface occurs at the edge of the contact, and is radially directed. It falls off with radial distance, r (Fig. 2.2), outside the contact circle according to,

$$\frac{\sigma_{rr}}{p_o} = \left(\frac{1-2\nu}{2} \right) \left(\frac{a}{r} \right)^2, \quad (r \geq a) \quad (2.12)$$

In 1904, Huber extended the Hertz analysis and produced complete stress field solutions in the form [13],

$$\frac{\sigma_{ij}}{p_o} = \left[g_{ij} \left(\frac{r}{a}, \frac{z}{a} \right) \right]_v \quad (2.13)$$

Proceeding as with the Boussinesq case, we plot trajectories and contours for the function of Eq.2.13 in Figs. 2.8 and 2.9, corresponding to the three principal stresses for $\nu = 0.33$ this time.

2.3.3. Comparison between the Boussinesq and Hertzian Fields

Comparing Figs. 2.8 and 2.9 with their counterparts in Figs. 2.3 and 2.4, it is apparent that the precise form of the applied load distribution can have a profound influence on the nature of the near-contact field [13]. With regard to the directions of the principal stresses, the main change appears to be a flattening of the σ_{11} trajectories immediately below the contact area. More dramatic changes appear in the magnitudes of the stresses in which the tensile components tend to be locally suppressed. Both σ_{11} and σ_{22} become compressive to a depth $\approx 2a$, below which a rapid convergence to Boussinesq value occurs; Fig. 2.10 illustrates this convergence for the stress $\sigma_{\theta\theta} = \sigma_{11} = \sigma_{22}$ along the contact axis. In the surface region outside the contact, no sign reversal in the stresses

is evident but extremely high stress gradients are set up at the edge of the contact. These gradients become especially severe for small contact areas.

2.4. Onset of Plastic Deformation

When two elastic bodies are pressed lightly against each other, the contact is purely elastic. With increasing load, the contact becomes elasto-plastic and the pressure distribution becomes more and more uniform. If the applied normal load exceeds a critical value, which is the elastic limit, a plastic zone develops surrounded by an elastically deformed material [16]. The elastic limit can be calculated from,

$$p_o = 1.85\tau_y \quad (2.14)$$

where, p_o is the mean contact pressure and τ_y is the yield stress in pure shear. If the *Tresca* or *Huber-Mises* criterion is applied to the stresses in the metal, the condition for plasticity is first reached at a point below the actual surface of contact (**Fig. 2.11**). The calculated shear stress in the metal below the surface has been plotted, and it revealed that the maximum value occurs at a point about $0.47a$ below the centre of the circle of contact, where a is the contact radius. The value of the shear stress at this point is $0.47 p_o$ (for materials having $\nu = 0.3$). With the two radial stresses are equal at this point, the *Tresca* and *Huber-Mises* criterion both indicate that plastic flow will occur when the shear stress equals $0.5Y$ (i.e., when $0.47 p_o = 0.5Y$, where Y is the yield stress [15]). This means that plastic deformation commences in this region when,

$$p_o \approx 1.1Y \quad (2.15)$$

As long as the mean pressure continues to be less than this, the deformation remains completely elastic and on removing the load, the surface and the indenter return

to their original shape. As soon as p_o reaches the value of $1.1Y$, however, some plastic deformation occurs in the region Z [Fig. 2.12(a)]. The rest of the metal is deformed elastically, so that on removing the load, the amount of residual deformation is very small.

2.5. The Indentation Experiment

When the indenter is first driven into a specimen, both elastic and plastic deformation occurs (Fig. 2.13). The plastic deformation causes a permanent hardness impression that conforms to the shape of the indenter to some contact depth, h_c . The elastic deformation results in an additional component of displacement, such that the surface displaces downward at the edge of the contact by an amount h_s . So the total displacement is,

$$h = h_s + h_c \quad (2.16)$$

When the indenter is withdrawn from the specimen, the elastic displacements are recovered.

2.5.1. Loading and Unloading Curves; Oliver and Pharr Model

Oliver and Pharr [17] found that the unloading curve (Fig. 2.14) follows a simple power law,

$$P = A(h - h_f)^m \quad (2.17)$$

where, P is the load, A , m are constants, and, h_f is the final depth of the residual hardness impression. The contact stiffness, S , is defined as the slope of the initial portion of the unloading curve,

$$S = \frac{dP}{dH} = mA(h - h_f)^{m-1} \quad (2.18)$$

The contact depth is found to be in the range extrapolated from the initial stages of unloading curve,

$$h_c = h_{\max} - 0.75 \frac{P_{\max}}{S} \quad (2.19)$$

where, P_{\max} is the peak load. The hardness, H , is defined as the mean pressure that the material will support under load.

$$H = \frac{P_{\max}}{A(h_c)} \quad (2.20)$$

where, $A(h_c)$ is the area function related to h_c . Reduced modulus, E^* , having contributions from both the indenter and the sample, is defined as,

$$E^* = \frac{S\sqrt{\pi}}{2\sqrt{A(h_c)}} \quad (2.21)$$

2.5.2. Work of Indentation

By integrating the loading and unloading curves, the work of indentation can be readily obtained [18]. The area under the loading curve is the total work, W_{tot} ; the area under the unloading curve is the reversible work, W_u ; the area enclosed by the loading and unloading curves is the irreversible work, W_p (**Fig. 2.15**), of indentation. Therefore, we have,

$$W_{tot} = W_u + W_p \quad (2.22)$$

2.5.3. ‘Sinking-in’ and ‘Piling-up’ Phenomena

According to Tabor [12], materials immediately outside the contact area of an indentation usually deform and do not remain flat. In case of a heavily work-hardened metal, the surface of the specimen around the indentation bulges upwards or piles-up, and for a fully annealed metal, the surface of the specimen around the indentation sinks in [18]. Both piling-up and sinking-in phenomena are schematically illustrated in **Fig. 2.16**. The piling-up and sinking-in phenomena are important as they affect the accurate determination of contact areas and, subsequently, the hardness measurements. Also, it remains to be investigated whether the pile-up area carries load.

Dimensional analysis helps to identify the parameters affecting the piling-up and sinking-in. In general, the contact depth is a function of all independent parameters,

$$h_c = f(E, \nu, Y, n, h, \theta) \quad (2.23)$$

where, E = Young’s modulus, ν = Poisson’s ratio, Y = the initial yield strength, n = the work hardening exponent, h = the indenter displacement, and, θ = the indenter half angle which characterizes the indenter geometry.

The dimensions of Y , ν , n , h and h_c can be expressed in terms of E and h , the two parameters with independent dimensions. Applying the Π -theorem in dimensional analysis, we obtain,

$$\Pi_\beta = \Pi_\beta(\Pi_1, \nu, n, \theta), \text{ or, } h_c = h\Pi_\beta\left(\frac{Y}{E}, \nu, n, \theta\right) \quad (2.24)$$

where, $\Pi_\beta = \frac{h_c}{h}$, and, $\Pi_1 = \frac{Y}{E}$, ν , n and θ are all dimensionless. It is seen that the ratio

$\frac{h_c}{h}$ is a function of both $\frac{Y}{E}$ and n , as predicted by dimensional analysis. Also, the value

of $\frac{h_c}{h}$ can be either greater or smaller than one, corresponding to the piling-up and sinking-in of the displaced surface profiles, respectively. Thus, dimensional analysis together with finite element calculations has made it clear that for conical and pyramidal indentations, the magnitude of piling-up and sinking-in is determined by neither n alone, nor all three parameters Y , E , and n . It is determined by two parameters $\frac{Y}{E}$ and n for a given indenter.

2.6. Indentation Fracture Mechanics

Indentation constitutes one of the most powerful test techniques for the systematic investigation of deformation and fracture responses in materials. To be precise, indentations represent a model flaw system for quantifying a wide range of mechanical properties, and as such deserve detailed study. In this section, we are going to deal with the basic conditions for crack nucleation, the basic indentation fracture systems, the types of Hertzian cracks and the different fracture toughness models.

2.6.1. Criteria for Crack Formation

When the surface layers of an initially flaw-free material undergo plastic deformation, voids and cracks can nucleate. The failure of a material proceeds in two steps [11],

Step 1: The initiation and nucleation of microcracks or microvoids, and,

Step 2: Crack propagation or void growth that leads to catastrophic failure.

Cracks in two-phase materials are nucleated around the hard particles due to the displacement incompatibility between the particle and the matrix, which occurs when the

matrix deforms plastically near the surface with repeated loading, but the hard particles cannot deform.

The fact that the crack nucleation in two-phase materials is due to the displacement incompatibility between the spherical inclusions and the matrix is illustrated as follows. We consider a hard, rigid, spherical particle surrounded by an elastoplastic matrix that undergoes shear deformation. In the absence of the hard inclusion, the matrix will deform in such a manner that an imaginary spherical boundary will assume an ellipsoid shape, as shown in **Fig. 2.17**. However, in the presence of the rigid sphere, which is well bonded to the matrix, the interface cannot assume the ellipsoidal shape because of the geometric constraint imposed on the matrix by the sphere. Consequently, normal stresses are developed at the sphere-matrix interface. At location *A* the normal stress is compressive, while at location *B*, it is tensile. When the tensile normal stress at *B* exceeds the cohesive (or adhesive) strength of the bonding at the particle-matrix interface, a crack may nucleate if the energy criterion is also satisfied. The strength criterion may be expressed as,

$$(\sigma_{kk})_{\max} \geq \sigma_i \quad (2.25)$$

where, $(\sigma_{kk})_{\max}$ is the maximum principal normal stress in tension, and σ_i is the ideal cohesive strength at the interface.

The energy criterion for void nucleation must be satisfied in addition to Eq.2.25. When the inclusion-filled material is subject to an external load, strain energy is stored in the elastic field within and around the inclusion. This strain energy will change as the elastic field changes during void nucleation. The energy in the matrix-inclusion system,

E^s , should be sufficient to provide for the surface energy created by the void nucleation process. This may be expressed as,

$$E_{before}^s - E_{after}^s \geq \Delta\gamma.A \quad (2.26)$$

where, A is the surface area of the nucleated void (or crack), and $\Delta\gamma$ is the surface energy change during void nucleation. If the void nucleates at the matrix-inclusion interface,

$$\Delta\gamma = -\gamma_{M-I} + (\gamma_M + \gamma_I) \quad (2.27)$$

where, M = matrix, I = inclusion, and γ = the surface energy. Eq.2.27 is inclusion-size independent, since the strain energy is proportional to the volume, and the surface energy is proportional only to the surface area. This is in contrast to the strength criterion, which is independent of the size. **Fig. 2.18** schematically shows both the strength, and the energy criterion expressed in units of applied elastic strain as a function of the inclusion size. For an inclusion size larger than d^* , the energy criterion is always satisfied whenever the strength criterion is reached. However, for inclusion sizes smaller than d^* , satisfying the strength criterion does not necessarily guarantee the satisfaction of the energy requirement. In metals, this critical size is in the range of a few hundred angstroms.

2.6.2. Basic Indentation Fracture Systems

With the change in the shape of the indenter tip, blunt or sharp, there is change in the type of crack formed. The two main indentation fracture systems include the *cone crack system* associated with a blunt indenter, and the *median crack system* associated with a sharp indenter. **Fig. 2.19** demonstrates the essential features of crack geometry for both blunt and sharp indenters, along with the appropriate fracture mechanics parameters [13]. In each case, the indenter sets up a contact stress field, the tensile component of

which provides the necessary driving force for initiating fracture. If the applied load, P , is concentrated at a point on the surface (or, $a \rightarrow 0$), the intensity of the stresses will vary according to the Boussinesq solution (Section 2.3.1). In reality, the stress level cuts off at some finite limit within the contact region. With blunt indenters, this cut-off is a manifestation of redistribution in load over a non-zero, elastic contact area whereas with sharp indenters, it is associated with the inability of the material to sustain stresses greater than a particular yield value [9]. For blunt contacts, cracks usually nucleate from pre-existing surface flaws (small dashes) outside the contact area (shaded), form into a surface ring (broken line), and finally become critical and propagates into a fully developed cone. For sharp contacts, cracks nucleate from the plastic contact zone (shaded) in the subsurface region, form into a contained penny (broken circle), and ultimately develop into a full half-penny.

2.6.3. Blunt Indenter

If contact conditions remain entirely elastic up to the onset of fracture, the indenter is deemed blunt [9]. The classical example is the Hertzian cone fracture produced by the indentation of a flat surface with a relatively hard sphere. In such cases, initiation occurs from pre-existing surface flaws in the region of high tensile stress just outside the circle of contact [**Fig. 2.20(a)**]; the ensuing crack circles the contact and subsequently propagates downward and outward into its fully developed (truncated) cone configuration [**Fig. 2.20(b)**].

- **Some variants from the ideal cone fracture configuration**

In this section, we deal with two of the several invariants that can be produced in the blunt-indenter crack patterns [19].

Case I. If the test material is not isotropic, homogeneous, or free of pre-existing residual stresses, departures can occur from the ideal cone geometry, even under axial loading. This is demonstrated in **Fig. 2.21** for sphere indentations on single crystal silicon surfaces.

Case II. In the second case, we consider the changes in the pattern that ensue when the indenting sphere is made to slide across the test surface with frictional tractions. **Fig. 2.22** shows a sliding-indenter track on soda-lime glass [9]. Several intermittent (partial) cone cracks are generated in the wake of the advancing indenter.

2.6.4. Sharp Indenter

As the indenter tip becomes sharper, there is an increased prospect of some pre-fracture yield at the contact zone. We take a closer look at the crack pattern generated in a sharp contact. If we take top and side views, as shown in **Fig. 2.23** for a Vickers indentation on soda-lime glass, we find there are two operative crack systems [9],

1. *Radial/Median cracks* extend on median planes containing the load axis and an impression diagonal (where stress concentrations are highest).
2. *Lateral cracks* extend from near the base of the subsurface deformation zone in a saucer-like manner, roughly parallel to the specimen surface.

Under normal loading conditions, both crack types attain a penny-like configuration in that their fronts are near-circular (or semi-circular in the case of median cracks). Thus, based on outward appearances, we might be led to conclude that the mechanics of crack propagation in the contact far field are really no different for sharp indenters than for blunt indenters.

For the case of sharp indenters, the basic sequence of subsequent crack propagation events has been depicted schematically [14] in **Fig. 2.24**: **(a)** the sharp point of the indenter produces an inelastic deformation zone; **(b)** at some threshold, a deformation-induced flaw suddenly develops into a small radial/median vent on a plane of symmetry containing the contact axis; **(c)** an increase in load causes further, stable growth of the median vent; **(d)** on unloading, the median vent begins to close (but not heal); **(e)** in the course of indenter removal, sideways-extending cracks, termed lateral vents, begin to develop; **(f)** upon complete removal, the lateral vents continue their extension towards the specimen surface, and may accordingly lead to chipping. Immediate reloading of the indenter closes the lateral vents, and reopens the median vents.

- **Some variants from the ideal sharp indenter pattern**

In this section, we deal with two invariants in the crack patterns produced by a sharp-indenter.

Case I. The first case occurs in anomalous glasses like fused silica, which deform by densification rather than by volume-conserving flow. **Fig. 2.25** compares Vickers indentations in soda-lime and fused silica glasses [20]. The patterns for the two glasses show clear differences, particularly in the near-contact region. It appears that in fused silica, the intense local displacements induced by the penetrating indenter generate the same kind of shear offsets at the contact surface, but that these do not extend downward into the material as they do in soda-lime glass.

Case II. As a second example, we consider how the crack patterns may be affected by the inhomogeneities in the material system. The potential for significant

crack-microstructure interactions is demonstrated in **Fig. 2.26**, which shows Vickers indentations in alumina of three different grain sizes [21]. The sequence represents the systems in which the radial cracks are **(a)** much larger than, **(b)** comparable with, and **(c)** much smaller than the scale of the microstructure. In cases **(a)** and **(c)**, the crack patterns are well defined, as though the materials were effectively homogenous, but in **(b)**, it is difficult to distinguish any true radial cracks at all.

2.6.5. Indentation Fracture Toughness (K_{IC}); the Crack-Length Method

The value of K_{IC} for a given material is unaffected by specimen dimensions or type of loading, provided that the specimen dimensions are large enough relative to the plastic zone to ensure plane-strain conditions around the crack tip (the strain being zero in the through-thickness direction) [22]. Therefore, K_{IC} is particularly convenient in materials selection because, unlike other measures of toughness, it is independent of specimen geometry. An empirical method for determining K_{IC} from Vickers microhardness testing was first developed by Palmqvist (1962). Later, the same technique was used to develop a number of relations between K_{IC} , load (P), indentation diagonal (a), crack length from the centre of the indentation (c), Young's modulus (E), and Vickers hardness number (H_V) of a material. Ponton and Rawlings [23] have summarized these relationships. The numerous indentation fracture models reported in the literature are classified into two groups. In one group it is assumed that the cracks that form from the Vickers indentation marks are well developed radial-median, halfpenny-shaped cracks, and in the other group it is assumed that radial Palmqvist cracks are formed.

Examples of equations [22] for calculating K_{IC} for Palmqvist cracks are given in the third column of **Table 2.1**. Each of these equations was derived for a number of

materials with the range of mechanical properties (K_{IC} , E , H_v) given in **Table 2.2**. The crack geometry ranges l/a for Eqs.2.28 and 2.29 are given in **Table 2.1**. For Eqs.2.30 and 2.31, there are no crack limitations.

Table 2.1: Proposed relationships between K_{IC} , E and data obtained from Vickers hardness measurements. H_v = Vickers hardness number, P = Test load, $2a$ = the indentation mark diagonal, and $l = c-a$, where c is total crack length from centre of hardness mark [22].

Eq. No.	Equation	Rearranged Eq., $y = \text{constant} \times x$
2.28	$K_{IC} = 0.0089 \left(\frac{E}{H_v} \right)^{\frac{2}{5}} \cdot \frac{P}{a.l^{\frac{1}{2}}}$, for $2.5 \geq \frac{l}{a} \geq 0.25$	$al^{\frac{1}{2}} = \left(\frac{0.0089E^{\frac{2}{5}}}{K_{IC}} \right) \frac{P}{H_v^{\frac{2}{5}}}$
2.29	$K_{IC} = 0.0122 \left(\frac{E}{H_v} \right)^{\frac{2}{5}} \frac{P}{a.l^{\frac{1}{2}}}$, for $2.5 \geq \frac{l}{a} \geq 1$	$al^{\frac{1}{2}} = \left(\frac{0.0122E^{\frac{2}{5}}}{K_{IC}} \right) \frac{P}{H_v^{\frac{2}{5}}}$
2.30	$K_{IC} = 0.0319 \frac{P}{a.l^{\frac{1}{2}}}$	$al^{\frac{1}{2}} = \left(\frac{1}{K_{IC}} \right) 0.00319P$
2.31	$K_{IC} = 0.0143 \left(\frac{E}{H_v} \right)^{\frac{2}{3}} \left(\frac{a}{l} \right)^{\frac{1}{2}} \frac{P}{c^{\frac{3}{2}}}$	$\left(\frac{l}{a} \right)^{\frac{1}{2}} c^{\frac{3}{2}} = \left(\frac{0.0143E^{\frac{2}{3}}}{K_{IC}} \right) \frac{P}{H_v^{\frac{2}{3}}}$

Table 2.2: Materials and mechanical properties for which Eqs.2.28-2.31 in **Table-2.1** were developed [22].

Eq. No.	Materials	Range of Mechanical Properties		
		$K_{IC}, MPa\sqrt{m}$	E, GPa	H_v, GPa
2.28	B ₄ C, Si ₃ N ₄ , SiC(sintered), SiC (hot pressed), ZnS, ZnSe, WC-Co cermets	0.9-16	≈70-575	1-30
2.29	WC-Co (12% Co), Si ₃ N ₄ , SiC, B ₄ C, soda-lime silica glass	0.75-12	≈70-575	5-24
2.30	WC-Co cermets	7.7-13.1	≈575	11-20
2.31	Si ₃ N ₄ , Al ₂ O ₃ , glass ceramic, sapphire, glass, Si	0.7-4.6	70-425	5.5-22

Riahi and Alpas [24] measured the K_{IC} of silicon-rich particles (SRP) in an Al-12%Si alloy using the micro-indentation method, by applying a normal load of 25 g to the surface of selected particles by a Vickers indenter. The diameter, $2c$, of the semi-circular cracks (median cracks) that formed under the indenter was estimated by measuring the average length of the cracks that reached the contact surface. The relationship between the fracture toughness, K_{IC} , and the loading parameters P , c , and the indenter tip angle, 2α is [7],

$$K_{IC} = \frac{P}{(\pi.c)^2 \cdot \tan \alpha} \quad (2.32)$$

An example of the post indentation impression on an Al₁₅(Mn,Fe)₃Si₂, and the resulting cracks emanating from the indentation's corners are shown in **Fig. 2.27**.

2.7. Vickers Indentation and Associated Elastic/Plastic Indentation Damage

Indentation fracture analysis requires knowledge of the stress fields through which cracks initiate [13]. For the sake of simplicity, it is convenient to distinguish between near and far stress fields in the deformation zone. Lawn et al. [25] suggested a model of median/radial crack system for sharp contacts pertaining only to “well-developed” cracks. In this model, the net indentation driving force for fracture is subdivided into well defined components. The elastic/plastic field of the fully loaded indenter is considered as a superposition of the residual field in the unloaded solid plus the field of an ideally elastic contact.

Fig. 2.28 outlines the model. In **Fig. 2.28(a)**, the indenter at load P generates a median-plane crack of characteristic dimension c . The plastic zone is taken to support the indenter, included angle 2ψ , over the characteristic contact dimension, a , and to extend radially outward over a characteristic dimension b . Separation of the elastic/plastic problem into elastic and residual components is shown in **Figs. 2.28(b)** and **(c)**. The elastic field is said to operate outside the plastic zone, in the region where cracking occurs, reaching its maximum intensity at full loading and reversing completely on unloading. Because of this reversibility, the elastic driving force may be defined by the stress distribution $\sigma(r, \phi)$ at $r \geq b$ in **Fig. 2.28(b)** over the prospective crack plane, and may therefore be obtained from classic elastic contact solutions. The residual field arises from mismatched tractions exerted on the surrounding matrix by deformed material within $r \leq b$. This component reaches maximum intensity at full loading, but persists as the indenter is removed. In the approximation of well-developed cracks, i.e., $c \gg b$, these

mismatched tractions manifest themselves as a net outward force acting at the crack centre [Fig. 2.28(c)]. It is, thus, very obvious from Fig. 2.28, that adding configurations (b) and (c) is equivalent to reloading the indenter to the original maximum load configuration in (a).

2.8. Deformation and Fracture of Silicon in Al-Si Alloys during Sliding Contact

Deformation and damage of silicon particles in Al-Si alloys used in automobile engines has been studied previously. Dienwiebel et al. [26] have observed that, initially, the engine piston ring slides over the protruding second phase silicon particles on the Al-Si cylinder bore surface, but then come into contact with a new surface layer consisting of fractured silicon particles mixed with aluminum. Riahi et al. [24] have shown that, in a chemically etched Al-12%Si alloy subjected to sliding contact with a Vickers indenter, there is a critical particle size-to-indenter contact width ratio (1:8) for protruding second phase particles, below which the particles fractured from their roots at the point of attachment to the aluminum matrix. For large ratios ($\gg 1$), the particles underwent plastic deformation on their contact surfaces rather than fracturing.

Chen and Alpas [27] performed sliding tests on Al-18.5wt.%Si under a low load of 0.5 N, and observed that the wear damage was restricted to the top surface of the silicon particles. This condition corresponded to the ultra-mild wear regime, in which the silicon particles effectively protected the soft, aluminum matrix from damage. At high loads (5.0 N), silicon particles fractured and became embedded (particle sinking-in) within the aluminum matrix [28]. During the course of the sliding process, the fractured silicon particles (Fig. 2.29) were fragmented to nano-size and mixed with organic

components from the oil-forming protective layer that helped to prevent further wear to the aluminum surface [29].

Finite element simulations of particle sinking-in predicted that interface failure (slipping) would occur during loading, whereas interface decohesion (opening up) would occur during unloading [30]. Under actual engine running conditions, formation of angular silicon fragments as a result of particle fracture intensified the overall damage process by causing abrasive wear to the engine's cylinder surface [28, 31]. Clearly, extensive research has been directed towards the conditions leading to multiple particle fracture and decohesion in Al-Si alloys. There still remains the scope of research on the details of damage accumulation and the mechanisms of fracture of silicon particles; a field which largely remains unexplored.

2.9. Statistical Analysis of Fracture: Weibull Modeling

Brittle materials exhibit a scatter in failure strength data, unlike ductile materials where plastic deformation takes place. The mode of fracture in a homogenous brittle material depends on the stress necessary to propagate an existing critical flaw or crack in it. In certain materials, flaws can be inclusions, segregations or any other centers which give rise to incompatible deformations. Therefore, variable sizes, shapes and orientations (with respect to the applied load) of the flaws in a material can account for the observed scatter of fracture strengths. A statistical method commonly used to determine the strength of brittle materials was introduced by Weibull [32].

2.9.1. Functional Deduction of Weibull's Formula

The independent theory of probability states that two events, A and B , are independent if the probability that they both occur is equal to the product of the probabilities of the two individual events, i.e.

$$P(A \cap B) = P(A)P(B) \quad (2.33)$$

This theorem was used by Waloddi Weibull for the deduction of the probability of failure. A formulation, in connection with the unicity theorem [33] has been deduced here.

If V is the body volume, σ is the constant stress-field, V_1 and V_2 are representing an arbitrary subdivision (without common points) of body volume and P is the cumulative survival probability, then we have,

$$P_s(V_1 + V_2, \sigma) = P_s(V_1, \sigma)P_s(V_2, \sigma)$$

$$V_1 \cap V_2 = \{ \}, V_1 \cup V_2 = V \quad (2.34)$$

where, \cap is the intersection of the set, \cup is the union of the set, and $\{ \}$ is the null set. It can be assumed that the survival probability of a very small body tends to unity when the body size tends to zero: $P_s(V \rightarrow 0, \sigma) \rightarrow 1$. Thus it can be said that,

$$P_s(0, \sigma) = 1 \quad (2.35)$$

Substituting alternatively the value zero for V_1 and for V_2 in Eq.3, we have,

$$\begin{aligned}
P_{12}(V_1 + 0, \sigma) &= P_{12}(V_1, \sigma) = P_1(V_1, \sigma) \\
P_{12}(0 + V_2, \sigma) &= P_{12}(V_2, \sigma) = P_2(V_2, \sigma)
\end{aligned} \tag{2.36}$$

and hence,

$$P_{12}(V, \sigma) = P_1(V, \sigma) = P_2(V, \sigma) = P_s(V, \sigma) \tag{2.37}$$

Using the unicity theorem, Eq.2.34 can be expressed as,

$$P_s(V_1 + V_2, \sigma) = P_s(V_1, \sigma)P_s(V_2, \sigma) \tag{2.38}$$

Considering Eq.2.38 to be the basic equation, the boundary condition given by Eq.2.35 is easily proved as follows,

$$P_s(V + 0, \sigma) = P_s(V, \sigma) = P_s(V, \sigma)P_s(0, \sigma) \tag{2.39}$$

from which $P_s(0, \sigma) = 1$. This demonstrates the equivalence of the unicity theorem and the boundary condition $P_s(0, \sigma) = 1$.

Functional Eq.2.38 was solved by Euler, and it may be detailed below since it imparts some clarity to this topic concerning statistics. The following development is easily obtained.

$$\begin{aligned}
P_s(V + \Delta V, \sigma) &= P_s(V, \sigma)P_s(\Delta V, \sigma) \\
&= P_s(V, \sigma) + P'_s(V, \sigma)\Delta V
\end{aligned} \tag{2.40}$$

and the same may be said for the following development,

$$\begin{aligned}
 P_s(\Delta V, \sigma) &= P_s(0, \sigma) + P'_s(0, \sigma)\Delta V \\
 &= 1 + P'_s(0, \sigma)\Delta V
 \end{aligned} \tag{2.41}$$

Eqs.2.40 and 2.41 give,

$$\begin{aligned}
 P_s(V, \sigma)P_s(\Delta V, \sigma) &= P_s(V, \sigma)[1 + P'_s(0, \sigma)\Delta V] \\
 &= P_s(V, \sigma) + P_s(V, \sigma)P'_s(0, \sigma)\Delta V \\
 &= P_s(V, \sigma) + P'_s(V, \sigma)\Delta V
 \end{aligned} \tag{2.42}$$

Using the equations above, the expression obtained is,

$$P_s(V, \sigma)P'_s(0, \sigma) = P'_s(V, \sigma) \tag{2.43}$$

and finally,

$$\frac{P'_s(V, \sigma)}{P_s(V, \sigma)} = P'_s(0, \sigma) = -\frac{\phi(\sigma)}{V_o} \tag{2.44}$$

$$\phi(\sigma) > 0$$

where, V_o = the unit volume, and, $\phi(\sigma)$ = the specific-risk function (or, Weibull's function) is a positive quantity because P_s is positive and monotonously increasing, which means that P'_s must be negative. Eq.2.44 can also be expressed as,

$$\frac{\frac{dP_s(V, \sigma)}{dV}}{\frac{P_s(V, \sigma)}{V_o}} = -\phi(\sigma) \quad (2.45)$$

Eq.2.45 gives the specific rate of the decreasing increment of the bodies that have not fractured owing to a volume increasing. On integrating Eq.2.45, we have,

$$\ln P_s(V, \sigma) = -\frac{V}{V_o} \phi(\sigma) + C \quad (2.46)$$

$$\text{or, } P_s(V, \sigma) = \exp\left\{-\frac{V}{V_o} \phi(\sigma) + C\right\} \quad (2.47)$$

In order to fulfill the boundary condition given by Eq.2.35, C must be zero. Eq.2.47 gives

$$P_s(V \rightarrow \infty, \sigma) \rightarrow 0$$

$$\text{or, } P_s(\infty, \sigma) = 1 \quad (2.48)$$

which means that a large size body has great defects and can be broken under any stress.

By rearranging Eq.2.47, one obtains the celebrated Weibull formula,

$$P_f(V, \sigma) = 1 - \exp\left\{-\frac{V}{V_o} \phi(\sigma)\right\} \quad (2.49)$$

where, $P_f(V, \sigma) = 1 - P_s(V, \sigma)$ = the cumulative probability of fracture.

The properties of $P_f(V, \sigma)$ are as follows,

$$0 \leq P_f(V, \sigma) \leq 1$$

$$P_f'(V, \sigma) \geq 0 \quad (2.50)$$

$$0 \leq \sigma \leq \infty \quad 0 \leq V \leq \infty$$

The stress under which P_f is zero is called the limit stress σ_L . When $P_f = 1$ the stress under which this occurs is called the highest-limit stress, σ_S .

Experimental results are in general in accord with the following analytical form proposed by Weibull [32],

$$\phi(\sigma) = \begin{cases} \left(\frac{\sigma - \sigma_L}{\sigma_o} \right)^m & \sigma \geq \sigma_L \\ 0 & 0 \leq \sigma \leq \sigma_L \end{cases} \quad (2.51)$$

where, σ_o and m are the Weibull's parameters and are fabrication constants. The Weibull modulus, m , shows the amount of variability in the nature of the group(s) of data under consideration. For example, a low value for modulus depicts a highly scattered data.

Another formula was given by Kies [34] as follows,

$$\phi(\sigma) = \begin{cases} \left(\frac{\sigma - \sigma_L}{\sigma_S - \sigma} \right)^m & \sigma_L \leq \sigma \leq \sigma_S \\ 0 & \sigma < \sigma_L \\ \infty & \sigma > \sigma_S \end{cases} \quad (2.52)$$

2.9.2. Application of Weibull Modeling to Material Failure

Considerable work has been focused on the mechanisms of failure within metal-matrix composites. Failure mechanisms such as matrix/reinforcement debonding [35, 36], particle cracking [37-41] and ductile failure in the matrix [42] have been previously observed. The actual mechanism of failure may depend on many factors, including, the interface strength, the reliability and strength of the reinforcement, the processing route [42], etc. Lewis and Withers [43] investigated the occurrence of reinforcement cracking within a particulate ZrO₂/2618 Al alloy metal matrix composite under tensile plastic straining, with specific focus on the dependence of fracture on particle size and shape. The probability of particle cracking was modeled using a Weibull approach, which was consistent with experimental data. Weibull modulus values and the stress required to crack the particles were found to be within the range expected for ceramic particle cracking. Caceres and Griffiths [44] observed cracking of silicon particles (of different morphologies produced by varying the solidification rate and length of solution treatment) during plastic deformation. The number of cracked particles increased with applied strain. The larger and longer particles were found to be more prone to cracking. Coarse particles cracked very rapidly even at lower strains, while cracking of fine particles occurred in a more gradual manner. The cracking of silicon particles was described using Weibull statistics, with the stresses in particles calculated using dispersion hardening theories. It was concluded that Weibull distribution can express the ductility of an alloy as a function of the dendrite cell size, together with the average size and aspect ratio of the cracked silicon particles, assuming that fracture occurs when a critical level of damage is attained. On the other hand, Danzer et al. [45] stated that

Weibull distribution is not followed by brittle materials containing bi- or multi-modal flaw distributions, surface and volume flaws, a high defect density, internal residual stress fields or showing a *R*-curve behaviour. It was also believed that Weibull statistics is not applicable to very small specimens, or if the applied stress field presents high gradients. In all the above mentioned cases, the Weibull modulus (*m*) is no longer a constant and depends on the applied stress amplitude. The real strength distribution can be understood only from test specimens with different volumes.

2.10. Deformation-induced Phase Transformation in Silicon

Silicon is known to undergo a series of phase transitions when subjected to high pressure, and also during pressure release [46]. A number of indentation tests have been carried out on different crystallographic planes of single crystal silicon in order to study high pressure phase transformation in silicon, and 12 different polymorphs have been observed so far [47-49]. Under a hydrostatic pressure of 11.2-12.0 GPa, diamond cubic structured Si-I phase transforms into a metallic β -tin structured Si-II phase [50]. This transformation is associated with a 22% increase in density [51]. A hexagonal diamond structured Si-IV phase may form directly from Si-I in the presence of shear stresses at twin sections, without preceding transformation to Si-II [52]. At fast unloading rates of the indenter, Si-II transforms into an amorphous state, whereas a mixture of rhombohedral-structured Si-XII and bcc-structured Si-III phases form at slower unloading rates. On annealing, the above mentioned high pressure phases of silicon transform to Si-IV at moderate temperatures but at higher temperatures, reversal to Si-I occurs [53]. **Fig. 2.30** is a schematic diagram of various pressure-induced phase transformations in silicon. Kovalchenko et al. [54] studied oil-lubricated sliding contact-

induced phase transformations in bulk silicon, and observed that a metallic Si-II phase was formed and underwent plastic flow.

Phase transformations during indentation on silicon have been reported by a number of authors [55-59]. Si-I to Si-II transformation is indicated by a “pop-in” in the loading curve. Transformation of Si-II to a mixture of Si-II and Si-XII or amorphous Si is indicated by a “pop-out” in the unloading curve, though Jang et al. [60] suggests that such events are not necessary conditions for phase transformations in silicon.

2.11. Dislocation Mobility in Diamond Cubic (DC) Structure

Silicon exists in the DC structure, which can be thought of as a face centered cubic lattice with two atoms per lattice site; one at (0,0,0) and the other at $\left(\frac{1}{4}, \frac{1}{4}, \frac{1}{4}\right)$ [61].

Silicon is covalently bonded and has a large Peierls stress. Dislocations in silicon are similar to those in face centered cubic materials, but at low temperatures the high Peierls stress confines them largely to the $\langle 110 \rangle$ valleys. At low temperatures, slip occurs on $\{111\}$ planes in the $\langle 110 \rangle$ directions with the Burgers vector $\frac{1}{2}\langle 110 \rangle$. Three types of dislocations are predominantly observed: a screw dislocation, and two 60° dislocations; although at high temperatures, a pure edge dislocation and others may be observed. Dislocations in silicon are shown to be dissociated in most cases [62]. The screw dislocation dissociates into two 30° partials, and the 60° dislocation dissociates into an edge dislocation (90°) and a 30° partial [62].

These dislocations may occur on the widely-spaced shuffle planes, or on the narrowly-spaced glide planes. The slip configuration is shown in **Fig. 2.31**, projected along the $\langle 110 \rangle$ direction. Formation of a dislocation in the shuffle configuration

requires the removal of a half plane along path 1234. This results in the formation of one dangling bond, which is normal to the glide plane. Formation of a dislocation in the glide configuration requires the removal of a half plane along 1564. This results in the formation of three dangling bonds, but they remain at a small angle to the glide plane. This shallow angle makes it possible for the glide set dangling bonds to reconstruct easily, thus lowering the dislocation energy. Reconstruction of the shuffle set dangling bonds would require much larger displacements. Recent work suggests that the dislocations lie in the glide configuration [63]. It is energetically favourable for the 30° partial to reconstruct, although the results are not clear for the 90° partial [63].

Partial dislocations have been observed to move together in silicon, but having differing mobility, which may lead to a large non-equilibrium spacing of the partials [64]. The mobility of the dislocation depends on which partial is leading, and which is trailing. Wessel and Alexander [65] reported that the mobilities are of the order $90_l^\circ > 90_t^\circ > 30_l^\circ > 30_t^\circ$, where, 90° and 30° refer to the dislocation type, and l or t refer to whether that partial is leading or trailing, respectively. The observation can be rationalised by considering that reconstruction has occurred in some of the partials, and considering that the lead partial moves into a perfect lattice, while the trailing partial moves into a stacking fault [64].

Dislocations also move into the material below the indentation, with Burgers vectors inclined to the surface. Transmission electron microscopy of dislocation rosettes revealed only dislocations associated with stacking faults [66]. Dislocations were of the $\frac{1}{6}\langle 211 \rangle$ Shockley type [67]. Dislocations with Burgers vectors inclined to the surface may interact to form a sessile dislocation, which can serve to nucleate cracks,

$$\frac{1}{6}[\bar{1}2\bar{1}] + \frac{1}{6}[1\bar{1}2] = \frac{1}{6}[011] \quad (2.53)$$

Undissociated dislocations may also react to form Lomer locks,

$$\frac{1}{2}[\bar{1}10] + \frac{1}{2}[0\bar{1}1] = \frac{1}{2}[\bar{1}01] \quad (2.54)$$

Either of these reactions reduces the energy of the dislocation by reducing the magnitude of the Burgers vector.

Whether or not a crack propagates in a material depends on the mobility of the dislocations in that material. Crack propagation depends on a competition between crack-tip decohesive forces, and the force necessary for dislocation emission; a model proposed by Kelly, Tyson and Cottrell [68]. If the stress intensity factor for fracture is reached before the critical stress for dislocation emission, the material behaves in a brittle manner. On the other hand, if dislocations are emitted from the crack-tip, the local conditions at the crack-tip are modified in two ways: (1) the dislocations emitted from a crack exert a back stress on the crack, effectively reducing the local stress intensity factor. This is known as *crack-tip shielding*; (2) the crack-tip can also be blunted by dislocation emission. The emission of dislocations of edge character with a Burgers vector normal to the fracture plane will blunt the crack-tip, while screw dislocations can jog the crack-tip [69]. This effect is known as *crack-tip blunting*.

Dislocations may also be nucleated by sources in the material near the crack-tip. The dislocations, once emitted, are strongly repelled by the crack-tip. Three forces act upon the dislocation: (1) the stress field surrounding the crack-tip, which repels the dislocations from the crack tip, (2) the *image force*, which attracts the dislocation to the

crack-tip, and (3) the *edge force*, which is a surface tension (attractive) force due to the creation of new surface at the crack-tip.

The interaction of these three forces creates a position of unstable equilibrium. Once this position is crossed, the dislocation is repelled strongly and moves away from the crack-tip until it encounters some obstacle [70]. TEM observations by Ohr [71] showed that dislocations moved rapidly away from the crack-tip, leaving a small dislocation-free zone (DFZ) around the tip. Ohr suggested that this DFZ results from the short range of the image force attracting the dislocations to the crack-tip. As a result, the dislocations always experience a repulsive force. Li [72] suggested that this is because the dislocations around the crack retract inwards after unloading.

Dislocations from sources near the tip may also play a role, as they are attracted or repelled from the crack-tip. Dislocations repelled by the crack-tip come to rest in dense tangles some distance away from the plastic zone, which shields the crack tip from the applied stress. This process, however, may not continue indefinitely. Dislocations may interact to produce pile-ups and wedge-shaped edge defects dependent on slip geometry in the material [73].

The stress intensity factor, K , required for dislocation emission has been derived as [69],

$$K = (2Gb\sigma)^{\frac{1}{2}} \quad (2.55)$$

where, G is the shear modulus, σ is the yield stress, and b is the magnitude of the Burgers vector. Thus, the stress required for dislocation emission is proportional to the square root of the flow stress. While dislocation emission from crack tips is a necessary but not a

sufficient condition for plasticity [74], dislocations must be able to move away from the tip rapidly enough to avoid the creation of a brittle condition.

2.11.1. Microhardness-induced Dislocation Generation

Although hardness testing is usually employed to determine the hardness or fracture toughness of a material, it may also be used to investigate related phenomenon. Microhardness testing can be used to investigate dislocation mobility. By using a hot microhardness tester, the ductile-brittle transition temperature (DBTT) for a material displaying this behaviour may be determined.

Just as microhardness testing simplifies obtaining the strength and fracture properties of a material, it also simplifies dislocation mobility studies. A typical non-microhardness method involves generating dislocation sources in material (e.g. by scratch) and applying successive stress pulses. Since the dislocation moves during the time at which the stress is applied, measurement of successive dislocation positions, by chemical etching, gives the dislocation velocity. This is known as the *double etch pit technique*. This method is as difficult as mechanical bend testing with all the same complexities. Another traditional method, *Lang Topography*, is used to dynamically measure dislocation velocities. This technique, which is based on an X-Ray method, is limited to thin specimens, and requires long exposures and intense radiation sources. Qualitative measurements of dislocation mobility can be made easily and rapidly by using microindentation test methods.

Hot microhardness testing was used to investigate dislocation mobility in silicon and germanium [75]. High purity, dislocation-free single crystals of these materials are available, and can be easily prepared and indented. After indenting, etching with an

appropriate etchant reveals arrays of dislocations (rosettes) generated by indentation. The extent of these rosettes can reveal information about dislocation mobility.

2.11.2. Investigation of Indentation Defect Structure in Silicon

As seen in Section 2.10, when indented at room temperature with a sharp indenter, crystalline silicon transforms into various types of high-pressure phases, which are formed in the highly stressed defect structure below the indentation, as reported in previous research performed with silicon single crystal. The details of the mechanism of amorphization of silicon under the application of shear stress are not very well known. Though silicon is considerably brittle at room temperature, under a hydrostatic pressure it may show some amount of ductility [76]. Therefore, existence of dislocations is expected in the defect structure of an indentation where a hydrostatic pressure and a shear stress coexist. Observation of the indentation defect structure under a TEM proved that this amorphization is induced by dislocation motion during plastic deformation [76 - 78]. Tachi et al. [76] suggested that this dislocation activity may lead to amorphization, although the exact mechanism is not clear. Ge et al. [79] concluded that in the process of slow unloading, mutual interaction of dislocations causes gradual lattice rotation, which results in the formation of a perfect crystalline lattice in due course. But in case of fast unloading, time required for this mutual interaction is very short. This phenomenon, along with excessive dislocation annihilation, may result in extensive lattice distortion resulting in the formation of an amorphous structure. Suzuki and Ohnuma [80] suggested that at higher temperatures, when dislocation climb takes place, regular crystal structure may be restored in silicon.

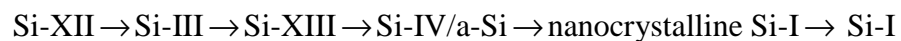
2.12. Temperature-induced Phase Transformations in Silicon

Though extensive research has been conducted on the metastable silicon phases produced by nanoindentation, very little has been reported regarding their thermal stability in the residual imprints. Hernandez et al. [81] performed micro-Raman spectroscopy on the silicon particles in Al-Si hypereutectic alloys in both liquid and semi-solid states. Quenching operations, with 390.1 Al-Si alloy, from liquid and/or semi-solid states conducted at cooling rates of 100°C/s were high enough to freeze the molten sample, thus allowing subsequent Raman analysis. Results revealed that the silicon agglomerates and the primary silicon particles had stressed and/or non-bonded silicon atoms at high temperatures, resulting in distorted lattices. The intensity of such stresses in silicon decreases with temperature, up to the end of solidification (solidus temperature 470°C). Both Si-XII and Si-III are metastable in ambient conditions, and are expected to transform into Si-I according to enthalpy calculations [82]. However, such transformations have not been observed experimentally. Instead, another metastable phase, the hexagonal diamond structured Si-IV, was observed after moderate heating of the Si-III samples recovered after pressurization in high-pressure cells [83-85]. The stability of Si-III was reported to be strongly temperature sensitive. The estimated “lifetime” of Si-III varied from over 100 years at room temperature, to only a few minutes at 200°C [86]. Si-IV was also shown to form directly from the Si-I when indentations were performed at elevated temperatures (350-550°C) [87, 88]. According to Pirouz et al. [88] and Dahmen et al. [89], the Si-I→Si-IV transformation occurs by double twinning in Si-I, with the resultant Si-IV phase appearing as ribbons or platelets embedded in Si-I around the indented area. The reported Raman spectra assigned to Si-IV

exhibit a rather broad, asymmetric band centered at $\sim 510 \text{ cm}^{-1}$ [86, 90] making it difficult to distinguish from nanocrystalline Si-I, which is characterized by a similar spectrum [91]. Moreover, Raman microspectroscopy studies of the temperature effect on phase stability in silicon nanoindenters reported the formation of an unidentified silicon structure around 150-250°C, that had at least four characteristic Raman bands at 200, 330, 475, and 497 cm^{-1} [92]. Domnich and Gogotsi [92] designated the new phase Si-XIII and proposed the following phase transformation sequence upon heating the residual hardness imprints in silicon:



However, the mechanisms of the above phase transitions and the corresponding microstructural changes in silicon nanoindenters have never been explored in detail. Ge et al. [93] explored the temperature effects on the metastable phases in silicon nanoindenters by use of Raman microspectroscopy analysis combined with in-situ experiments in a TEM hot stage and found that the transformation of Si-III and Si-XII into other structures begins at $\sim 175^\circ\text{C}$. Raman spectra suggested the formation of an unidentified ‘‘Si-XIII’’ phase at temperatures of $\sim 200^\circ\text{C}$, which precedes the formation of Si-IV. The in-situ heating experiment at 200°C in TEM showed that different transformation paths exist for the metastable Si phases. It was also proposed that amorphization during heating proceeds by a distortion-induced disorder mechanism. The phase transformation sequence during heating was established as,



2.12.1. High Temperature Deformation of Silicon due to Indentation

Microstructural investigations of temperature-dependent deformation around sharp indentations on highly brittle ceramics like, single crystal SiC, Si₃N₄ and B₄C was performed by Naylor and Page [94]. It was observed that radial and lateral crack dimensions increased at elevated temperatures, mainly due to increasing radial stresses around indentations caused by increasing plasticity. Arguirova et al. [95] used Rockwell indentations on Cz-silicon (wafer) at elevated temperatures (70°C-600°C) and observed strong residual compressive stresses (up to 2.25 GPa) at the centre of the residual indents while the stresses at the boundary were tensile in nature. Metastable crystalline phases of silicon, like Si-III, Si-IV and Si-XII, were observed, including traces of amorphous silicon. Observations of regions away from the indentations (at different temperatures) proved to be interesting. High density of relaxation cracks was observed up to 400°C, where the material continued to remain unstressed. Apart from Si-I, Raman shifts due to Si-IV had high intensity at this temperature. At temperatures between 500°C and 600°C, a transition occurred from the tensile stress at the boundary to compressive stresses as the distance increased (more than 40 µm) from the indents. Such regions were associated with low crack density. At temperatures higher than 600°C, crack density decreased to zero.

2.13. A Short Summary of the Literature Survey

Evidently, previous investigations on sharp contacts have been directed towards determining the associated stress fields and resultant crack systems. A considerable amount of research has been focussed on indentations performed on the polished crystallographic surfaces of bulk silicon. Stress-induced phase transformations in silicon

have been investigated only for developing silicon as a semi-conducting material for its enormous application in the electronic industry. Dimensional analyses have shown that indentation pile-up and sinking-in depends on the material properties, however, research is needed to systematically quantify and understand the reasons of pile-up (as a function of the indentation load), and comprehend the actual cause of crack formation by directly investigating the subsurface defect structure. Observing indentation-induced damaged structure (by using state-of-the art techniques including ion-milling and in-depth transmission electron microscopy) in small volumes like the second phase silicon particles (less than 100 μm) in Al-Si alloys is a challenge and, quite clearly, the next stage in the direction of current research on sharp contact mechanics.

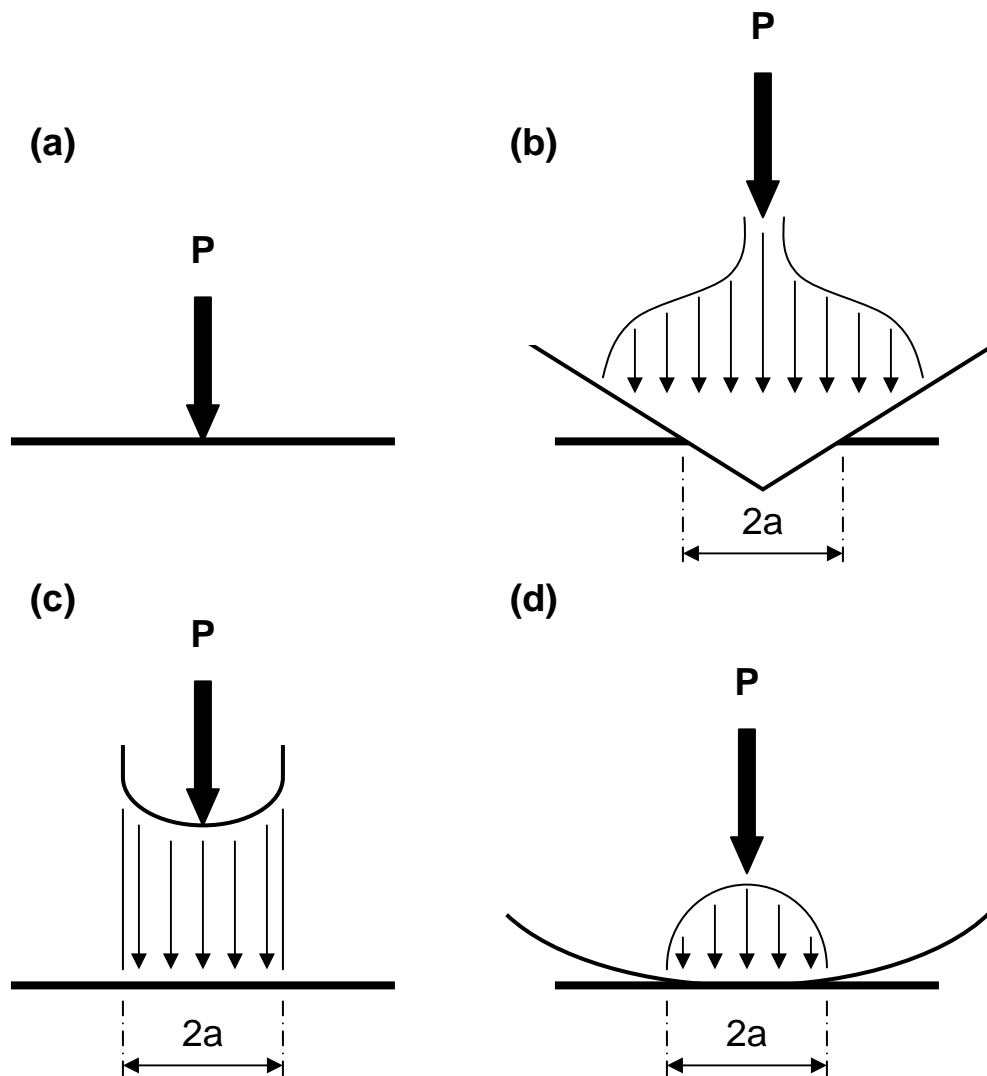


Fig.2.1: Elastic contact pressure distributions for various indentation systems; **(a)** point load, **(b)** sharp indenter, **(c)** flat punch, **(d)** sphere (or cylinder). P and a characterize the extent of applied loading and resulting contact respectively [13].

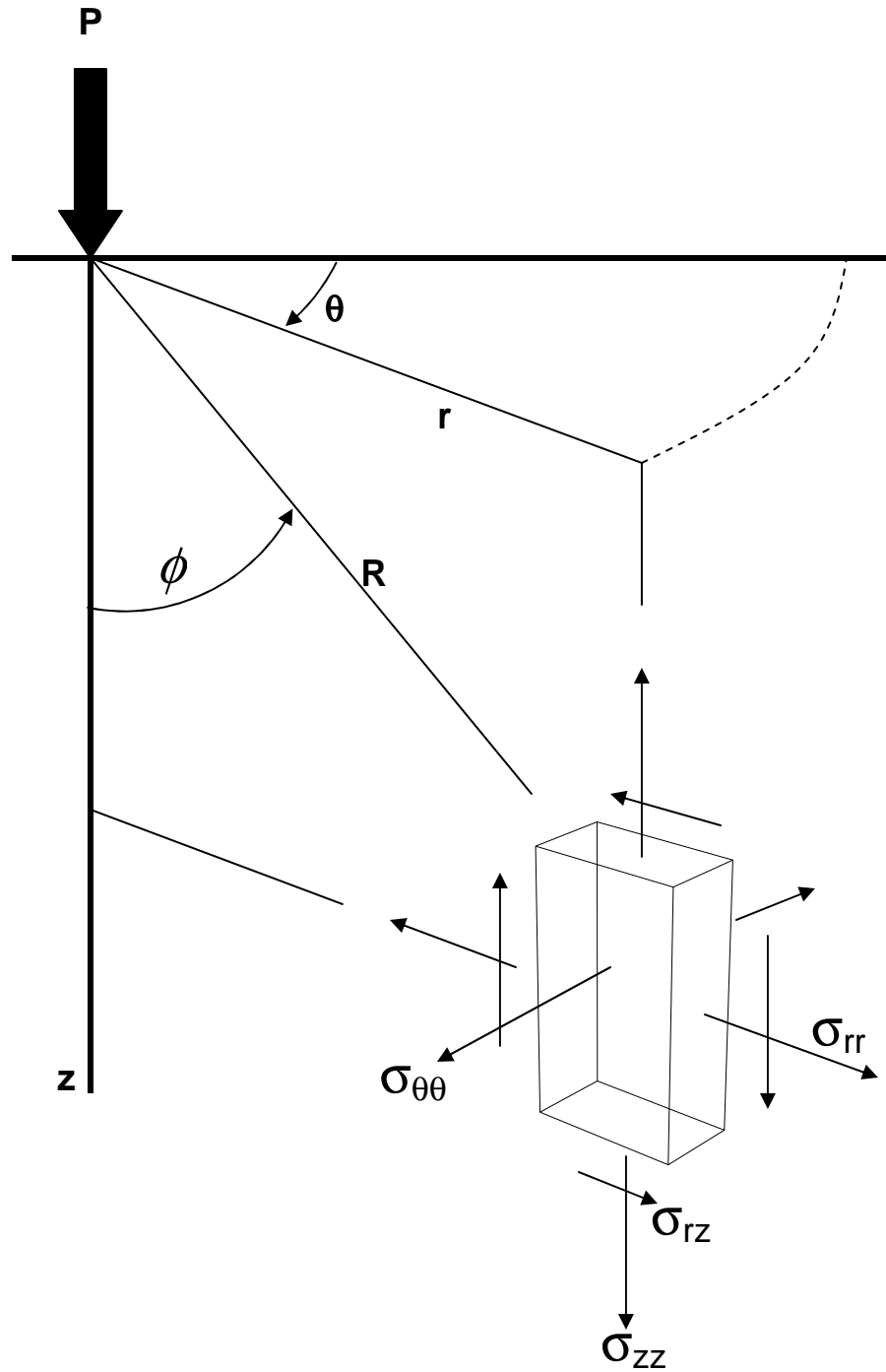


Fig.2.2: Coordinate system for axially symmetric point loading P . Expressions for the stress components indicated are given in the Appendix (p-138) [14].

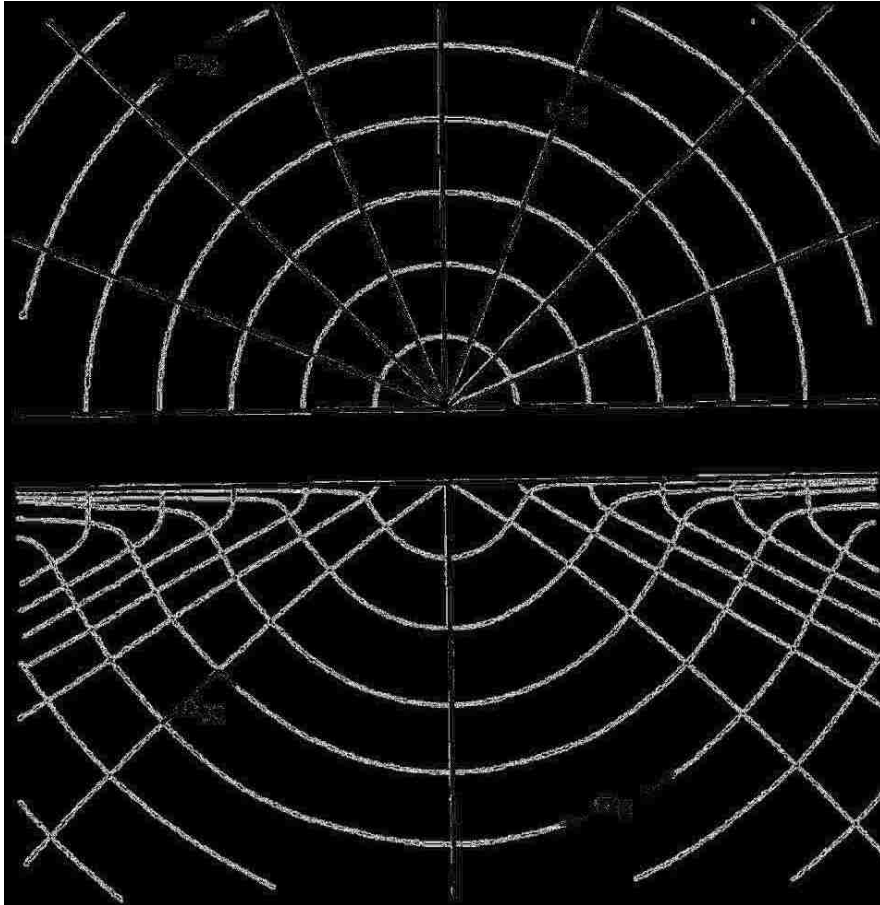


Fig.2.3: Half-surface view (top) and side view (bottom) of stress trajectories in Boussinesq field. Plotted for $\nu = 0.25$ [14].

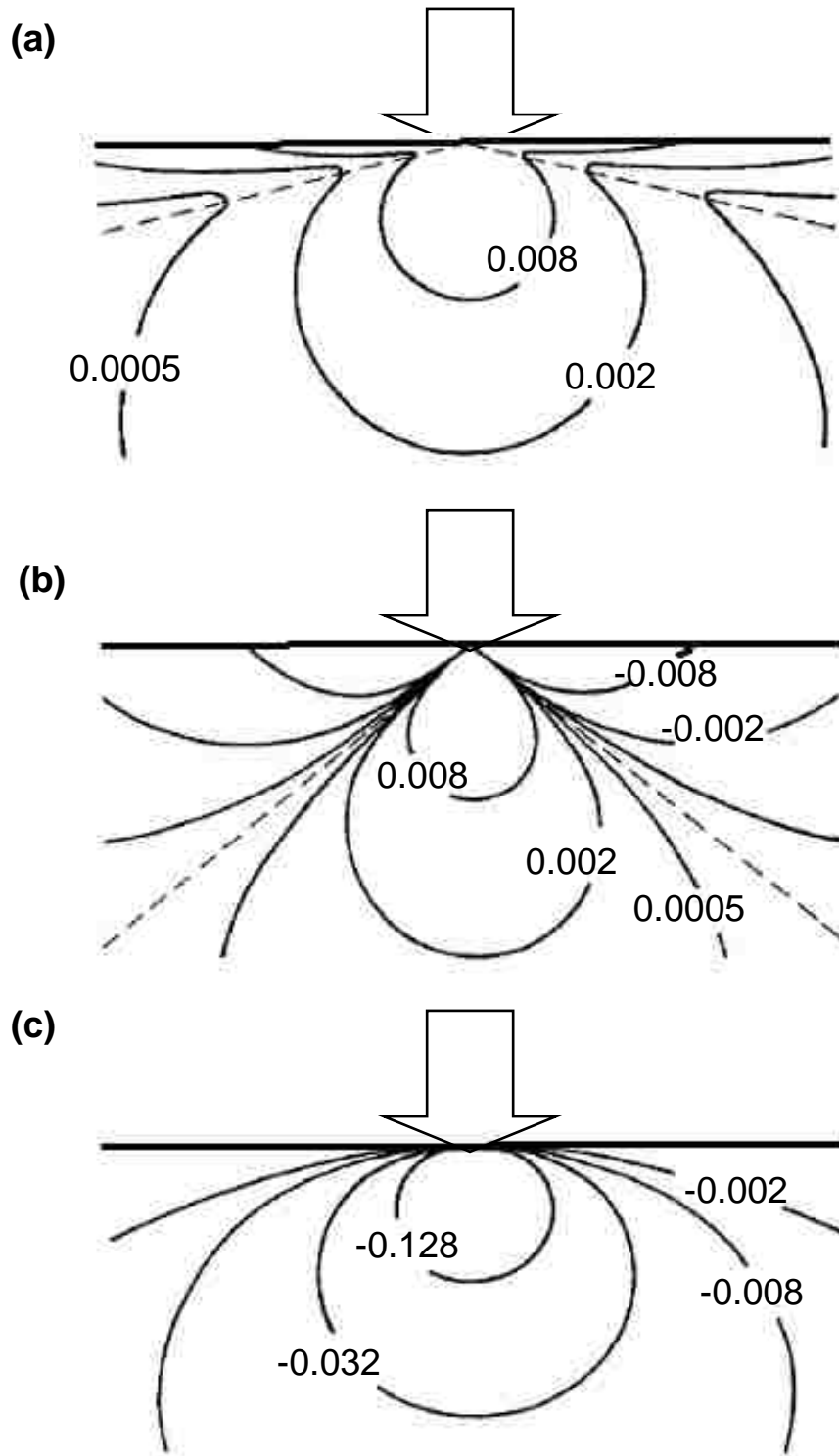


Fig.2.4: Contours of principal normal stresses, (a) σ_{11} , (b) σ_{22} , and (c) σ_{33} , in Boussinesq field, shown in plane containing contact axis. Plotted for $\nu = 0.25$. Unit of stress is p_o , contact “diameter” (arrowed) is $2a\sqrt{\alpha}$. Sharp minimum in σ_{11} and zero in σ_{22} are indicated by broken lines in (a) and (b) respectively [14].

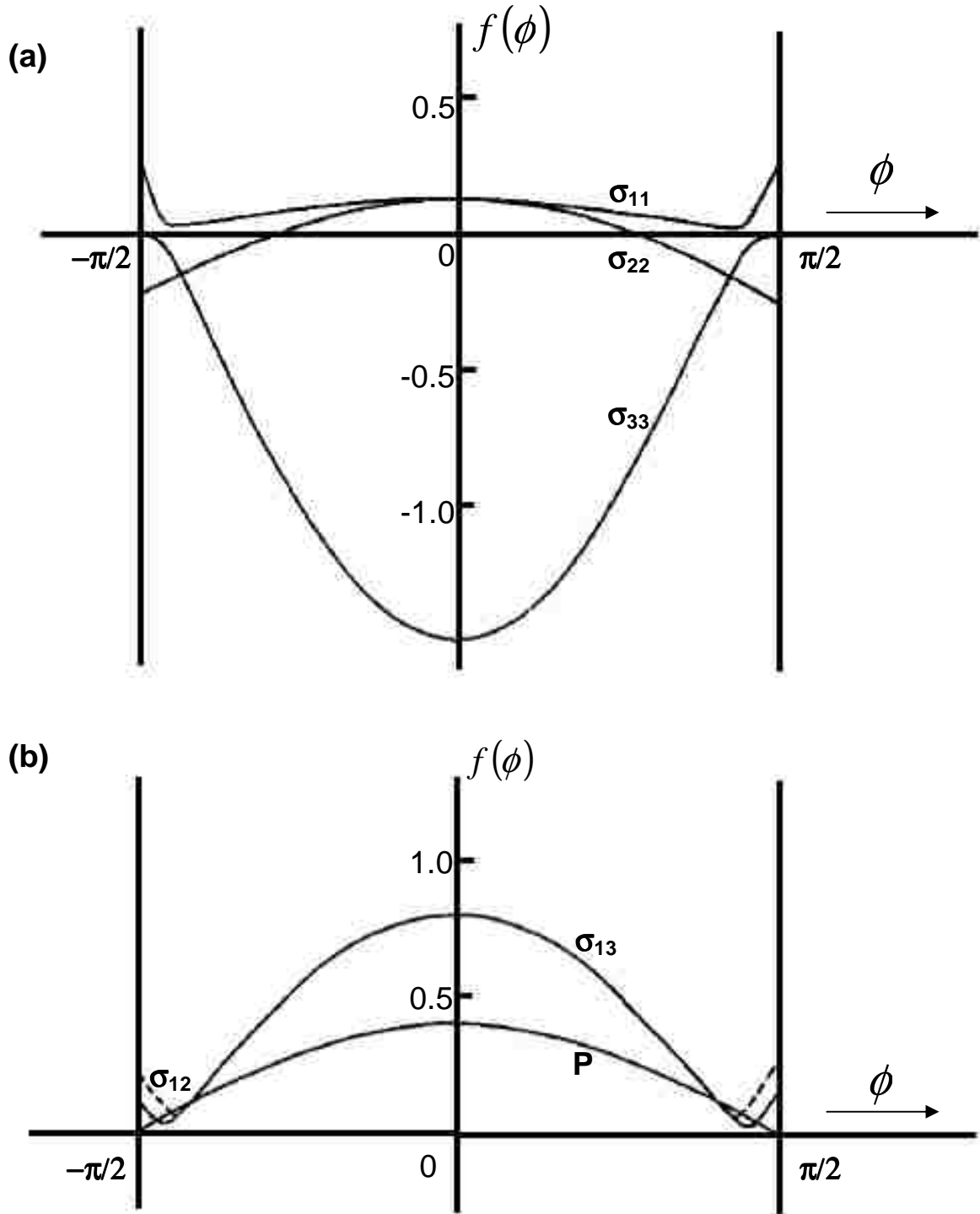


Fig.2.5: Angular variation of principal stress components in Boussinesq field, plotted in terms of dimensionless function $f(\phi)$ (Eq.2.6) (a) Principal normal stresses, σ_{11} , σ_{22} , and σ_{33} ; (b) Maximum principal shear stress σ_{13} or σ_{12} (broken line), and hydrostatic compression, p . Plotted for $\nu = 0.25$ [14].

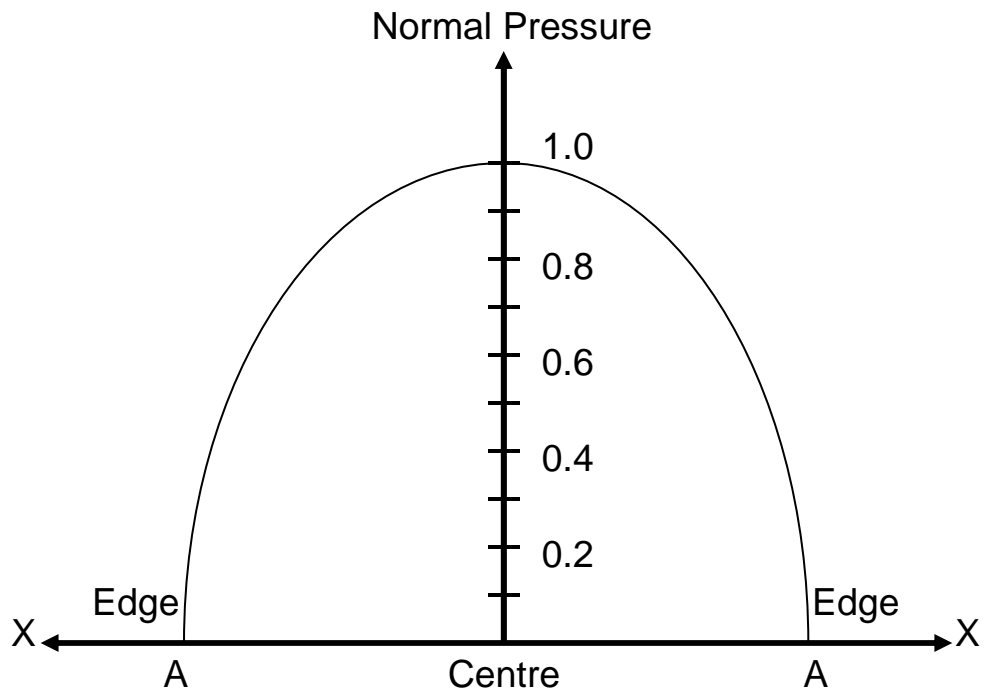


Fig.2.6: Pressure distribution over circle of contact when a flat surface is deformed elastically by a sphere [15].

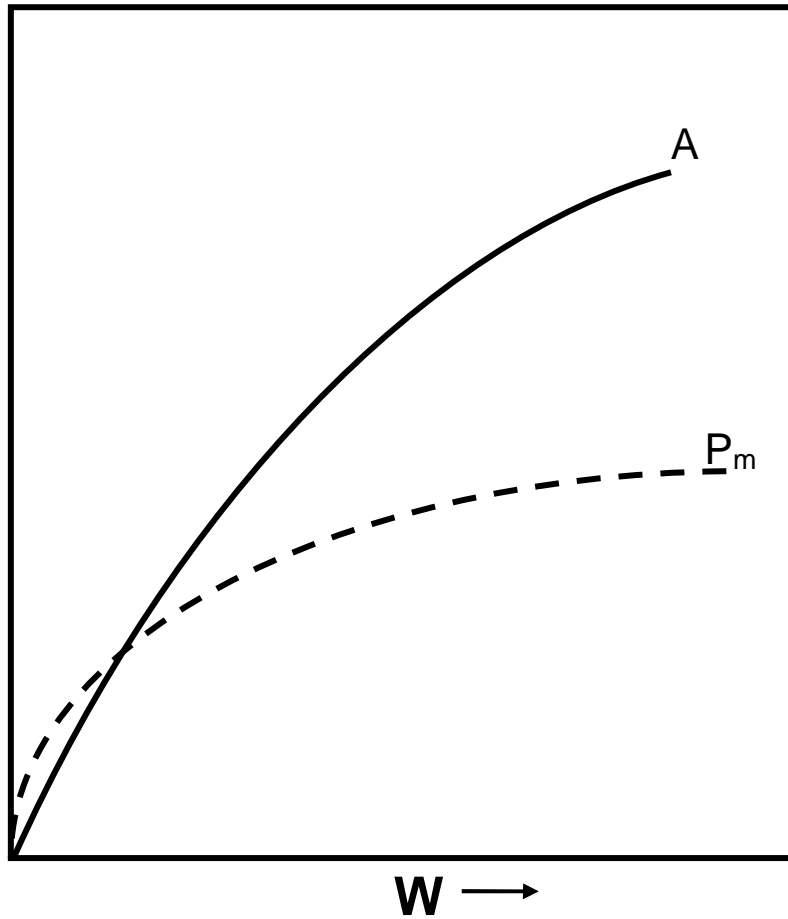


Fig.2.7: Elastic deformation of a flat surface by a sphere: the area of contact A is proportional to $w^{\frac{2}{3}}$ and the mean pressure P_m over the region of the contact is proportional to $w^{\frac{1}{3}}$ [15].

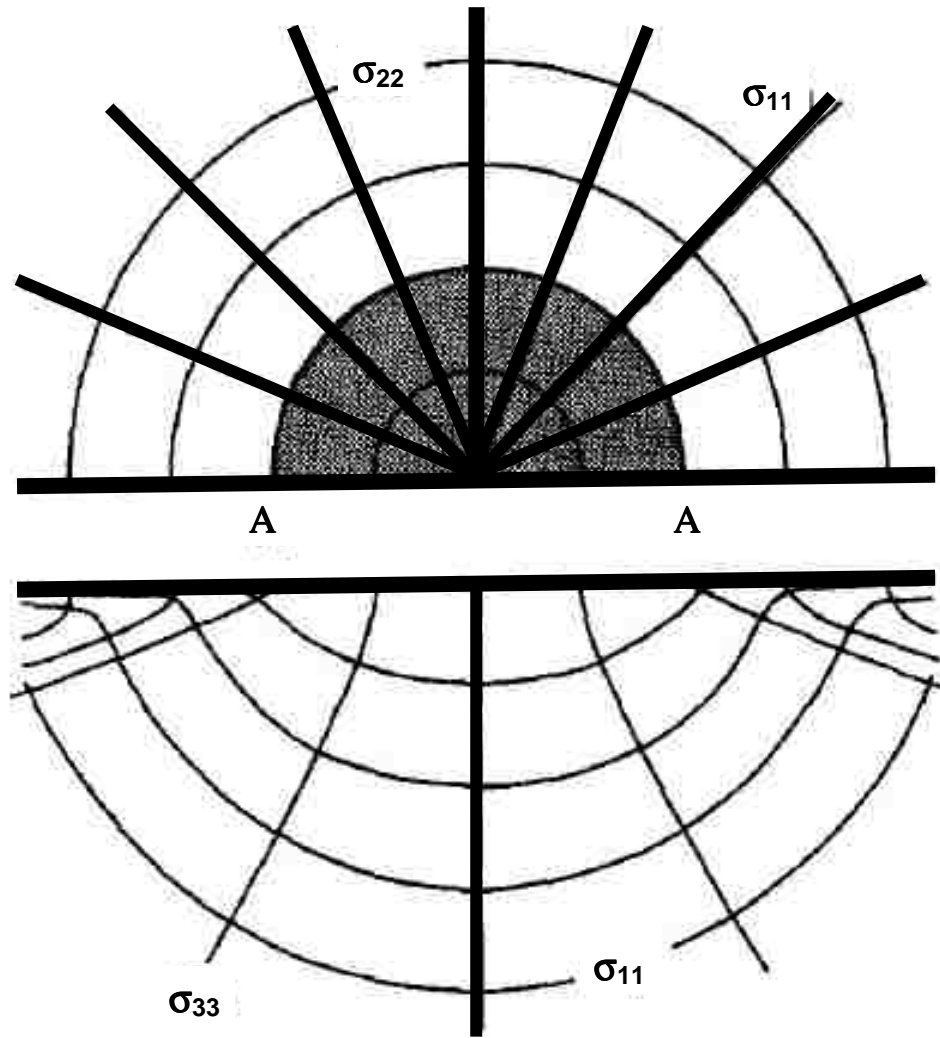


Fig.2.8: Half-surface view (top) and side view (bottom) of stress trajectories in Hertzian field. Plotted for $\nu = 0.33$, contact diameter AA is $2a$ [19].

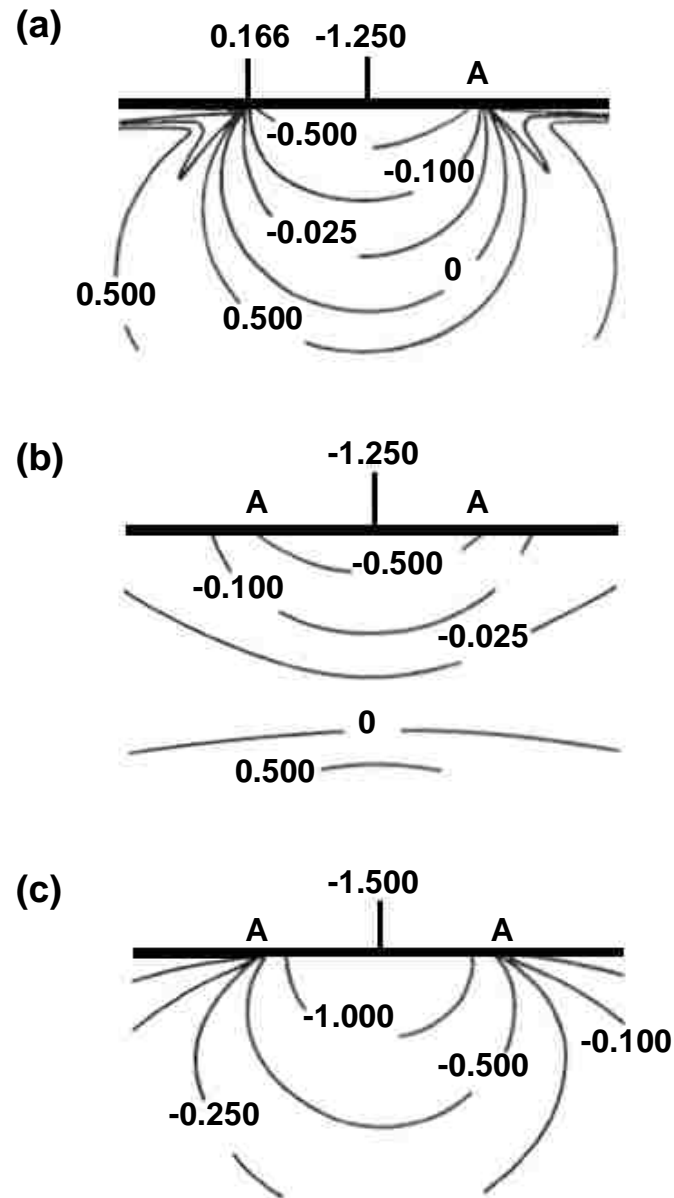


Fig.2.9: Contours of principal normal stresses, (a) σ_{11} , (b) σ_{22} , and (c) σ_{33} , in Hertzian field, shown in plane containing contact axis. Plotted for $\nu = 0.33$. Unit of stress is p_0 , contact diameter AA is $2a$ [19].

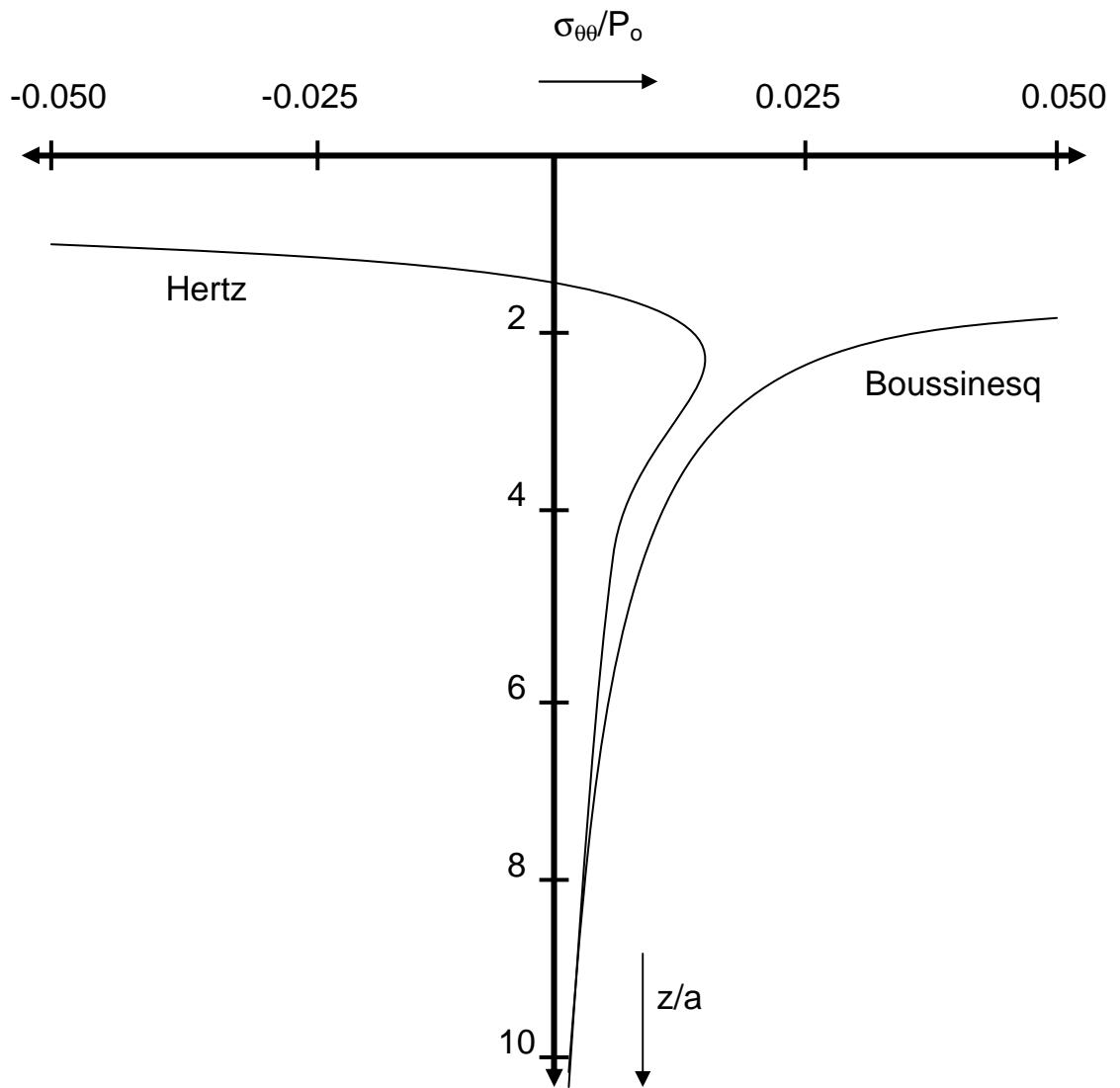


Fig.2.10: Comparison of $\sigma_{\theta\theta}(z)$ stress terms for Boussinesq and Hertzian stress fields. Plotted for $\nu = 0.25$. Divergence of curves in vicinity of contact zone is observed (at $z \rightarrow 0$, $\sigma_{\theta\theta} \rightarrow \infty$ in the Boussinesq field, $\sigma_{\theta\theta} \rightarrow -1.125 p_o$ in the Hertzian field) [14].

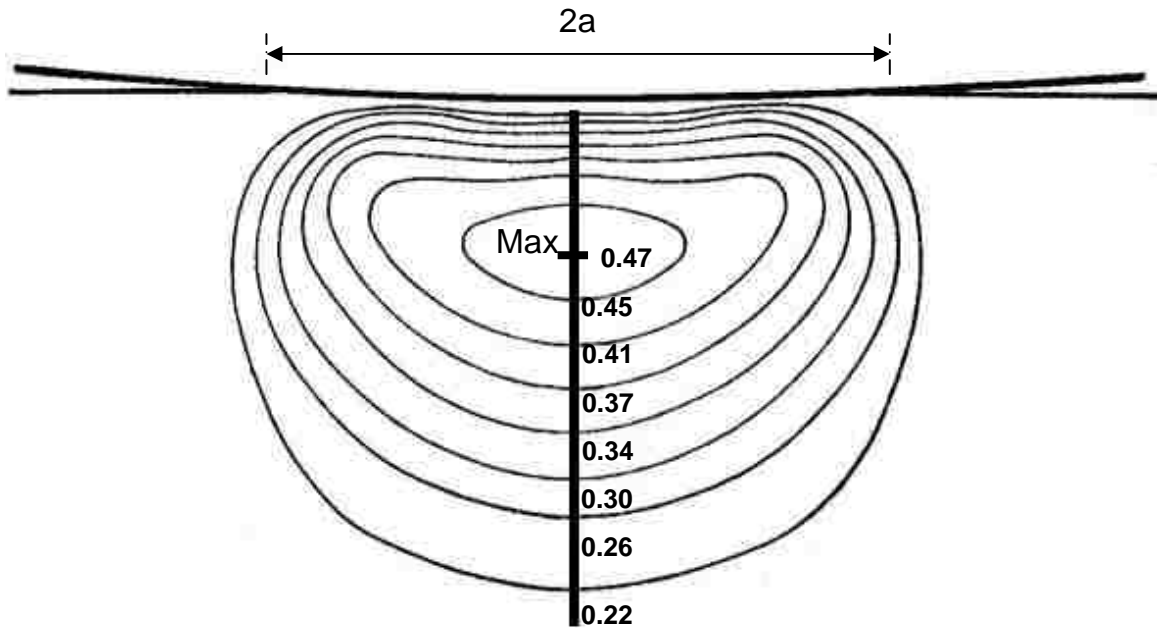


Fig.2.11: Elastic deformation of a flat surface by a sphere, showing the maximum shear stress in the bulk material below the deformed surface. The maximum shear stress occurs below the below the centre of the circle of contact has a value of $0.47 P_{mean}$, where P_{mean} is the mean pressure. Plastic deformation first occurs at this point when the shear stress $=0.5Y$, i.e., when $P_{mean} \approx 1.1Y$, where Y is the yield stress of the material [15].

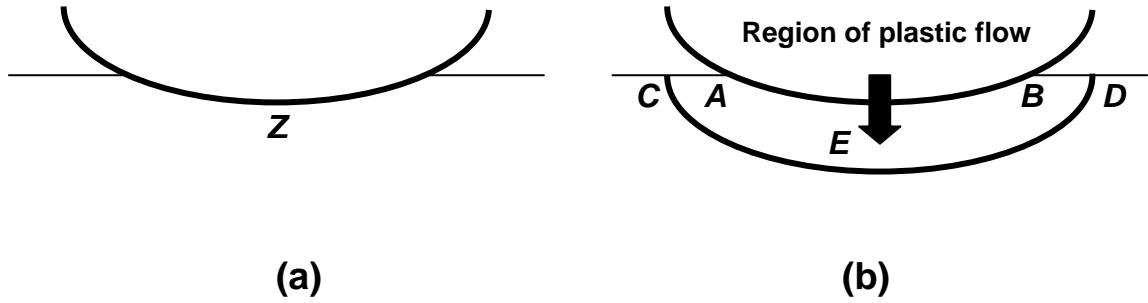


Fig.2.12: Plastic deformation of an ideally plastic metal by a spherical indenter: (a) the onset occurs at a localized region Z when $p_o \approx 1.1Y$; (b) at a later stage the whole of the material around the indenter flows plastically [15].

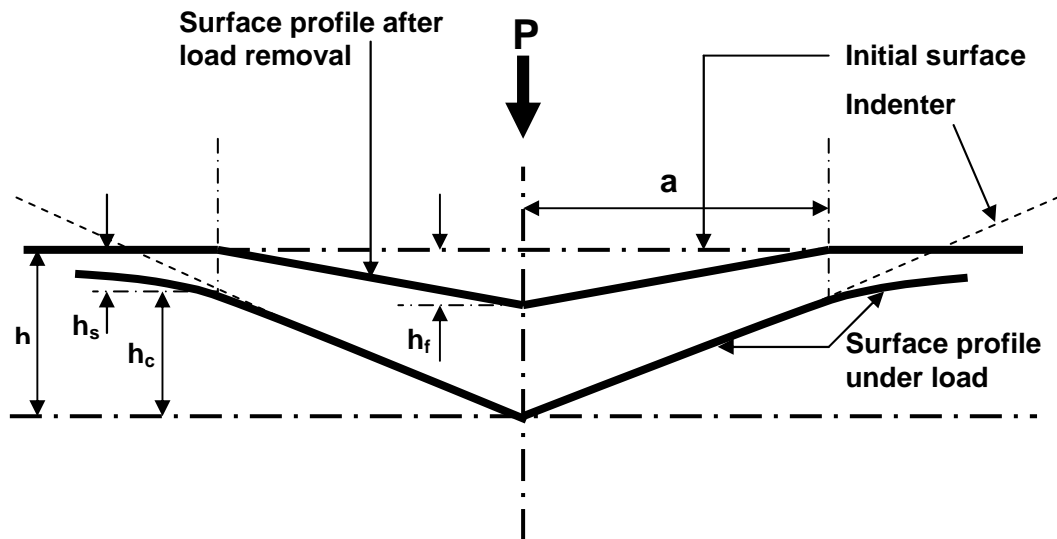


Fig.2.13: A schematic representation of a section through an indentation showing various quantities; P = the applied load; h = total displacement (Eq.2.16); h_c = the contact depth; h_s = the displacement of the surface at the perimeter of the contact; h_f = the final depth of the residual hardness impression, a = the contact radius [17].

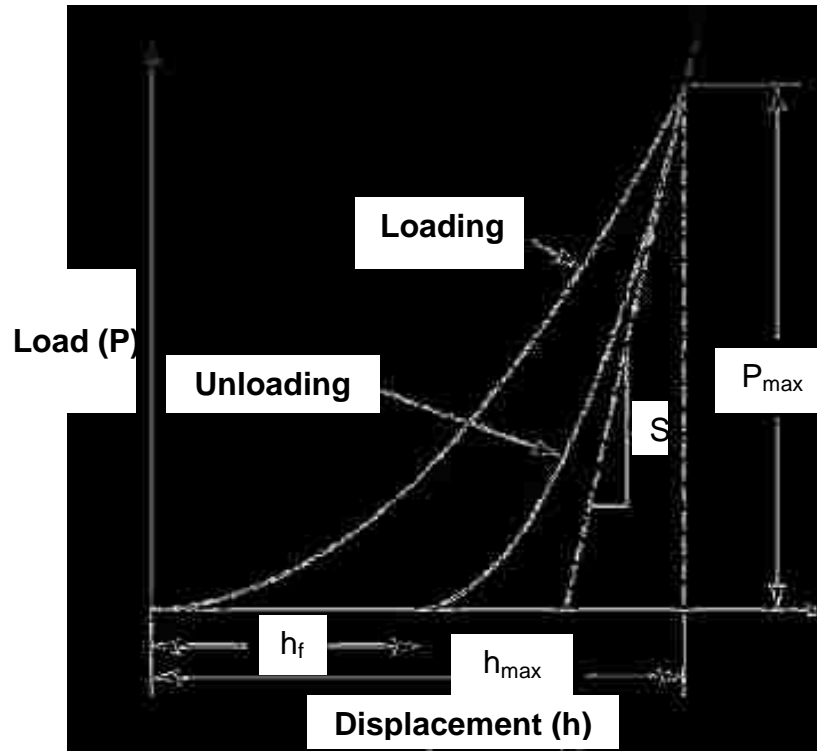


Fig.2.14: Schematic representation of load-displacement data for an indentation experiment [17].

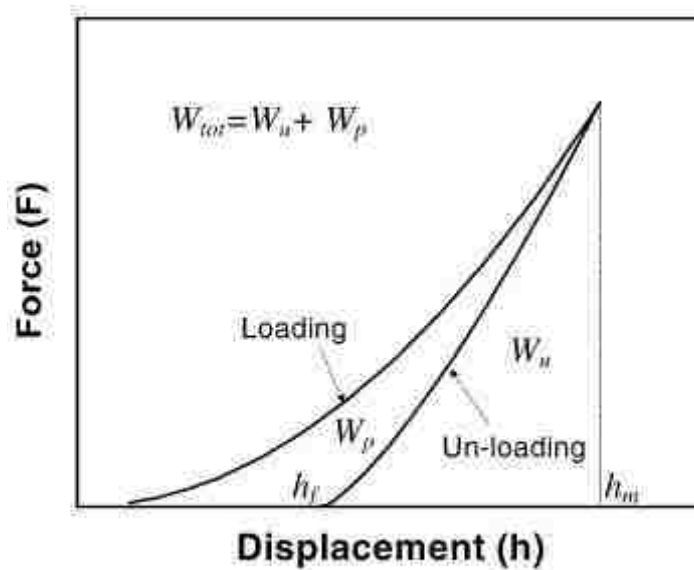


Fig.2.15: Definition of reversible work, W_u , irreversible work, W_p , and total work, W_{tot} [18].

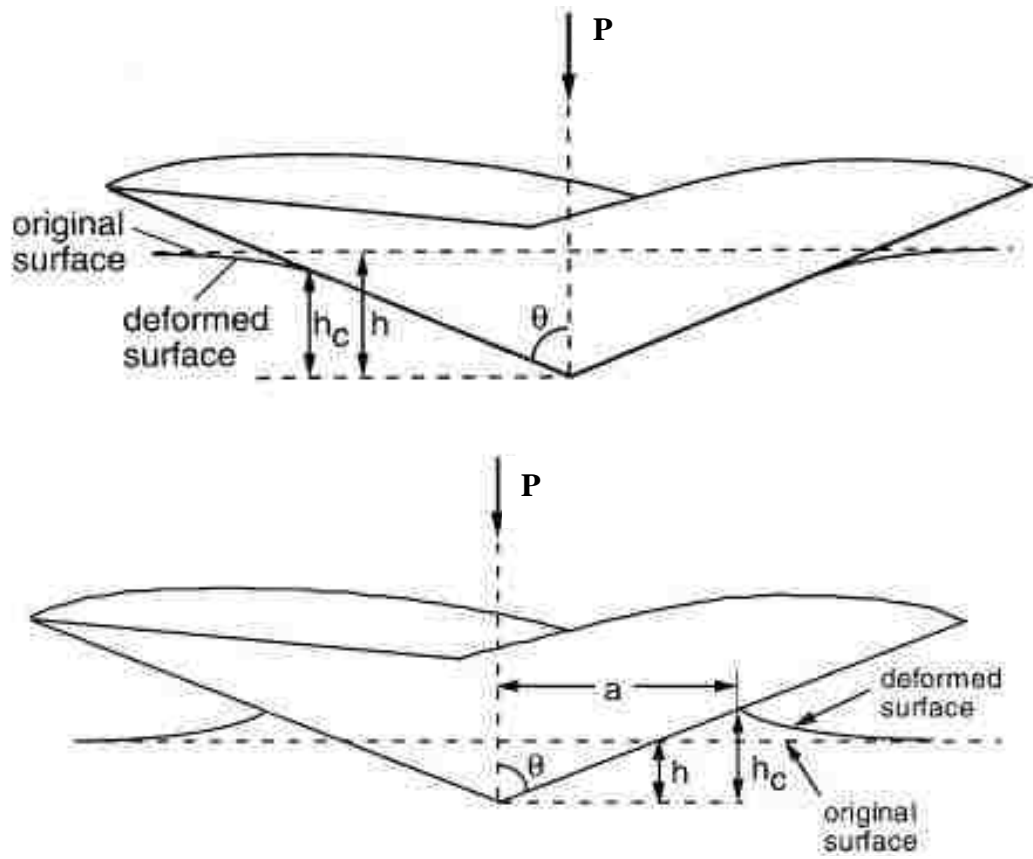


Fig.2.16: Schematic illustration of conical indentation with definition of terms [18].

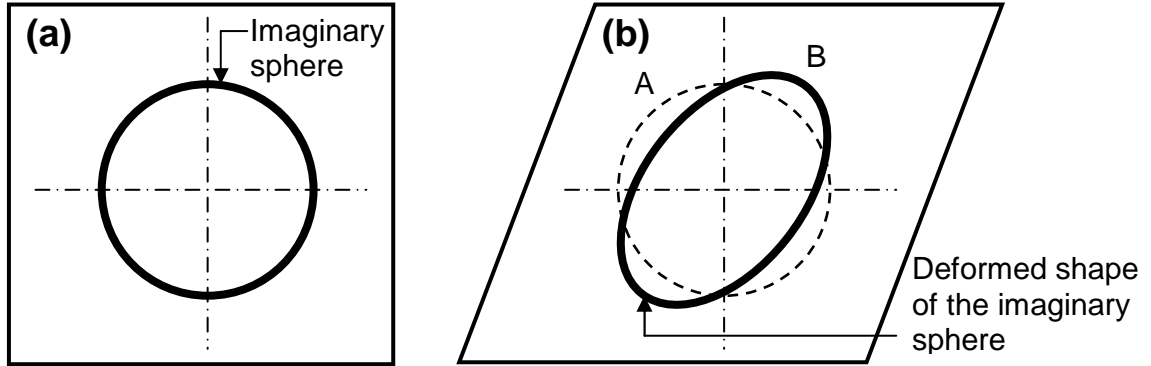


Fig.2.17: Illustration of the displacement incompatibility between the matrix and the inclusion, (a) before deformation, and, (b) after deformation of the matrix [11].

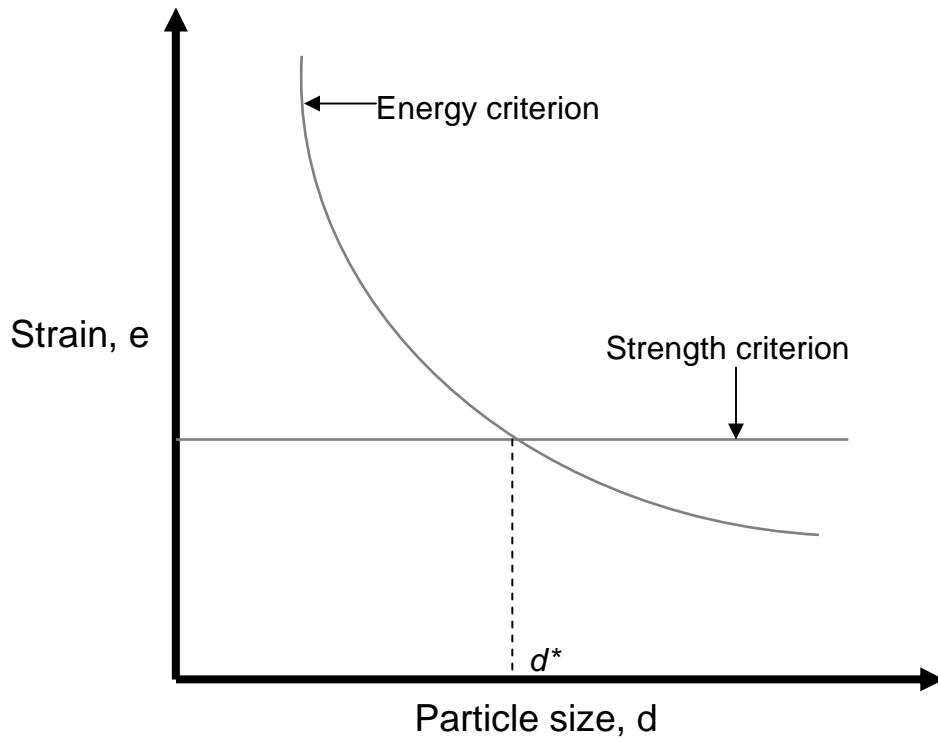


Fig.2.18: Schematics of the energy and stress criterion for void nucleation [11].

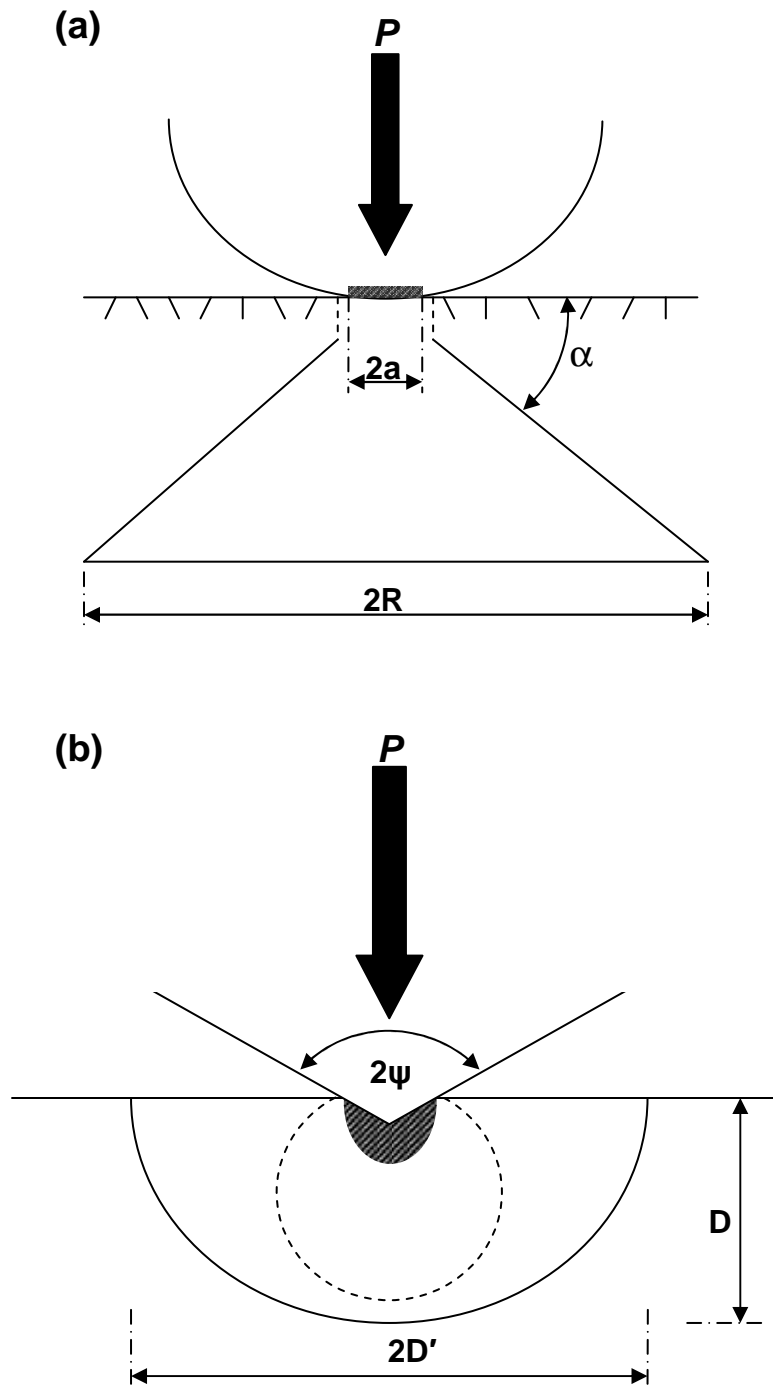


Fig.2.19: The two basic indentation fracture systems. (a) Cone crack system associated with a blunt indenter, and (b) median crack system associated with a sharp indenter [13].

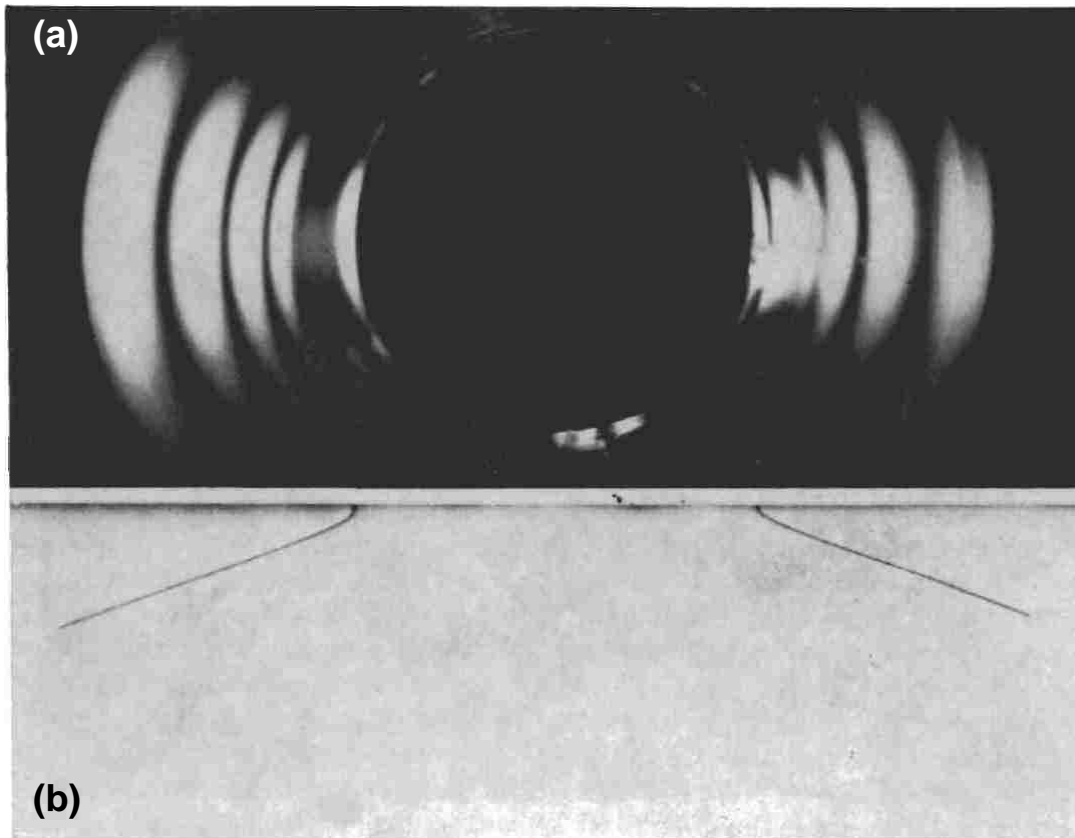


Fig.2.20: Hertzian cone crack in soda-lime glass; **(a)** view from beneath the fully-loaded specimen (light directed for specular reflection); **(b)** view in profile, after section-and-etch of unloaded specimen [96].

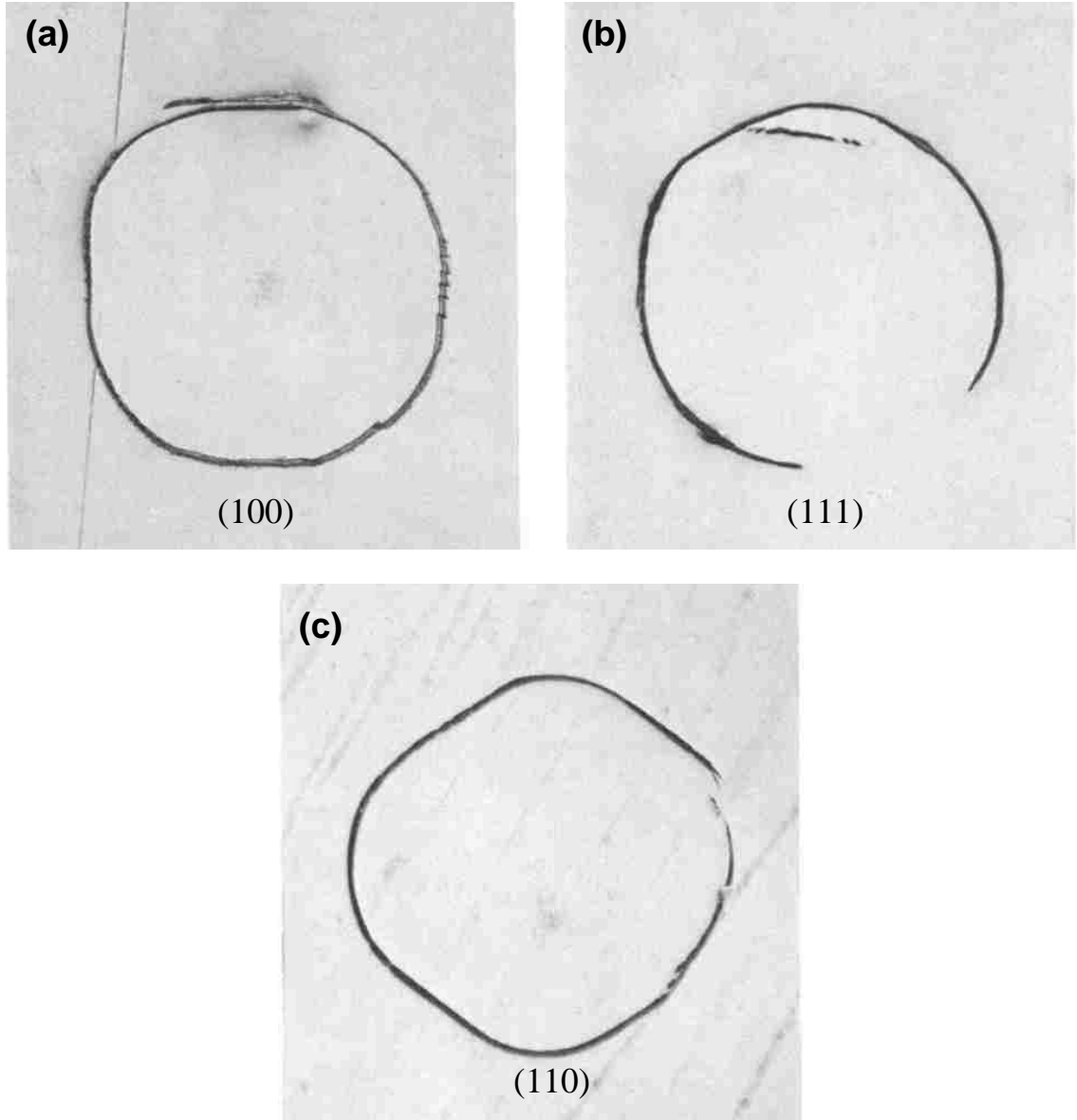


Fig.2.21: Traces of Hertzian cracks on three low-index surfaces of silicon; **(a)** 100 **(b)** 111, and **(c)** 110; Specimens were lightly abraded, indented, etched, and viewed in normal reflected light. Diameter surface cracks 1.0 mm. Some abrasion scratches are still visible. Incomplete traces are due to small deviations from perpendicularity between specimen surface and the line of application of load [19].

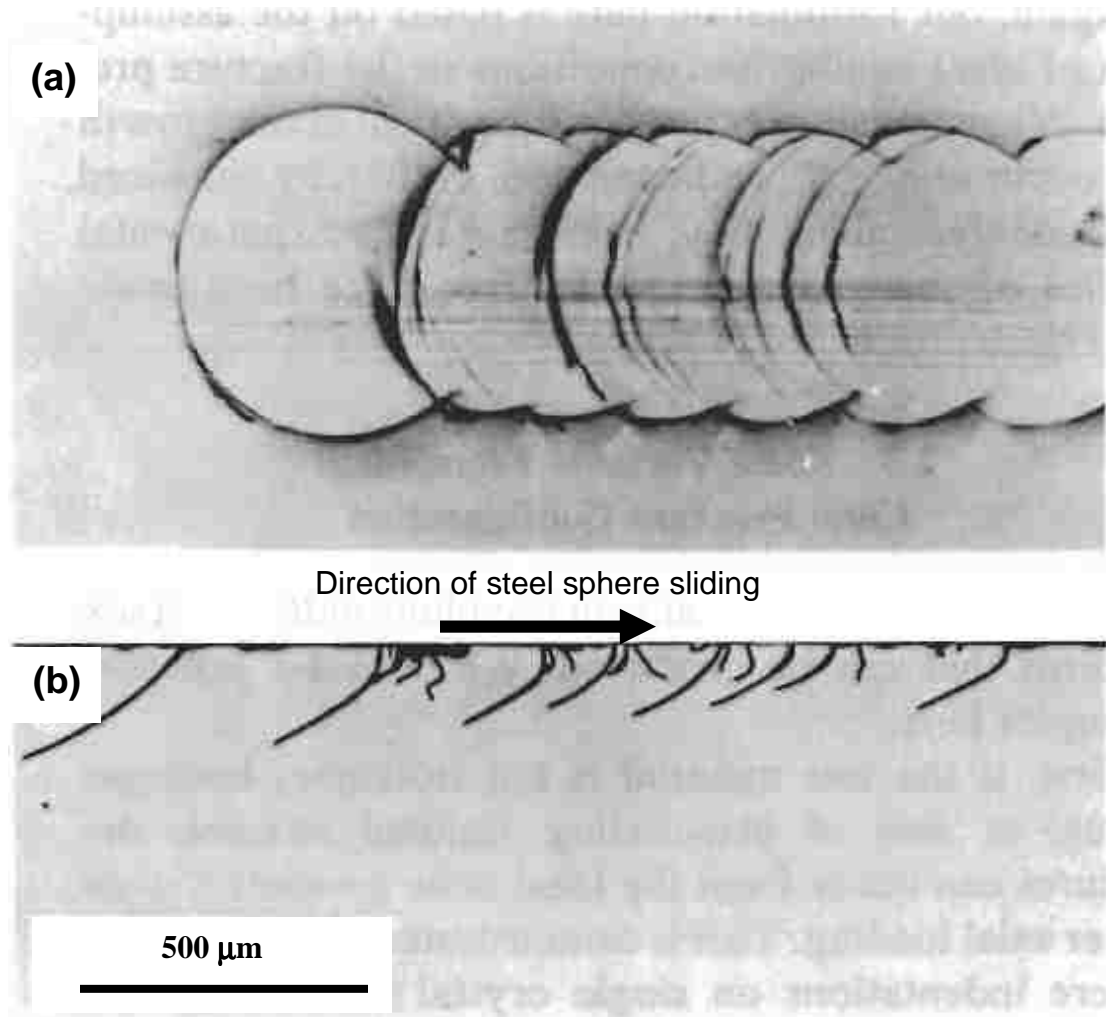


Fig.2.22: Partial cone crack damage track produced on soda-lime glass by sliding steel sphere (left to right), coefficient of friction, $\mu = 0.1$; **(a)** surface view; **(b)** profile view, after section-and-etch [9].

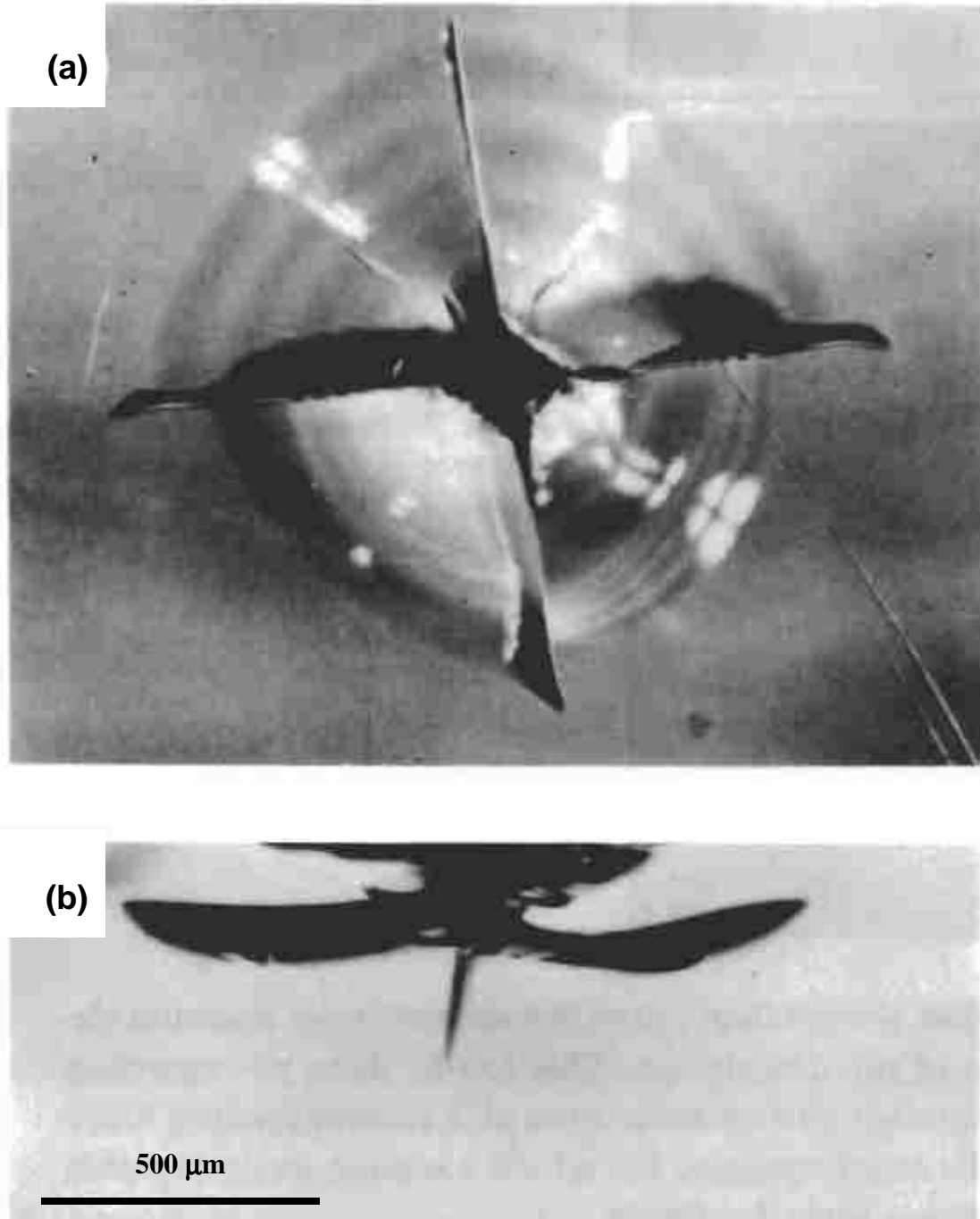


Fig.2.23: Vickers indentation in soda-lime glass: **(a)** surface view; **(b)** side view. Radial and lateral crack systems are evident [9].

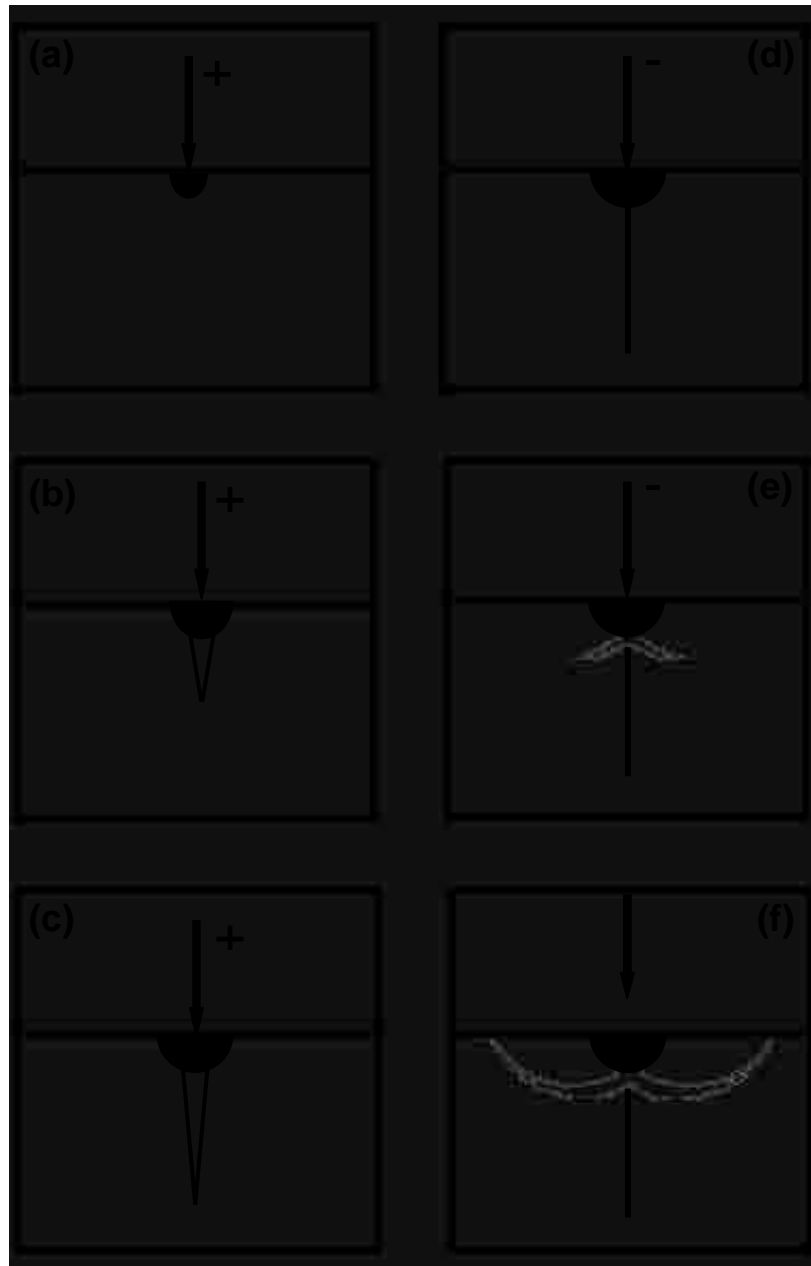


Fig.2.24: Schematic of vent crack formation under point indentation. Median vent forms during loading (+) half cycle, lateral vents during unloading (-) half-cycle. Fracture initiates from inelastic deformation zone (dark region) [14].

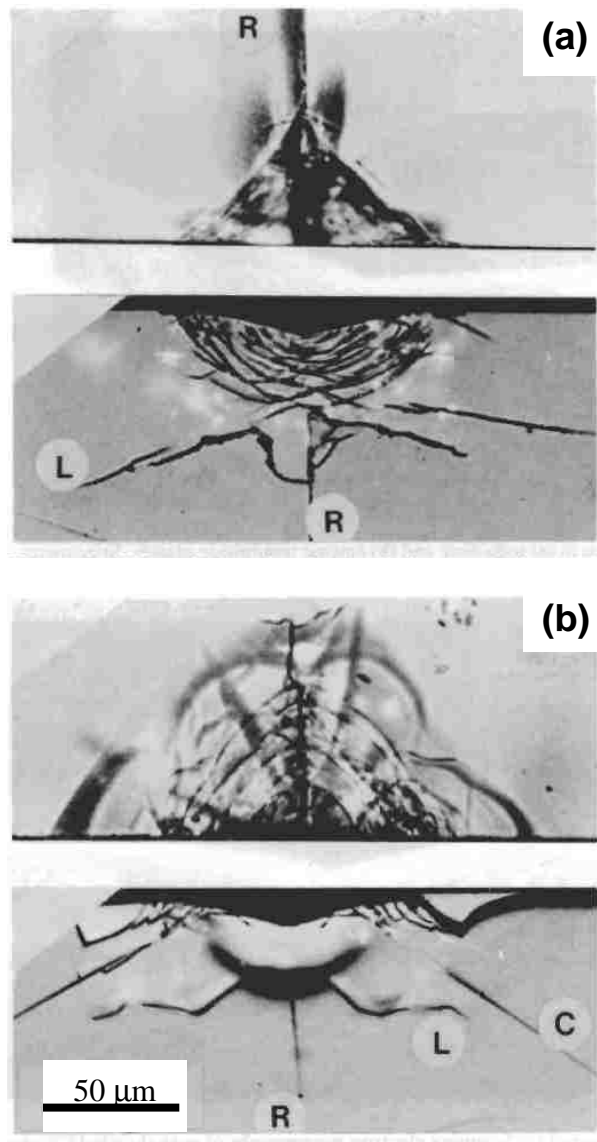


Fig.2.25: Vickers indentations in (a) soda-lime and (b) fused silica glasses in half-surface (top) and section (bottom) views. Specimens prepared by indenting across pre-existing hairline crack in glass surfaces, then breaking in order to obtain half-surface and section views. Indentation load = 30 N; width of field = 220 μm . Crack components indicated: R = radial; L = lateral; C = cone. Different deformation zone configurations are noted (near-semi-circular region immediately below impression) in the section views [20].

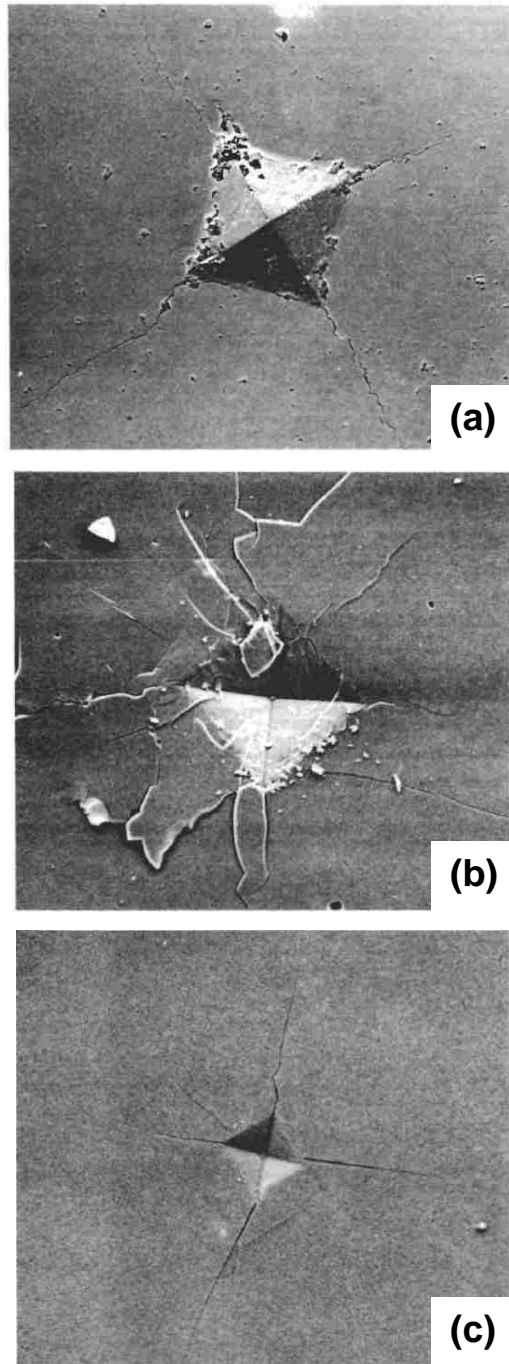


Fig.2.26: Scanning electron micrographs of Vickers indentations in three modifications of Al_2O_3 ; **(a)** grain size = 3 μm , **(b)** grain size = 20 μm , and **(c)** single crystal (sapphire) [21].

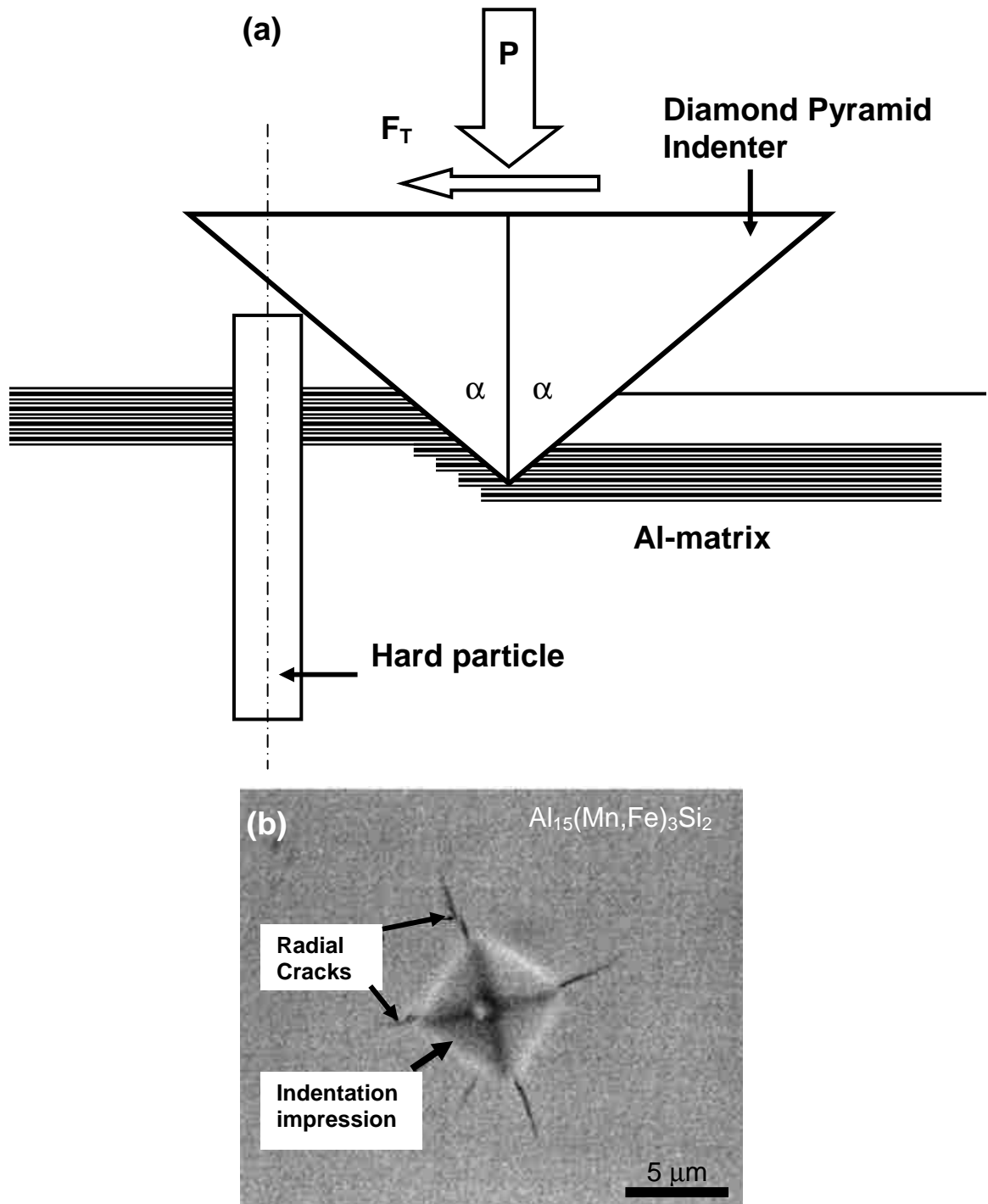


Fig.2.27: (a) A schematic diagram illustrating the cross-sectional view of the contact between Vickers indenter and the particle. The pyramid indenter has a tip angle 2α . [24]. (b) A Vickers indentation on $Al_{15}(Mn,Fe)_3Si_2$ particle surface. Median cracks can be seen at each of the four corners of the indentation impression. The average crack length $2c$ was used to calculate the fracture toughness of the particle, K_{IC} . Load = 25 g [24].

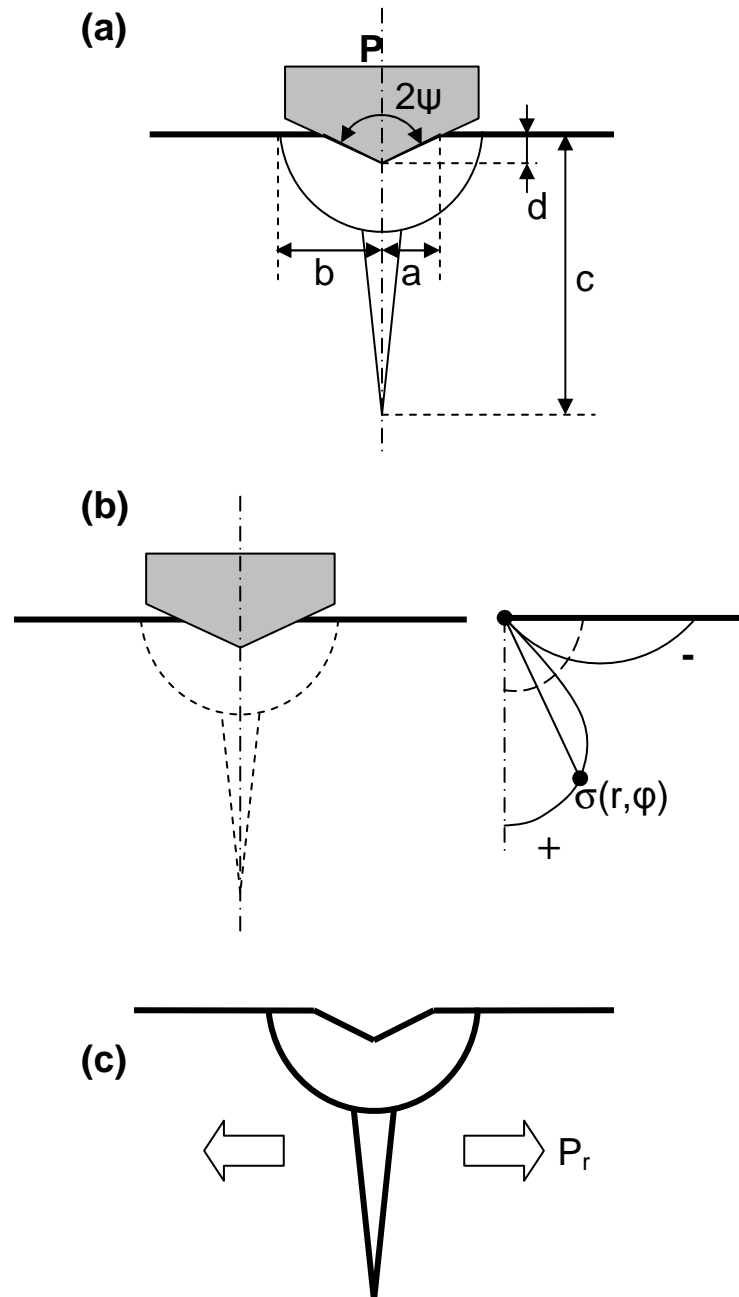


Fig.2.28: Median/radial crack system, associated with a sharp indentation, showing (a) elastic/plastic configuration at full load subdivided into (b) elastic component at full load plus (c) residual component at complete unload [25].

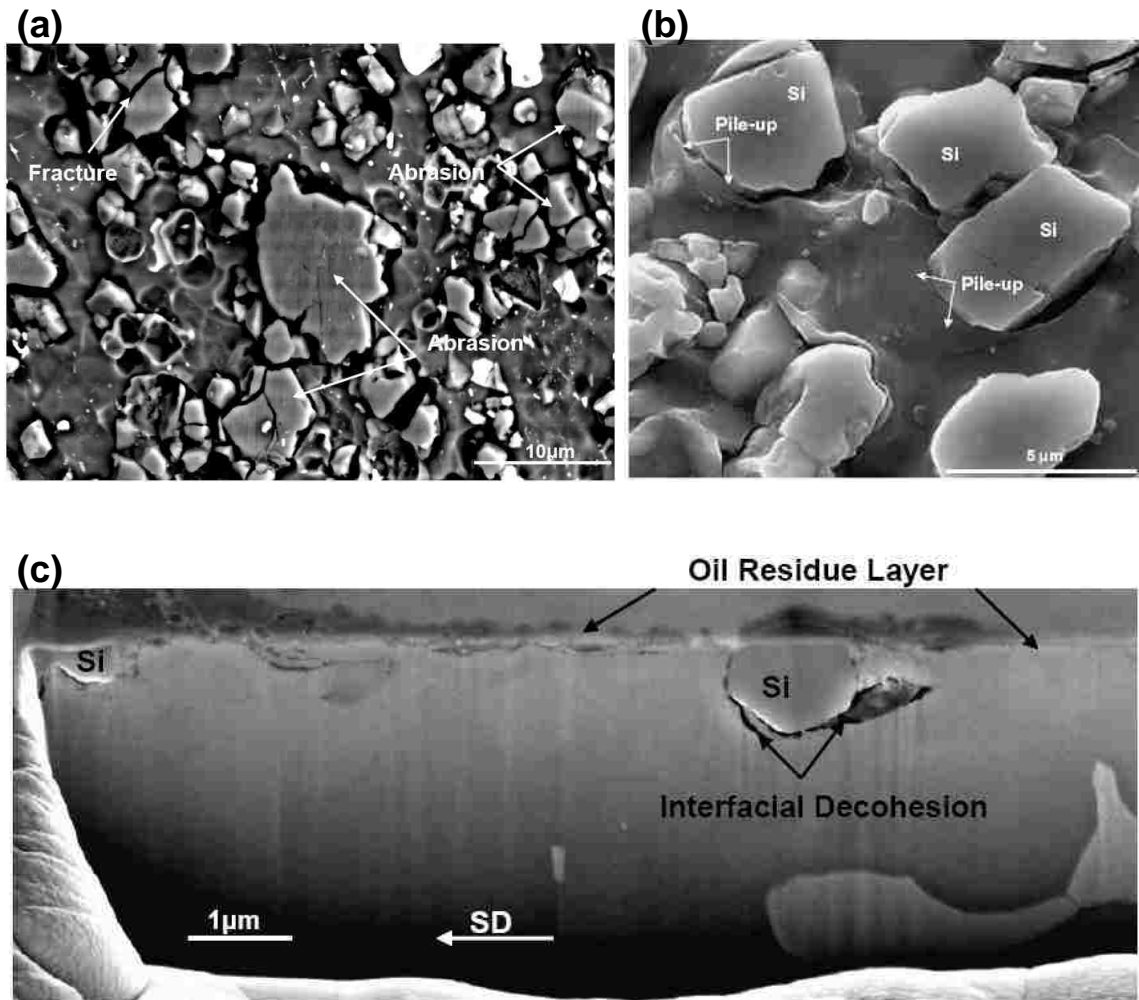


Fig.2.29: (a) A backscattered SEM image of a worn surface showing fracture and abrasive wear of silicon particles at 0.5 N after 6×10^5 sliding cycles, and (b) a high magnification secondary SEM image (20° tilt) of a worn surface showing Al pile-up on silicon particles at 1.0 N after 5×10^4 sliding cycles of a Al-25wt.%Si alloy. (c) A cross sectional SEM image of the wear track of Al-25wt.%Si showing the oil-residue layer on the contact surface with damage to silicon and Al-Si interface indicated [29].

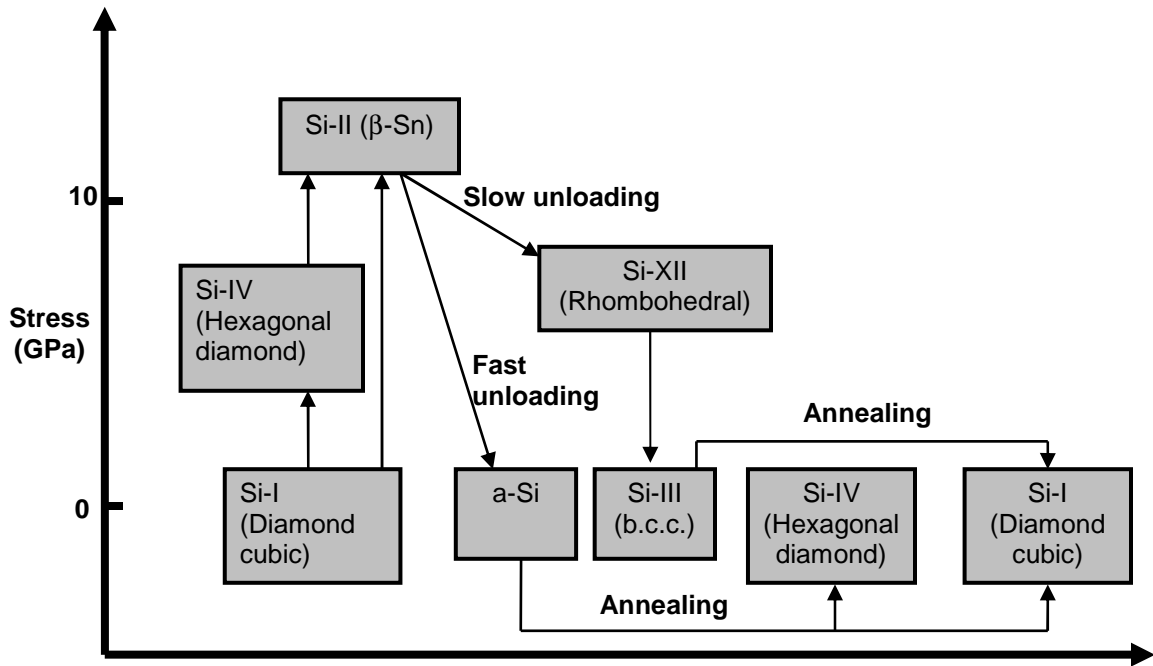


Fig.2.30: Schematic diagram of phase transformation that occur during hardness indentations and post-treatment in silicon [53]. During the loading stage of the indentation, silicon transforms from original diamond cubic Si-I structure to the hexagonal diamond Si-IV or the metallic β -Sn phase Si-II depending on local stress conditions. Upon unloading, due to pressure release, other polymorphic phases of silicon (Si-III and Si-XII) or an amorphous silicon forms depending on the unloading rate of the indenter. During annealing, there is a transition to Si-IV or, at higher temperatures, to Si-I.

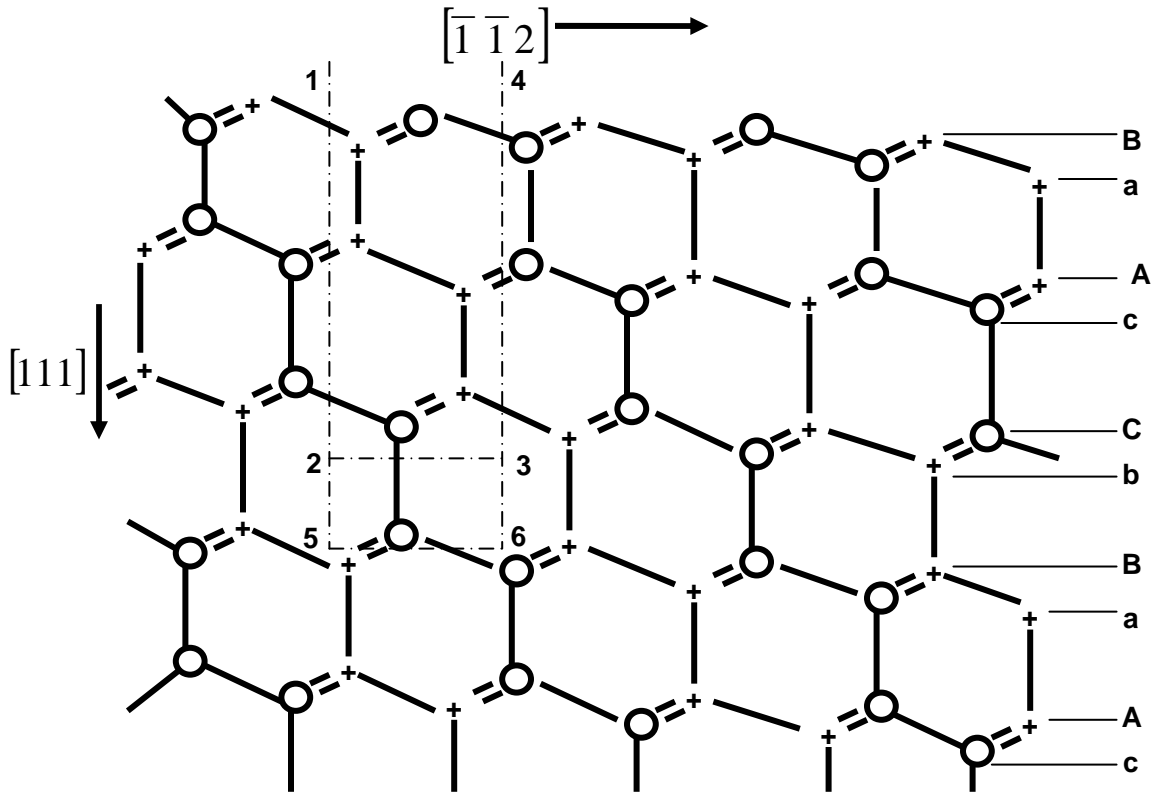


Fig.2.31: DC lattice projected onto $(1\bar{1}0)$ plane. Circles represent atoms in the plane of paper and crosses represent atoms in the plane below [61].

CHAPTER 3: Experimental

3.1. Description and Preparation of Samples

3.1.1. Al-18.5wt.%Si Alloy

A sand-cast hypereutectic Al-Si alloy (A390) with the following composition (in wt.%): 18.5% Si, 4% Cu, 0.23% Fe, 0.57% Mg, 0.07% Mn, 0.02% Ni, 0.05% Ti, 0.1% Zn and the balance Al, was studied. The microstructure of the alloy, shown in **Fig. 3.1**, presents the distribution of the different second phases, namely silicon, a Cu-containing phase θ -Al₂Cu, and a Fe-rich Al₁₅(Fe,Mn)₃Si₂ phase, in the Al-matrix. The average surface roughness of the silicon was 37.8 ± 3.3 nm, according to optical surface profilometer (WYKO NT1100) data taken over a cumulative area of $(44 \times 44) \mu\text{m}^2$ measured using an average of 10 silicon particles. The mean silicon particle length was $68.4 \pm 32.4 \mu\text{m}$, and the width was $35.5 \pm 15.5 \mu\text{m}$, corresponding to a particle aspect ratio of 1.9 ± 0.4 . Details of quantitative metallographic analyses are given in [27].

3.1.2. Monocrystalline Silicon Wafer

Vickers indentation tests were also carried out on a {111} monolithic silicon surface which acted as a reference for similar tests on the silicon particles in Al-18.5wt.%Si.

Both samples were prepared using standard metallographic techniques, involving grinding and polishing to a final polish of using a 0.1 μm diamond suspension.

3.2. Microhardness Experiments

Vickers indentations were performed using a CSM Instruments Micro-Combi Tester on second-phase particles in Al-18.5wt.%Si and on the {111} surface of monolithic silicon. Each indentation was performed on a separate second-phase particle in Al-18.5wt.%Si, and five tests were performed at each load. On the initial contact, a load of 25 mN was applied. **Fig. 3.2** is a low magnification SEM micrograph of a region of the alloy showing a large primary silicon particle, with polyhedral morphology, in the aluminum matrix. A 350 mN Vickers micro-indentation was done on the silicon particle showing the typical indent shape and crack patterns. **Figs. 3.3(a)** and **(b)** are SEM (8000X) and optical profilometry (50X) images of a 700 mN indentation done on a silicon particle. **Fig. 3.3(c)** is a high magnification (24,000X) image of the indentation deformed surface indicated by a red frame in **Fig. 3.3(a)**. In the load range considered, the indentation size varied between $5.0 \pm 0.4 \mu\text{m}$ at 200 mN, and $8.4 \pm 0.5 \mu\text{m}$ at 800 mN. **Figs. 3.4(a)** and **(b)** are SEM (13,000X) and optical profilometry (50X) images of a 300 mN indentation done on single crystal silicon. **Fig. 3.4(c)** is a high magnification (30,000X) image of the indentation deformed surface indicated by a red frame in **Fig. 3.4(a)**. **Fig. 3.5(a)** plots the Vickers microhardness values of silicon particles (measured using Oliver and Pharr method [17]) against indentation loads within a load range of 200 mN and 800 mN. Higher hardness values at lower loads are consistent with a large amount of elastic recovery [97] in the silicon particles indicating indentation-size effect phenomenon. **Fig. 3.5(b)** is an optical microstructure showing the distribution of eutectic and primary silicon particles in the aluminum matrix. A particular silicon particle in this figure was indented by a 400 mN load. A SEM image of a fractured silicon particle (by a

750 mN load) has been shown in **Fig. 3.5(c)**. They illustrate the differences in the nature of the deformation experienced by the silicon particles with increasing loads. Under a 400 mN load, the indenter led to pile up formation, whereas at 750 mN, subsurface crack propagation caused chipping out of portions of silicon adjacent to the indenter, as will be described in detail in Section 4.1.

The morphologies of residual Vickers microindentations were observed using a FEI Quanta 200 FEG Environmental Scanning Electron Microscope (ESEM) and an optical surface profilometer WYKO NT-1100 that utilizes white-light interferometry.

3.3. Calculation of Indentation Fracture Toughness: Measurements using the Crack-length Method

The indentation fracture toughness (K_{IC}) of silicon particles and the $\text{Al}_{15}(\text{Fe,Mn})_3\text{Si}_2$ phase in Al-18.5wt.%Si was determined from crack length values measured under indentation loads (L) of 300 mN and 100 mN, respectively, using the equations listed in **Table 3.1**. Accordingly, for the silicon particles, the calculated values varied within a range of 0.97 and 1.6 $\text{MPa}\cdot\text{m}^{0.5}$ [**Fig. 3.6(a)**], consistent with what has been reported as the fracture toughness of polycrystalline silicon [98]. For $\text{Al}_{15}(\text{Fe,Mn})_3\text{Si}_2$, the value was found to vary between 0.74 and 1.01 $\text{MPa}\cdot\text{m}^{0.5}$ [**Fig. 3.6(b)**]. The K_{IC} of silicon single crystal was also determined and found to vary between 0.66 and 1.345 $\text{MPa}\cdot\text{m}^{0.5}$; the obtained values were compared with those of the alloyed silicon particles and discussed later (Section 5.1.2).

Table 3.1: Calculation of the indentation fracture toughness (K_{IC}) of silicon particles using models [22] involving E = elastic modulus, H_v = Vickers hardness value, L = test load, $2a$ = the indentation mark diagonal, and $l = (c-a)$, where c is total crack length from centre of the residual indent as shown in **Fig. 4.8(a)**.

Eq.	Indentation fracture toughness (K_{IC}) equations	K_{IC} , MPa.m ^{0.5}	
		Si	Al ₁₅ (Fe,Mn) ₃ Si ₂
3.1	$K_{IC} = 0.0089 \left(\frac{E}{H_v} \right)^{\frac{2}{5}} \cdot \frac{L}{a.l^{\frac{1}{2}}}$ (1)	0.97 ± 0.14	0.74 ± 0.05
3.2	$K_{IC} = 0.0122 \left(\frac{E}{H_v} \right)^{\frac{2}{5}} \cdot \frac{L}{a.l^{\frac{1}{2}}}$ (2)	1.3 ± 0.19	1.0 ± 0.07
3.3	$K_{IC} = 0.0319 \frac{L}{a.l^{\frac{1}{2}}}$ (3)	1.6 ± 0.24	1.0 ± 0.07

3.4. Temperature-induced Phase Transformation in Silicon Particles:

Preparation of Encapsulated Al-Si Samples

Al-18.5wt.%Si samples were polished and selected silicon particles were indented using a 400 mN indentation load. Five such samples were encapsulated in evacuated and inert-gas filled glass capsules [**Fig. 3.7**] in order to prevent surface oxidation during heat treatment. Thereafter, samples were heat treated at temperatures 150°C, 190°C, 230°C, 300°C and 450°C for 2 hours and then air-cooled till the samples reached room temperature (25°C). Post-heat treatment indent sites on silicon particles were identified in each sample after breaking the glass capsules. Raman spectra were obtained from the residual micro-indent, heat treated at different temperatures, in order to observe phase transformation. Details of Raman spectroscopy parameters have been given in Section 3.5. Raman results showing phase transformation at different temperatures have been discussed in Section 4.3.2.

3.5. Raman Micro-spectroscopy

Raman spectra were collected from the deformed regions of residual indentations to investigate indentation-induced phase transformation in silicon particles. A 20 mW He-Ne laser emitting at the 632.8 nm excitation line was employed to excite the sample through the 50X objective lens of a Renishaw inVia Raman microspectrometer [Fig. 3.8]. The diameter of the laser spot on the specimen surface was 1 μm (for 50X objective lens) and the effective power of the incident laser was 2.5 mW, preventing laser-induced phase transformation in silicon to a large extent [99]. Peak identification on the obtained Raman spectra was done using WiRE 3.0 software.

3.6. Preparation of FIB-milled Cross-sectional Samples

To investigate the plastic deformation and fracture that occurred in a silicon particle's subsurface region as a result of the application of a Vickers microindenter, cross-sectional trenches were milled across the indentations using a focused ion-beam (FIB) method. The highly directional nature of the atomic bonds in covalently bonded silicon makes the ion-beam imparted atomic disordering not readily recoverable. Care was taken to avoid ion-beam damage on the surface, by depositing a thin layer of carbon across one diagonal of an indentation impression (and by paying attention that the ends of the radial cracks emanating to the surface were also covered). A trench was milled normal to the deposited carbon layer, using Ga^+ from a Ga-based liquid metal ion-source (LMIS), at an accelerating voltage of 30 kV, with beam currents ranging from 13 nA to 700 pA. Final milling was conducted at a low ion-beam current of 80 pA to minimize the

prospect of beam damage. Cross-sections were investigated using a Zeiss NVISION 40 dual beam SEM/FIB.

Cross-sectional TEM samples of the indentation were prepared using the FIB in-situ “lift-out” technique. In this case, two trenches were milled on each side of a thin silicon membrane (thickness $\sim 4 \mu\text{m}$) parallel to the deposited carbon layer. The details of TEM sample preparation are illustrated in **Figs. 3.9(a)-3.9(h)**, and consisted of the following steps:

- (a) Two trenches were ion-milled on either side of the FIB-deposited carbon layer to obtain a thin membrane (about $4 \mu\text{m}$ thick) containing the indentation and connected to the rest of the silicon particle at only two points [**Fig. 3.9(a)**].
- (b) One end of the membrane was cut free and a tungsten needle (end effector) was positioned at the top of the membrane at that end [**Fig. 3.9(b)**].
- (c) The needle was welded to the membrane using a thin layer of carbon [**Fig. 3.9(c)**].
- (d) After secure welding, the fixed end of the membrane was milled off and the TEM sample was made ready to be lifted out of the trench [**Fig. 3.9(d)**].
- (e) The TEM sample was lifted out as shown in **Fig. 3.9(e)**.
- (f) The sample was then carried to a copper grid [**Fig. 3.9(f)**].
- (g) The sample was welded to the grid, and the needle was separated. The entire silicon particle containing the indentation (along with its associated cracks) is clearly visible in **Fig. 3.9(g)**.
- (h) The top portion of the sample (containing the indentation subsurface defect structure) was polished down to 100nm thickness using a low current ion-beam of 80 pA [**Fig. 3.9(h)**].

A JEOL 2010F TEM with an imaging filter (Gatan Tridiem model) and a Philips CM12 conventional TEM were used to observe cross-sectional TEM samples at an operating voltage of 200 kV.

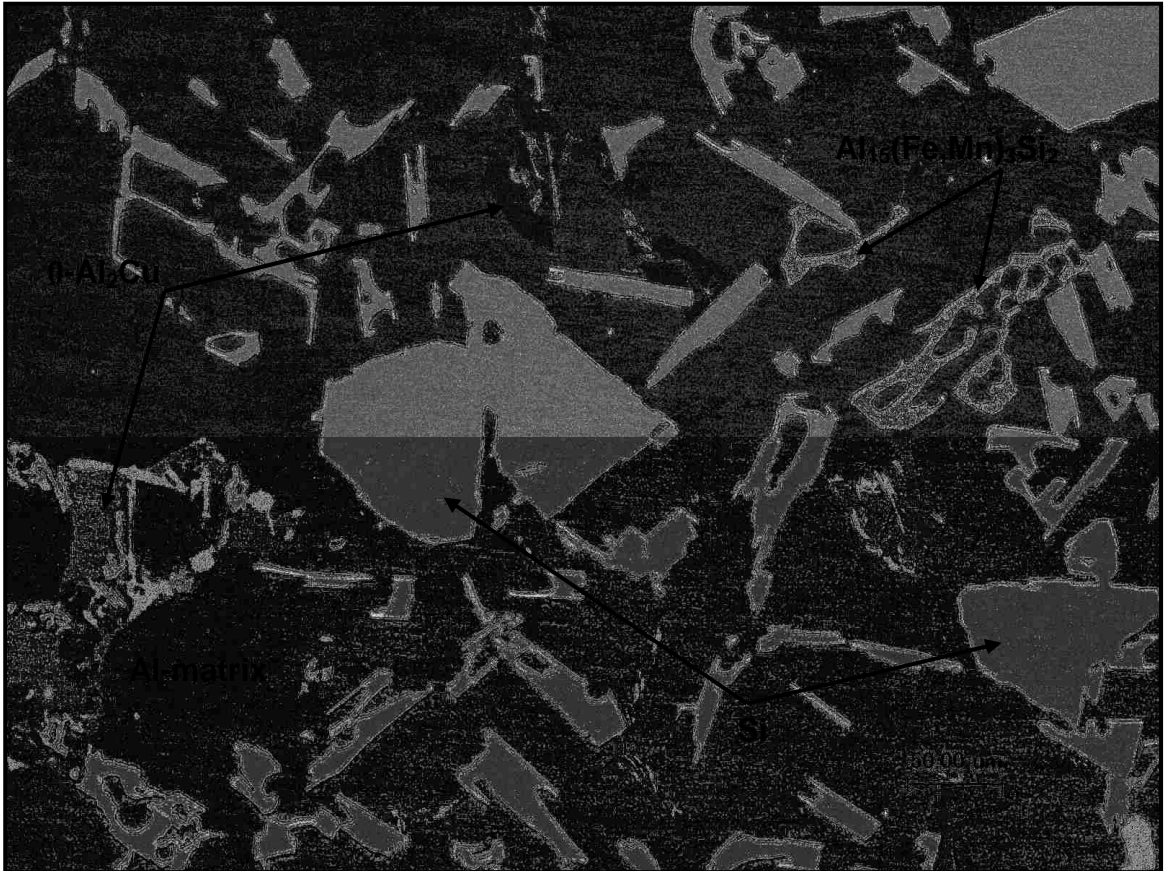


Fig.3.1: An optical microstructure of Al-18.5wt.%Si showing the different second phases. The silicon particles appear as dark brown with varying aspect ratios. The $\text{Al}_{15}(\text{Fe,Mn})_3\text{Si}_2$ has a script-type morphology. The $\theta\text{-Al}_2\text{Cu}$ has the lightest contrast, appearing as small patches.

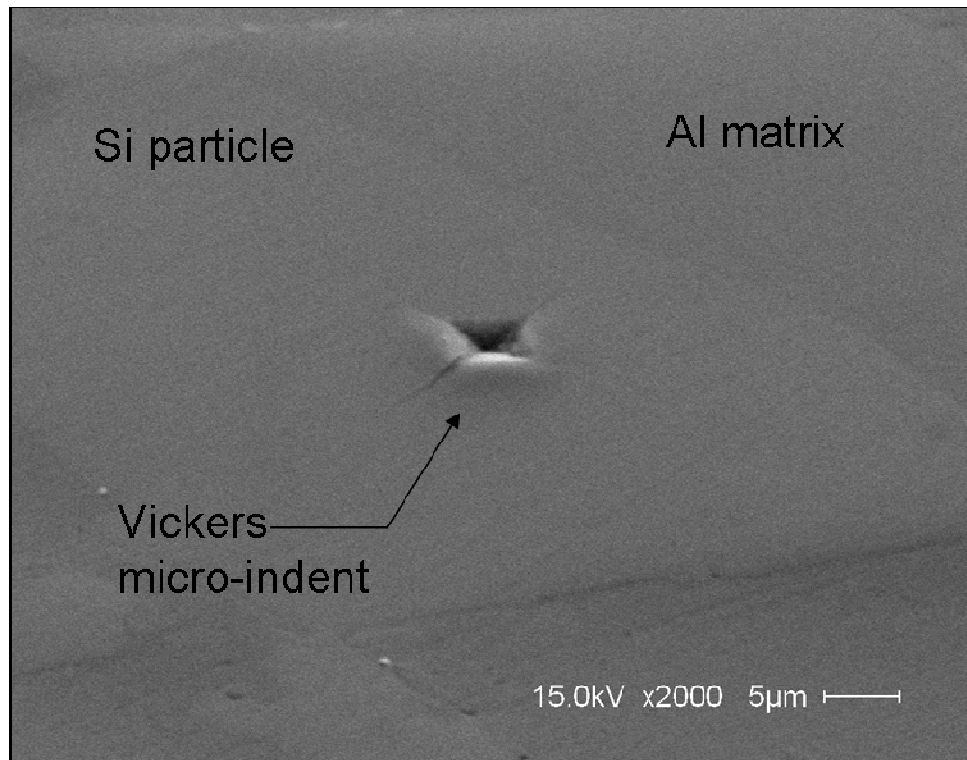


Fig.3.2: A SEM micrograph of a region in Al-18.5wt.%Si showing a large polyhedral silicon particle. A Vickers micro-indentation test has been performed on the silicon particle under a load of 350 mN.

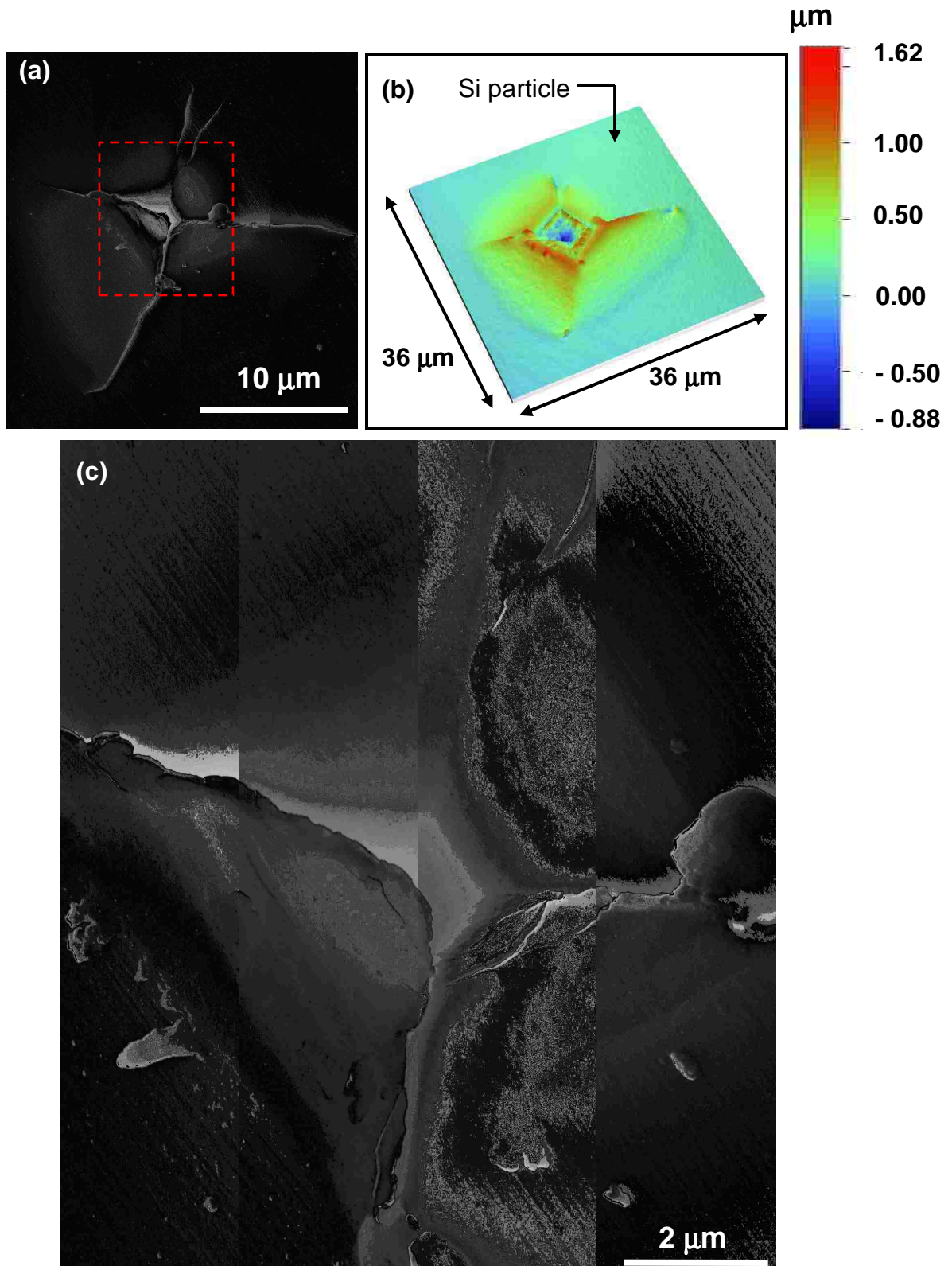


Fig.3.3: (a) SEM image of a 700 mN indentation on a silicon particle; (b) Optical profilometry image of the same indentation in (a); (c) High magnification (24,000X) SEM image of the deformed surface indicated in (a) by a red frame.

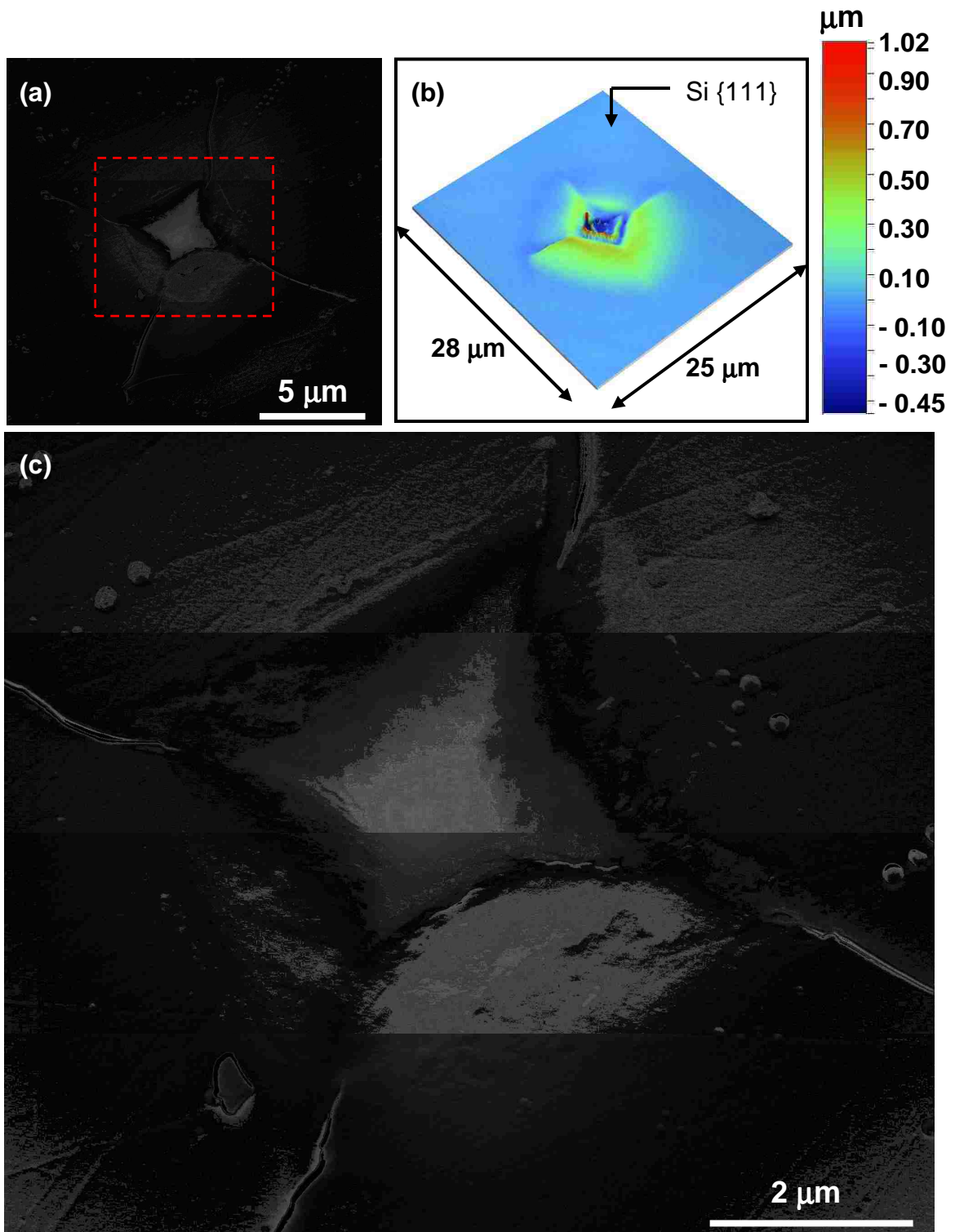


Fig.3.4: (a) SEM image of a 300 mN indentation on a monolithic silicon {111}; (b) Optical profilometry image of the same indentation in (a); (c) High magnification (30,000X) SEM image of the deformed surface indicated in (a) by a red frame.

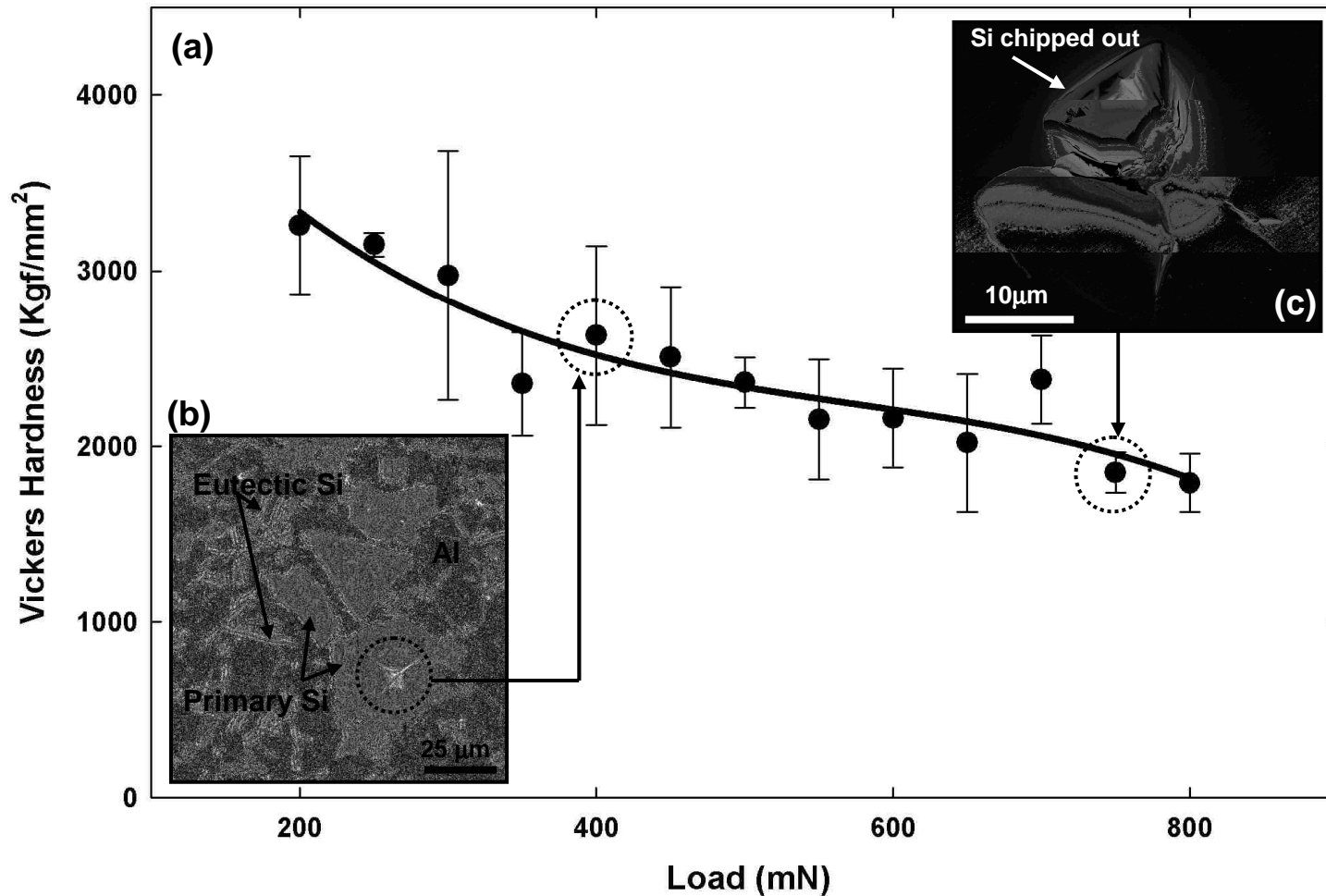


Fig.3.5: Vickers hardness values for silicon in Al-18.5wt.%Si, plotted as a function of the indentation load, which is emphasized by a regression trend line. Indentation size effect (ISE) is observed from the hardness values at very low and high loads. **(b)** Optical microstructure showing a general view of the alloy; a 400 mN Vickers indent has been done on a silicon particle. **(c)** SEM image of a 750 mN indentation showing chipping-out fracture of silicon.

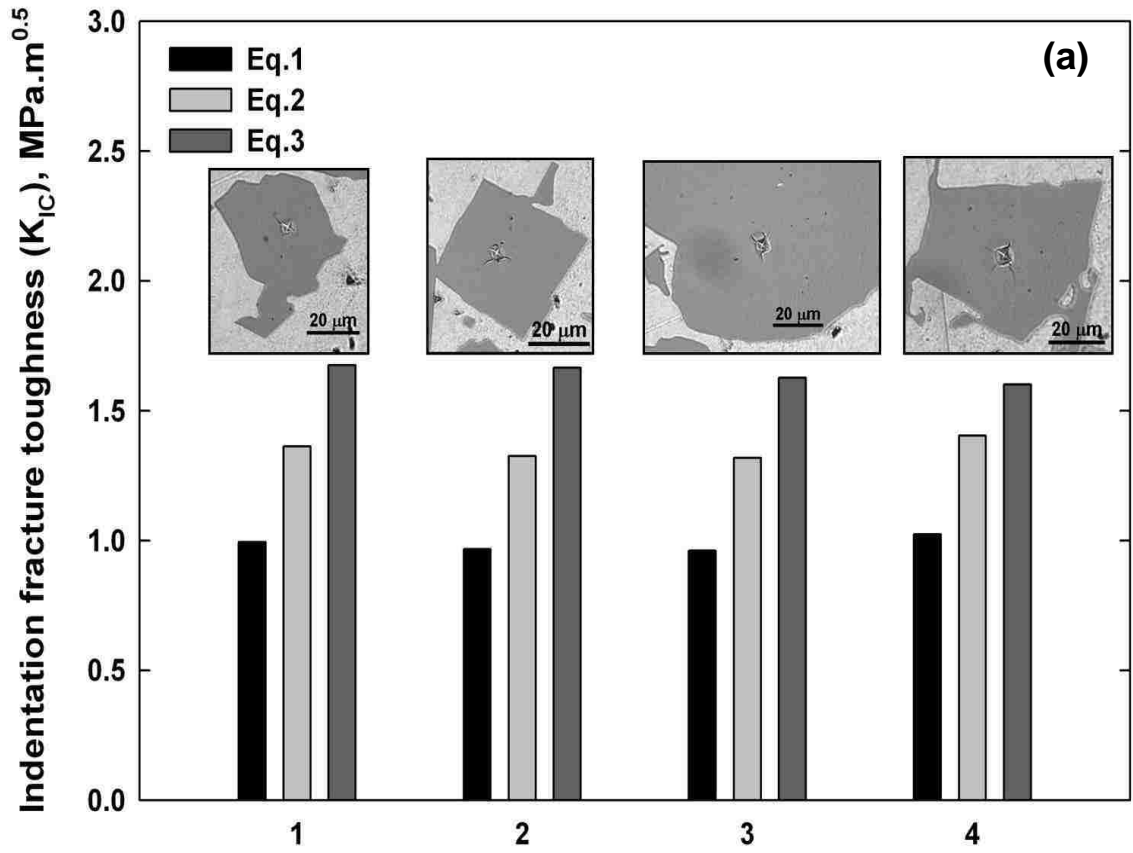


Fig.3.6: Indentation fracture toughness (K_{IC}) measured using the crack length method of the (a) silicon particles and (b) $\text{Al}_{15}(\text{Fe},\text{Mn})_3\text{Si}_2$ phases shown in the inset.

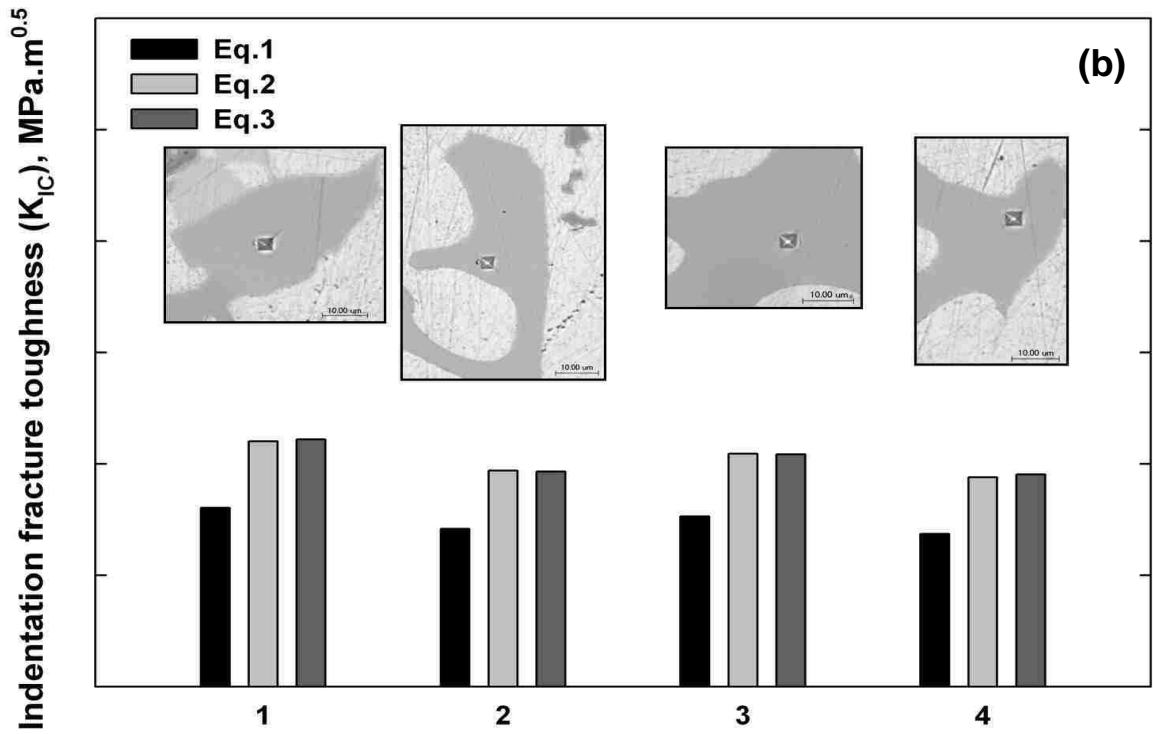


Fig.3.6: Contd.

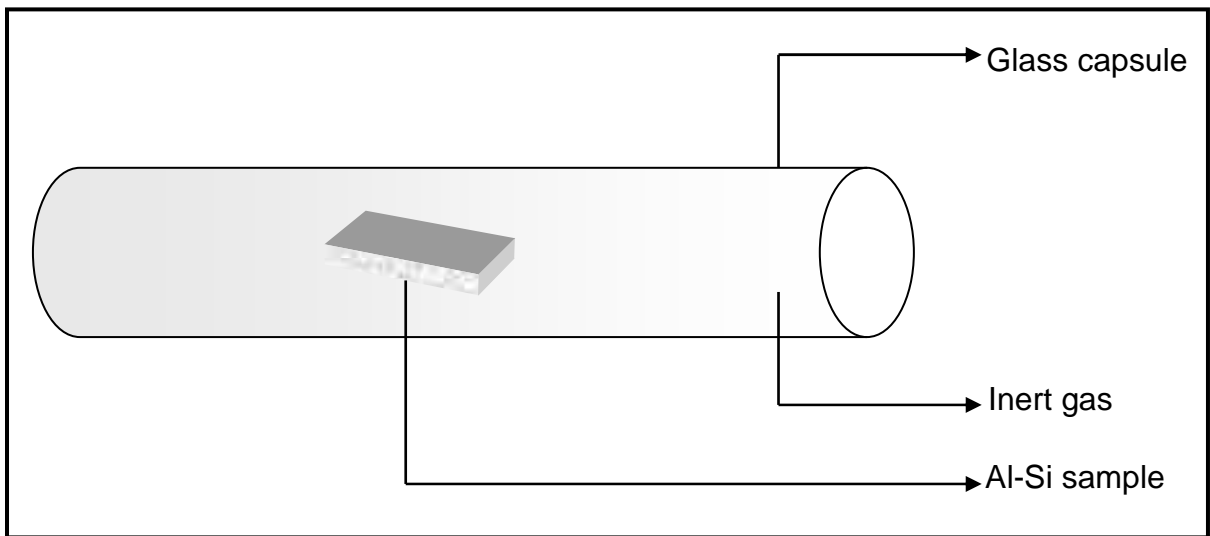


Fig.3.7: Diagram showing an encapsulated Al-Si sample prepared for heat-treatment and subsequent analysis of temperature-induced phase transformation in silicon.

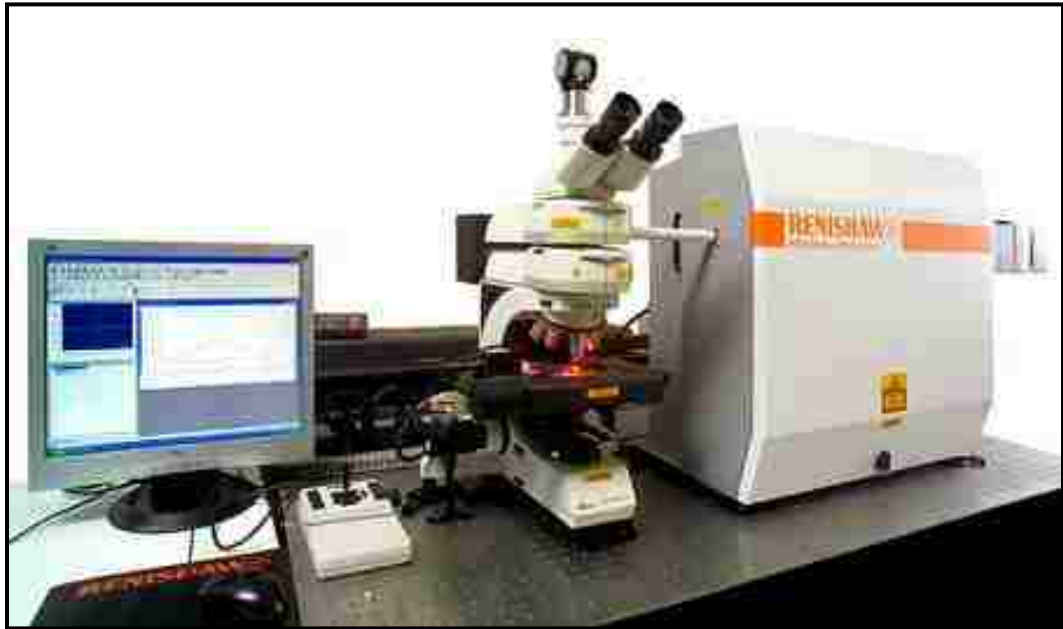


Fig.3.8: Renishaw InVia Raman Microscope.

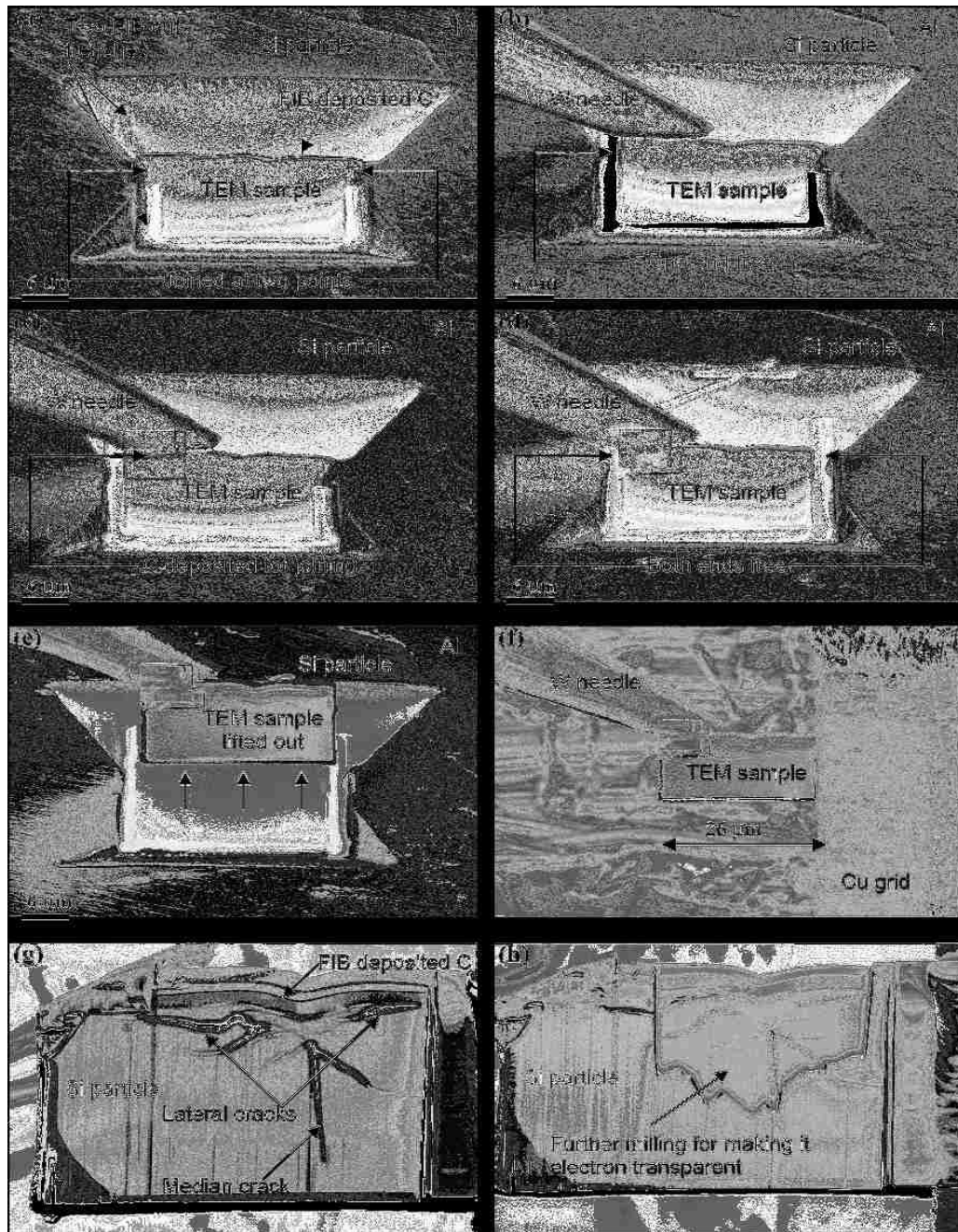


Fig.3.9: SEM images of the steps for preparing a TEM sample by FIB lift-out method, including (a) the ion milling of two trenches adjacent to the strip of carbon deposited on the membrane (TEM sample) containing the indentation, at which the membrane is connected at two points only; (b) a W needle is brought to the top of the membrane after another end is made free; (c) the needle is welded with the membrane by depositing carbon; (d) the other end of the membrane is freed after proper welding; (e) lifting out the TEM sample; (f) carrying the TEM sample to a Cu grid; (g) welding the sample to the grid and separating the needle from the sample; and (h) further fine ion-milling of the indented region to make it transparent to electrons.

CHAPTER 4: Results

4.1. Indentation Surface Morphology and Phenomenological Description of Silicon Particle Fracture

4.1.1. Pile-up Formation due to Plastic Deformation and Lateral Crack Formation

Fig. 4.1(a) shows indentation load vs. penetration depth curves obtained at four typical loads of 400 mN, 600 mN, 700 mN, and 800 mN. The loading curves, in all cases, follow the same path. An elbow or “pop-out” was observed in the unloading curve for the 600 mN indentation in **Fig. 4.1(a)**. Slightly increased tendency of work hardening behaviour in silicon particles with load was indicated by the decreasing nature of the experimental h_f/h_m ratios with load (h_f = the penetration depth at complete unloading and, h_m = the maximum penetration depth) in **Fig. 4.2**. **Fig. 4.3** shows the influence of the indentation load on the measured elastic moduli (E). This change in the values can be explained by the change of the initial portion of the slope, S , of the unloading curve, as,

$$E = \frac{S}{2} \frac{\sqrt{\pi}}{\sqrt{26.43h_c}} \quad (4.1)$$

where, h_c = the contact depth. **Fig. 4.4** shows a plot of the plasticity involved in the silicon particles expressed as a function of the indentation load. The plasticity is a ratio equal to the value of the plastic work done divided by the sum of the plastic work (loading curve) and the elastic work (unloading curve) during each indentation experiment. The results indicate that this ratio decreases slightly with load, like the h_f/h_m ratios and the elastic moduli, and thus the work of indentation is also load dependent. Thus, **Figs. 4.2 - 4.4** along with **Fig. 3.5** indicate that microhardness measurements on

second phase silicon particles is accompanied by the indentation size-effect phenomenon, where the material properties are found to vary as a function of the indentation load. Finally, the plot shown in **Fig. 4.5** was constructed to demonstrate that though the elastic moduli and the hardness results were found to be load dependent, the E/H_V ratios (where, H_V is the Vickers hardness no.) in turn, obtained from the same indentation experiments, were load independent.

Figs. 4.1(b)-4.1(e) show 3-dimensional surface profilometry images of the indentations. The amount of pile-up of material due to plastic deformation increased with the load, from 400 mN [**Fig. 4.1(a)**] to 800 mN [**Fig. 4.1(e)**]. At loads higher than 600 mN, fully-formed radial cracks contributed to the increasing pile-up height and diameter [**Fig. 4.1(c)**]. It was noted that at high loads, subsurface lateral crack formation [indicated by a faint halo in **Fig. 4.1(d)**] prompted silicon volume expansion, and thus was an additional factor that enhanced pile-up.

In order to provide a quantitative analysis of change in surface morphologies as a result of indentation, a series of 2-dimensional profiles of the indentation impressions and pile-ups were plotted, starting from the centre of the indentation along a horizontal line crossing the material pile-up formations [**Fig. 4.6(a)**]. At loads less than 600 mN, pile-up radii reached a maximum of 6 μm , whereas pile-up radii at 700 and 800 mN extended to 16 μm . **Fig. 4.6(b)** shows the maximum height of pile-up adjacent to the silicon indentations, in addition to the indentation penetration depths plotted as a function of the indentation load. The depth of penetration into the silicon was found to vary linearly with load. At loads higher than 650 mN, the increase in pile-up height was evident from the

greater slope, indicative of the fact that volume expansion due to subsurface lateral crack formation had become operative, in addition to silicon plastic deformation.

4.1.2. Statistical Nature of Indentation Fracture

A statistical analysis of the frequency of subsurface lateral cracks that reached the surface of silicon particles was conducted using optical profilometry and SEM images of indentations. The resulting plot in **Fig. 4.7(a)** depicts the probability of lateral cracks reaching the surface as a function of the indentation load. Each of these observations is based on the results of six indentation tests on different silicon particles at a particular load. The frequency of subsurface cracks that reached the surface $P_f(L)$ at an indentation load, L , obeys an exponential curve defined by the following equation:

$$P_f(L) = (-5.6 \times 10^{-3}) + (1.023) \left[1 - \exp \left\{ - \left(\frac{L - 48.4}{439.1} \right)^{2.73} \right\} \right] \quad (4.2)$$

According to experimental data, $P_f(L) \approx 0$ for $L < 200$ mN, whereas $P_f(L) \approx 1$ at $L \geq 650$ mN, depicting 100% probability of subsurface cracks reaching the surface and causing the “chipping-out” fracture of the silicon particle [**Fig. 3.5(c)**]. The data in **Fig. 4.7(a)** can be expressed in the form of Weibull probability curve shown in **Fig. 4.7(b)**, using survival probability values $P_s(L)$, i.e., resistance to chipping-out fracture occurrence, where $P_s(L) = 1 - P_f(L)$. As the indentations were performed on a narrowly selected silicon particle size range of 30% of the mean particle width, the particle volume effect could be ignored and thus, the basic form of Weibull analysis [43] can be adopted. As a result, the silicon particles’ fracture survival probability can be assumed dependent only on the indentation load. It followed that for $P_s(L) = \frac{1}{e} = 0.37$, $L_o = 480$ mN and thus

$$\ln \ln \left(\frac{1}{P_s} \right) = m \ln \left(\frac{L}{480} \right) \quad (4.3)$$

for which the Weibull modulus of $m = 3.5$, which reveals a highly variable nature of chipping fracture frequency of the indented particles. Using the empirically determined values of m and L_o ,

$$P_s(L) = \exp \left[- \left(\frac{L}{480} \right)^{3.5} \right] \quad (4.4)$$

which is the Weibull equation that expresses the survival probability of silicon to fracture at a given indentation load, L . The micromechanisms of fracture are investigated in Section 4.2 and discussed in detail in Chapter 5.

4.2. Subsurface Damage and Indentation Crack Patterns

Cross-sectional investigations of the indentations revealed the damaged zone and subsurface crack patterns responsible for silicon particle fracture. A plane-view SEM image of a Vickers micro-indentation after loading to 475 mN (corresponding to $P_s(L) \approx 0.37$) on a silicon particle is shown in **Fig. 4.8(a)** and indicates well-developed radial cracks emanating from each of the four corners of the indentation impression. The corresponding 3-dimensional surface profilometry image of the same indentation, revealing the existence of pile-up adjacent to the indentation impression is shown in **Fig. 4.8(b)**. The position of the FIB-milled trench is marked on **Fig. 4.8(b)**. The SEM image of the resultant ion-milled cross-section, given in **Fig. 4.8(c)**, depicts typical features of indentation induced subsurface damage. Accordingly, a semi-circular plastic core (of slightly lighter contrast) exists underneath the residual indentation impression. The radius of this plastic core was measured to be approximately 2.8 μm , a value that was later used

for calculating the equivalent pressure for an applied indentation load (Section 5.2). A well-developed median crack, of about 9 μm long, propagated perpendicular to the contact plane starting from immediately beneath the plastic core. Lateral cracks, also originating from the base of the plastic core, were also prominent, and extend on both sides in a “saucer-like” manner, almost parallel to the surface.

4.3. Micro-Raman Spectroscopy of Residual Indentation Impressions

4.3.1. Results of Room Temperature Phase Transformations in Silicon Particles

Raman spectra identified diverse metastable crystalline forms of silicon under the residual indent. **Fig. 4.9** consists of two Raman frequency shifts, one from a non-indented silicon particle and the other obtained from a silicon particle subjected to Vickers micro-indentation (at 475 mN), as shown in the inset in **Fig. 4.9**. The non-indented silicon particle is characterized by the typical strong and sharp peak at 522.4 cm^{-1} , as well as a much weaker, broader peak at 306 cm^{-1} , both due to diamond cubic Si-I. The post-indentation Si-I peak at 525.5 cm^{-1} was much less intense than the original Si-I peak at 522.4 cm^{-1} , indicating an almost complete phase transformation of Si-I to other forms of silicon. The shifts at 168.5 cm^{-1} , 377.5 cm^{-1} , 387 cm^{-1} , 399 cm^{-1} , and 438.6 cm^{-1} were due to both bcc Si-III and rhombohedral Si-XII phases, while the shifts at 186.2 cm^{-1} and 354.8 cm^{-1} corresponded to Si-XII, and the shift at 496 cm^{-1} belonged to Si-III [100].

4.3.2 Effect of Temperature on Phase Transformations in Silicon Particles

Fig. 4.10 shows the resultant Raman spectra obtained from residual micro-indentations in silicon particles in Al-18.5wt.%Si heat treated to elevated temperatures for 2 hours and subsequent air-cooling. The spectra show the gradual reversion of the metastable

crystalline phases of silicon, namely, Si-III and Si-XII, at room temperature to diamond cubic Si-I with increase of temperature. The metastable phases are well observed in the silicon indents up to a temperature of 150°C. At 190°C, the shifts due to Si-III and Si-XII between 370 and 440cm⁻¹ almost disappear (though the Si-XII shift at ~355 cm⁻¹ still remains but of much less intensity than what it was in the room temperature indent) and the intensity of the Si-I peak at ~525 cm⁻¹ starts to increase. Thus, the transformation of Si-III and Si-XII phases to Si-I initiated somewhere between temperatures 150°C and 190°C. Though, the last trace of Si-XII at ~355 cm⁻¹ disappears at 300°C. At 450°C (which is just below the temperature of change in silicon particle morphology, 480°C [2]), the other Si-I peak at the 303.6 cm⁻¹ shift becomes prominent and the ongoing phase reversion is said to be complete.

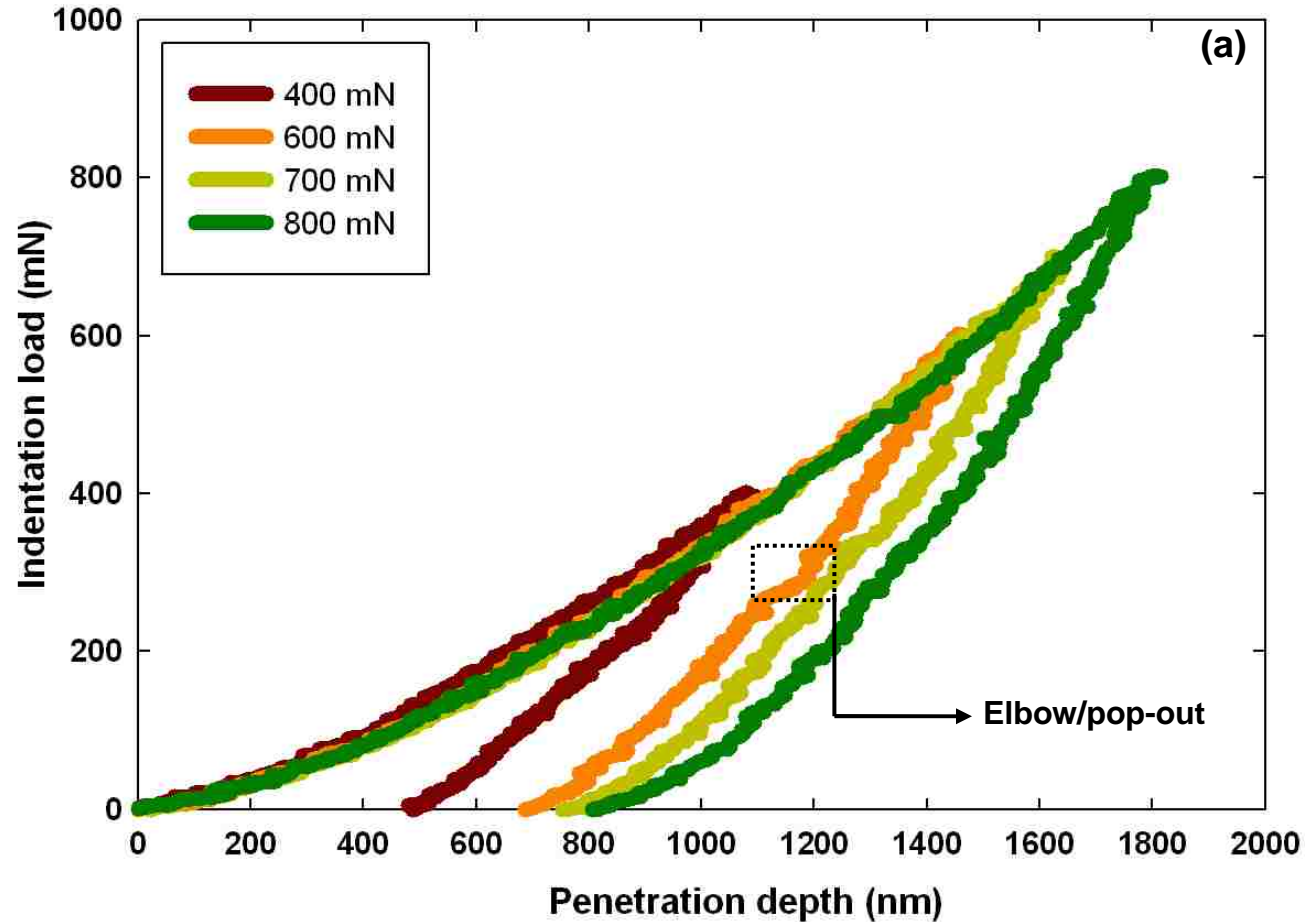


Fig.4.1: (a) Indentation load vs. penetration depth curves generated from the Vickers micro-indentation of silicon particles in Al-18.5wt.%Si. 3-dimensional surface profilometry images of (b) 400 mN, (c) 600 mN, (d) 700 mN, and (e) 800 mN Vickers micro-indentations for different silicon particles. The amount of plastic deformation and crack formation in the silicon particles increased with the indentation load.

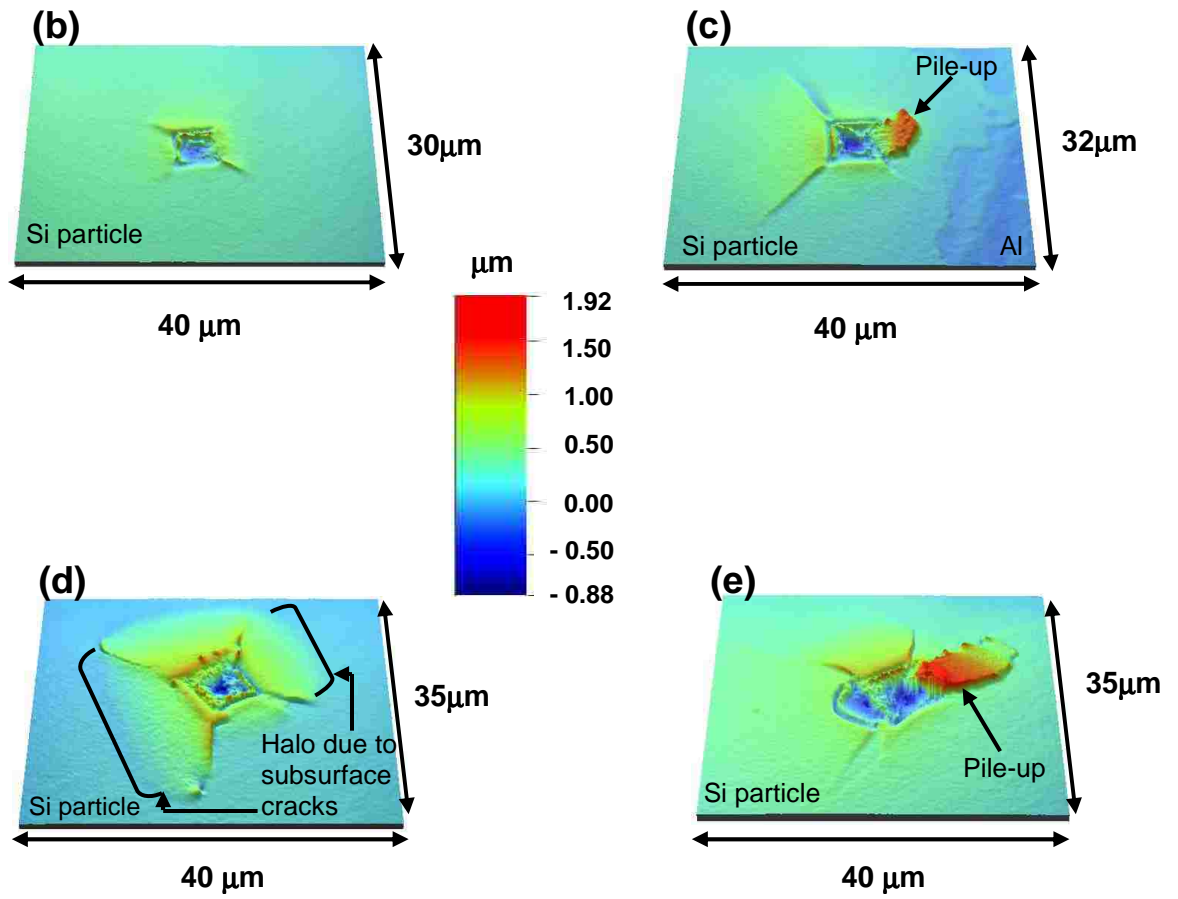


Fig.4.1: Contd.

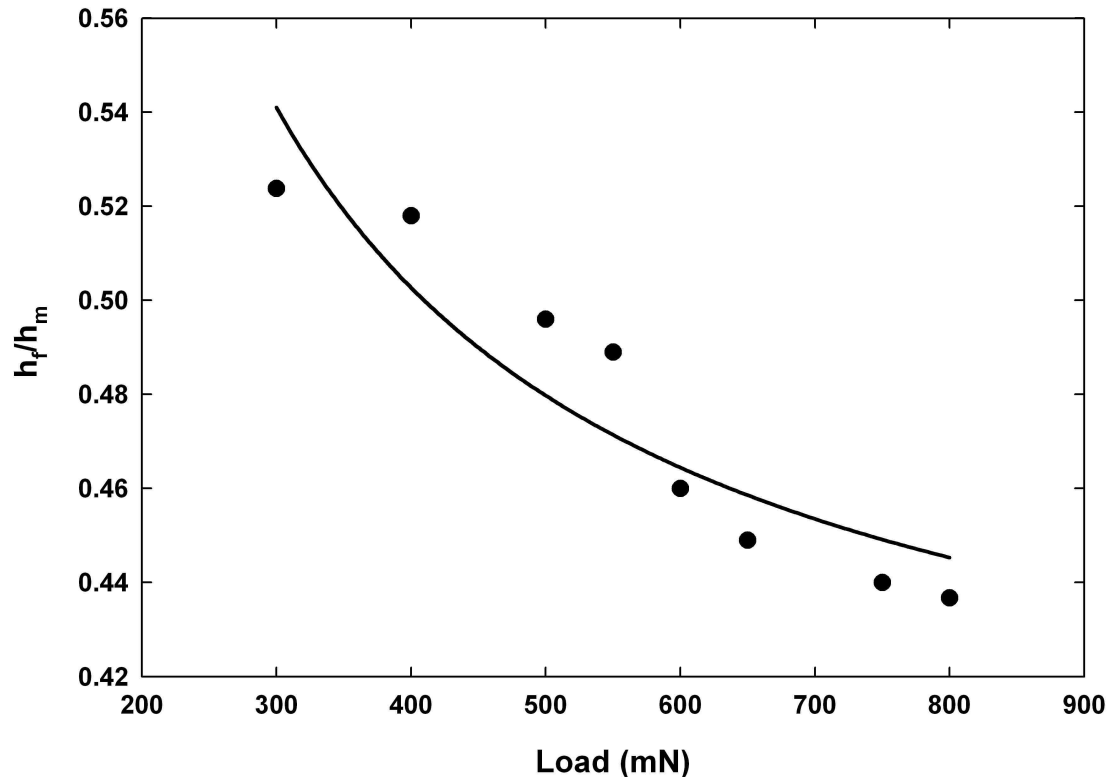


Fig. 4.2: Ratio of the penetration depth at complete unloading, h_f , and the maximum penetration depth, h_m , as a function of indentation load. The h_f/h_m ratios decrease slightly with increasing load. This predicts the increased tendency of work hardening behaviour in silicon particles with load.

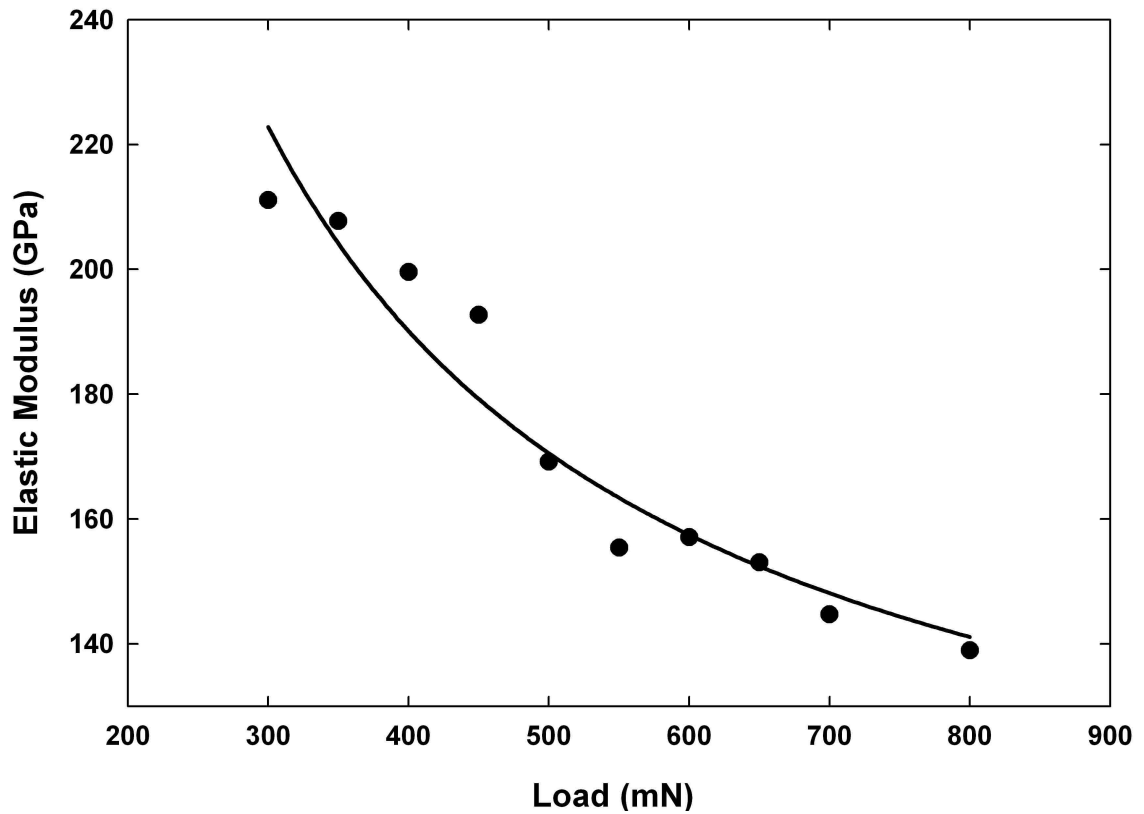


Fig.4.3: Plot showing the influence of the indentation load on the measured elastic moduli of silicon particles. This change in the values can be explained by the change of the slope of the unloading curve of the indentation experiments as in Fig. 4.1(a).

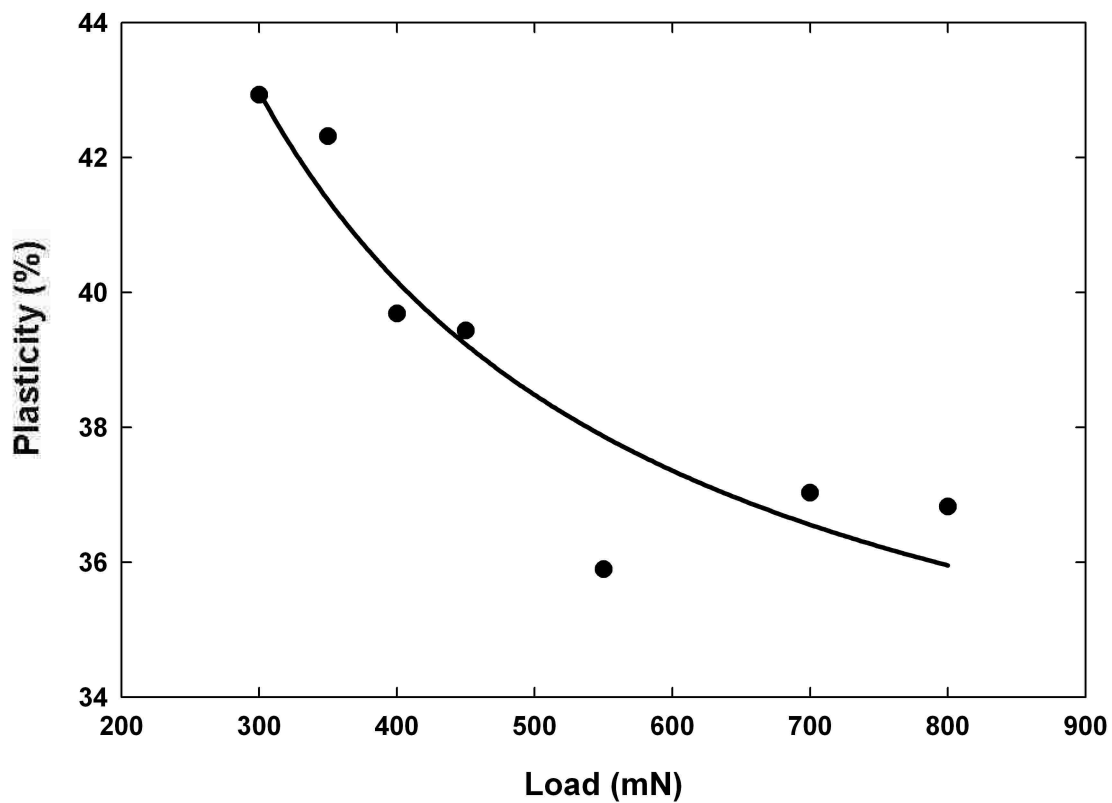


Fig.4.4: Plot depicting the plasticity (ratio of the plastic work done to the total work) involved in the silicon particles expressed as a function of the indentation load. Results indicate that this ratio decreases with load and thus the work of indentation is also load dependent.

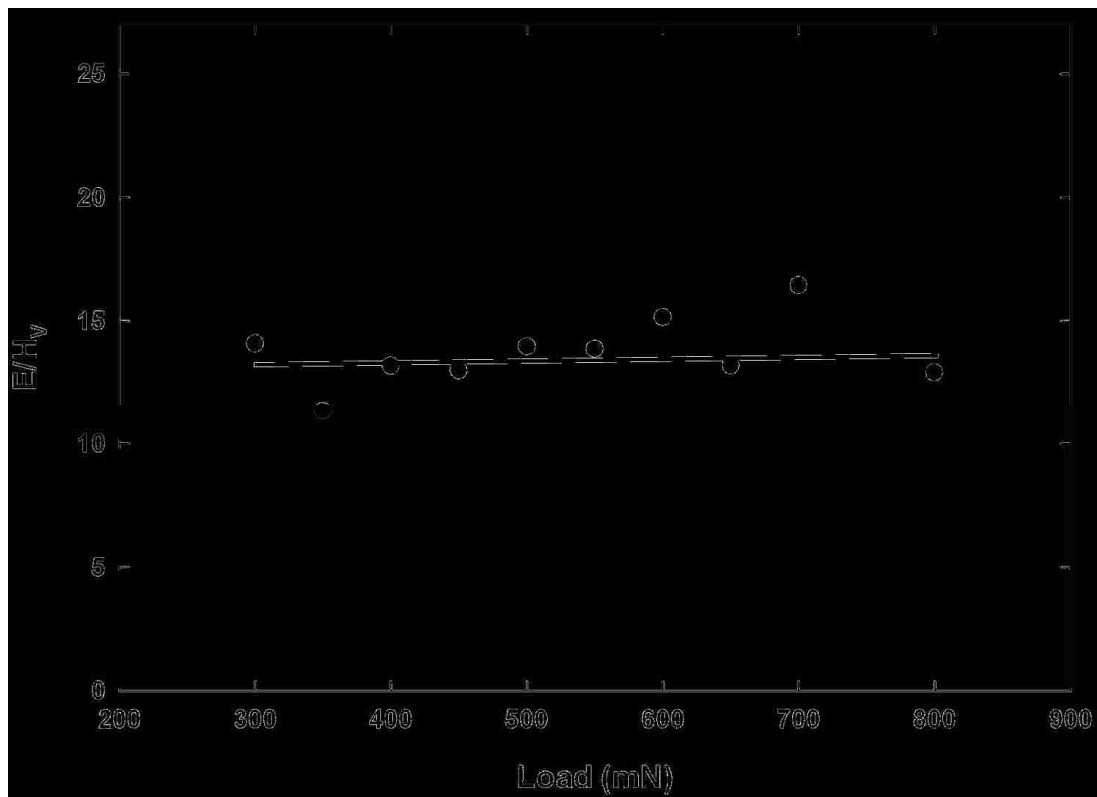


Fig.4.5: Plot showing that the ratio of the elastic modulus (E) and the Vickers hardness no. (H_V) of silicon particles (obtained from Figs. 4.3 and 3.5, respectively) is indentation load independent.

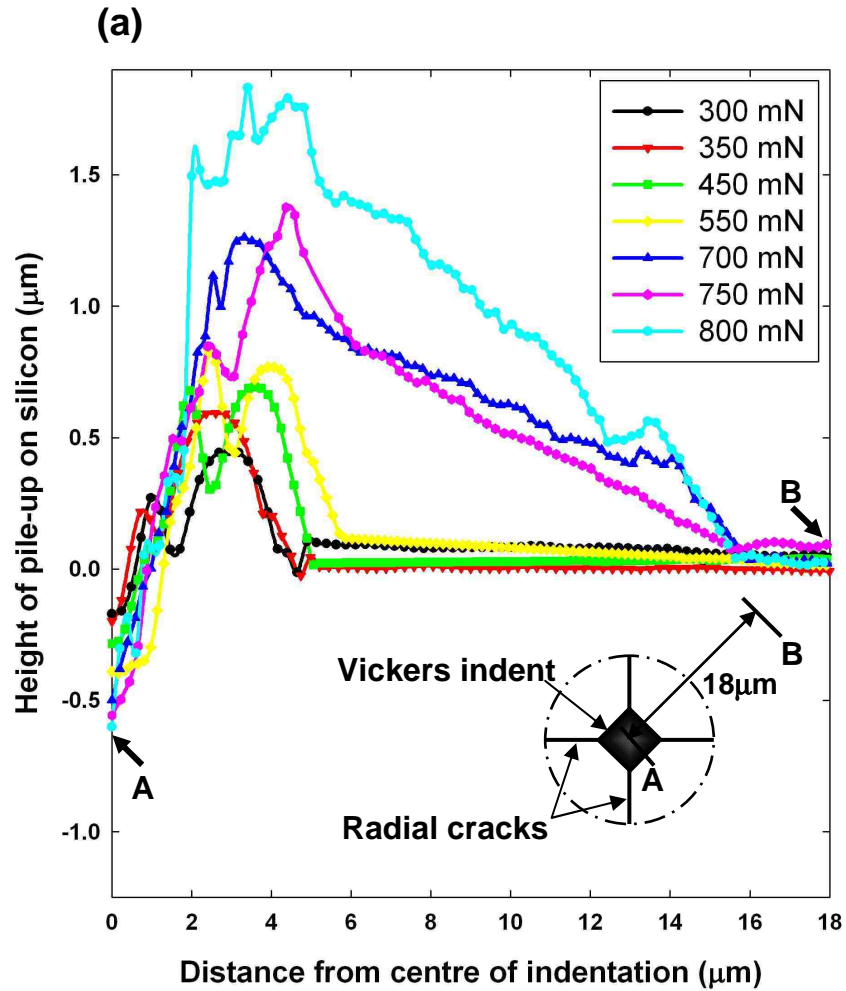


Fig.4.6: (a) 2-dimensional profiles of indentation pile-ups starting from the centre of indentations to the silicon in Al-18.5wt.%Si, plotted as a function of the indentation load. A schematic explaining the limits of the 2-dimensional profiles is shown as an inset in (a). (b) Plot of indentation load vs. top points of the pile-ups found on silicon particles, and the depth of penetration.

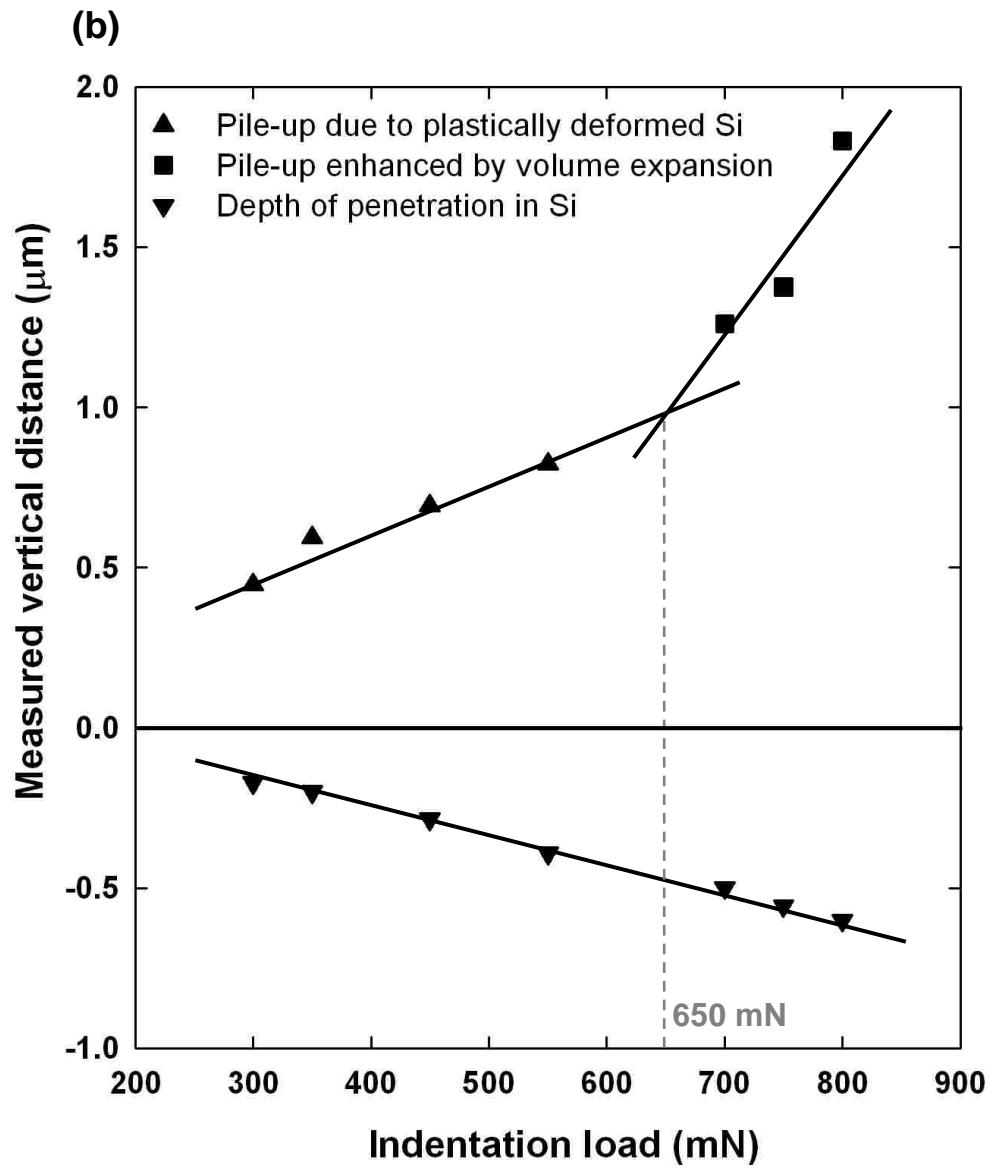


Fig.4.6: Contd.

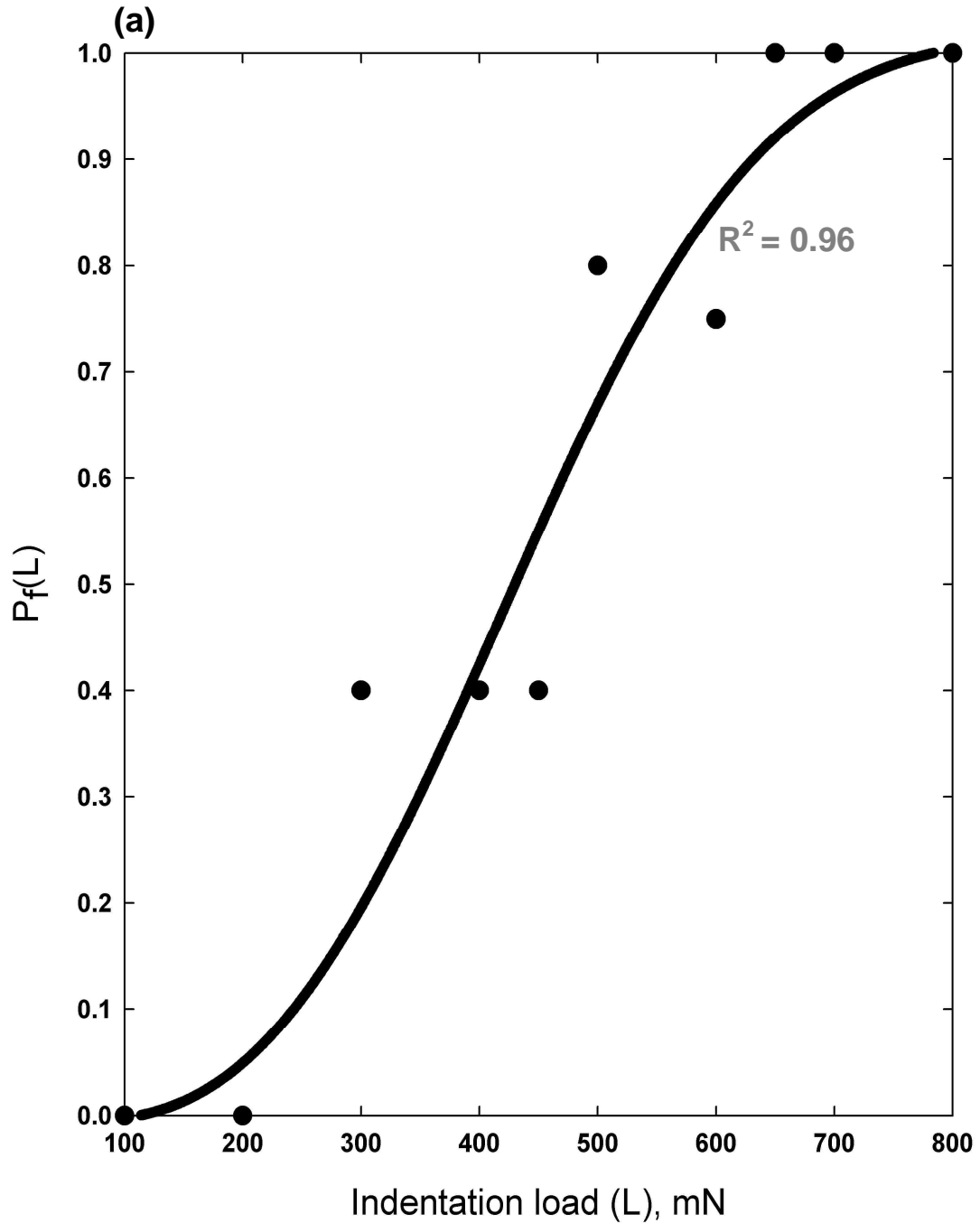


Fig.4.7: (a) Plot showing the probability of subsurface lateral cracks in silicon particles reaching the surface [$P_f(L)$], as a function of the indentation load (L). An exponential curve fits the experimental data. (b) A Weibull distribution function plotted with the data points of the exponential trend in (a), and a Weibull probability curve is the inset which gave a modulus of 3.5.

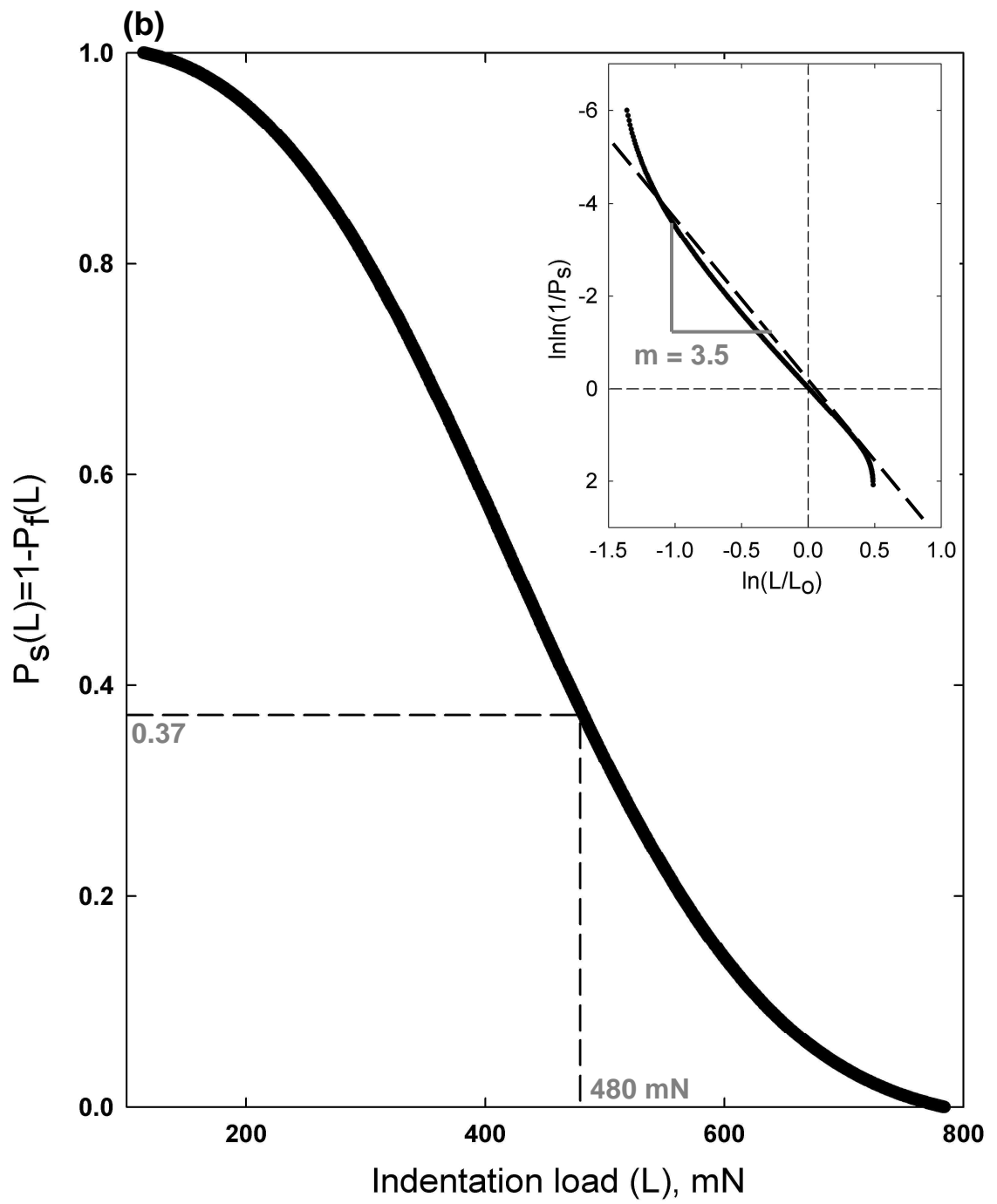


Fig.4.7: Contd.

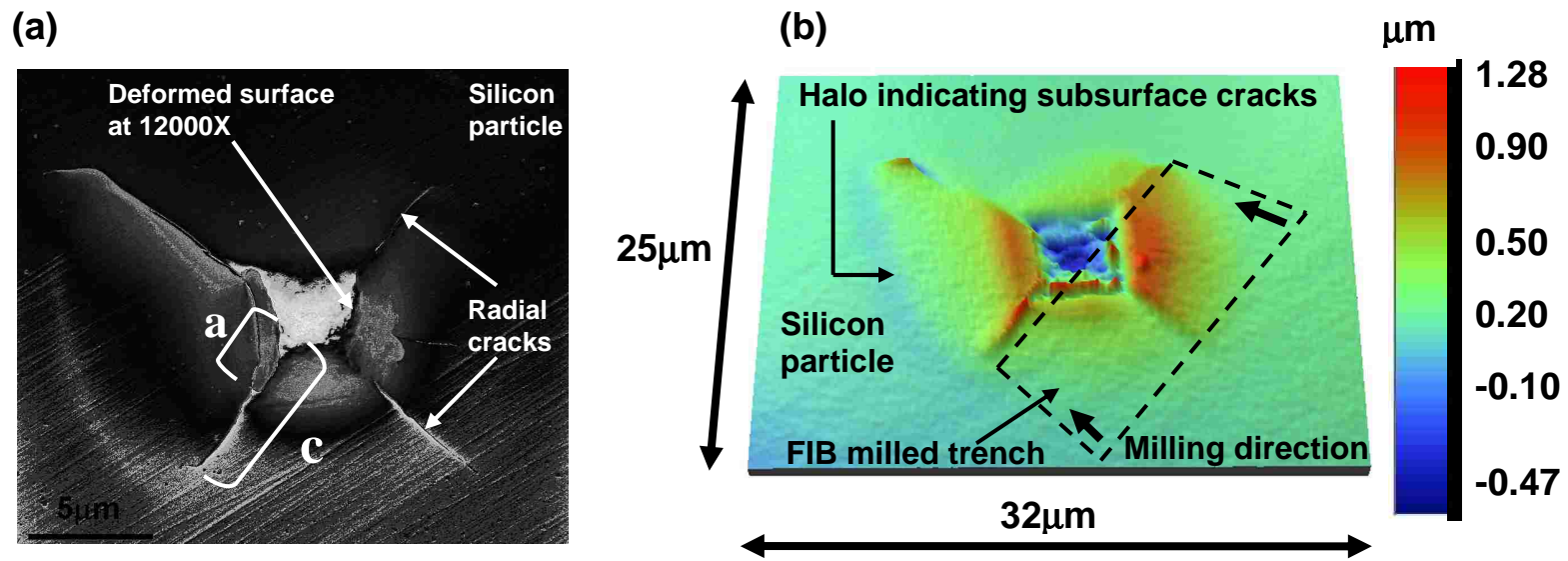


Fig.4.8: (a) An SEM image of a 475 mN Vickers indentation on a silicon particle, revealing the deformed surface of the residual indent. (b) A 3-dimensional surface profilometry image of the same indentation in (a), showing the halo due to subsurface lateral crack formation. The region of the FIB-milled trench has been shown with a dotted frame. (c) A SEM image of the FIB-milled region (cross-sectional view) of the same indentation as in (a) and (b), showing a semi-circular plastic core below the residual indent, and the subsurface crack pattern of the silicon particle.

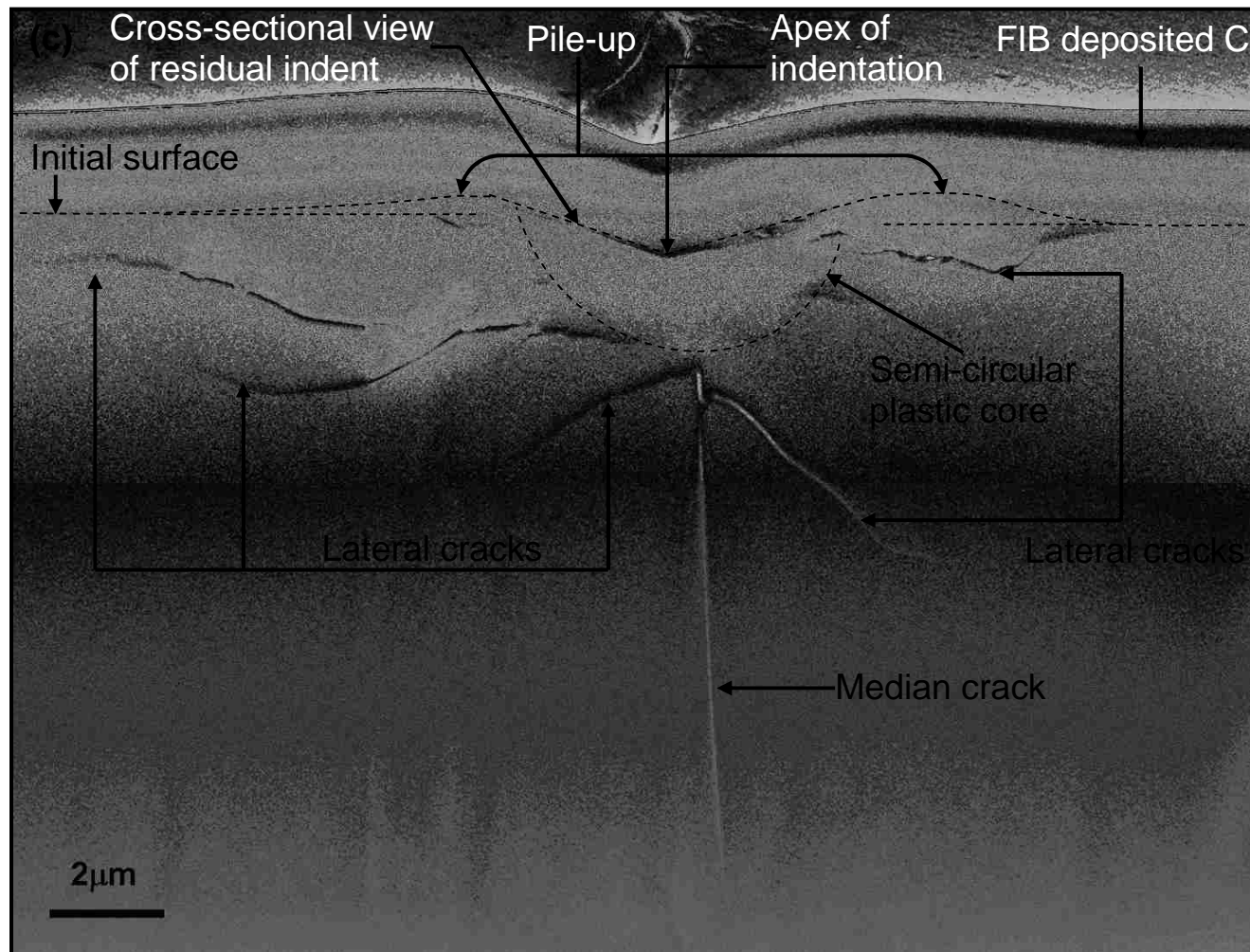


Fig.4.8: Contd.

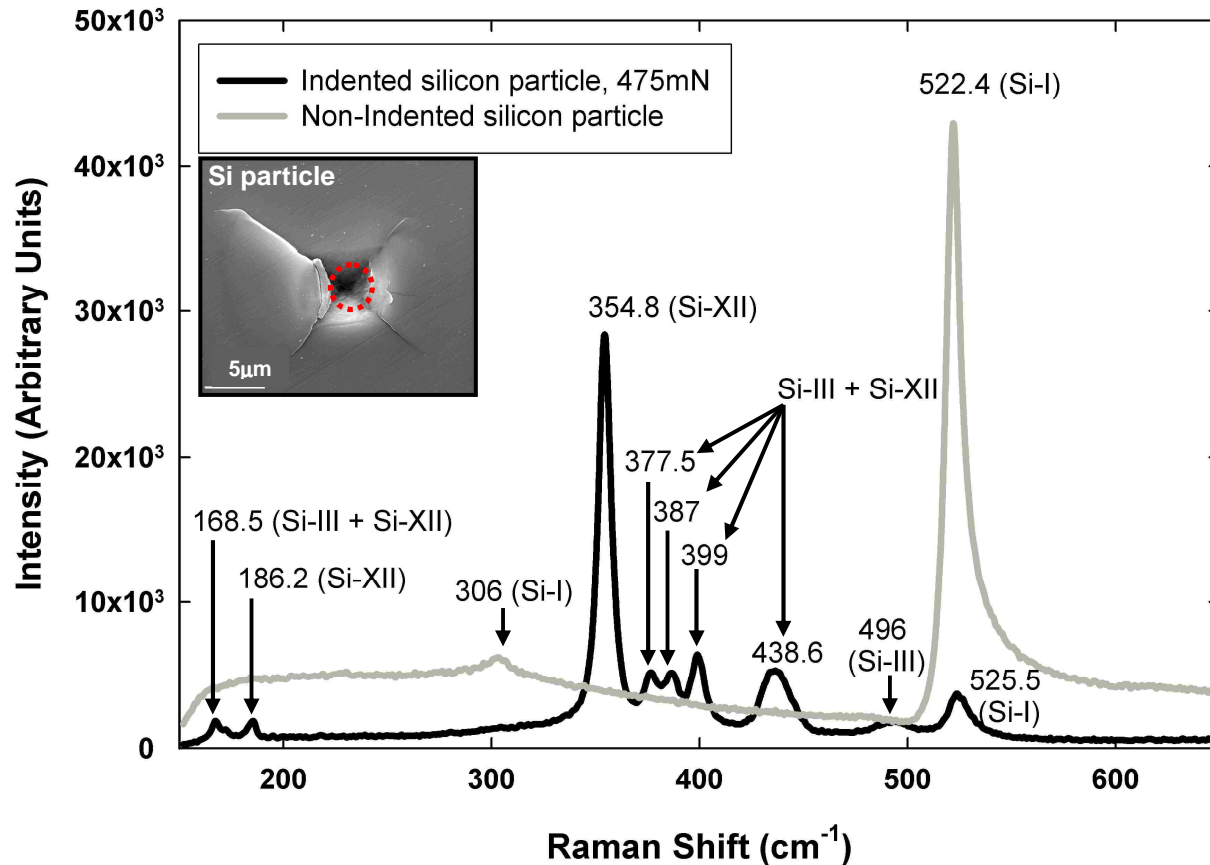


Fig.4.9: Raman spectra collected from silicon particles in Al-18.5Wt.%Si. The gray curve is the spectrum obtained from a non-indented silicon particle, having Raman bands at 522.4 cm^{-1} (strong and sharp) and 306 cm^{-1} (weak and broad). The black curve is the spectrum obtained from the centre of a 475 mN Vickers micro-indentation on a silicon particle shown in the inset, having Raman bands (due to metastable crystalline phases of silicon in the indentation deformed surface) at 168.5 cm^{-1} , 186.2 cm^{-1} , 354.8 cm^{-1} , 377.5 cm^{-1} , 387 cm^{-1} , 399 cm^{-1} , 438.6 cm^{-1} , 496 cm^{-1} and 525.5 cm^{-1} . Objective, 50X.

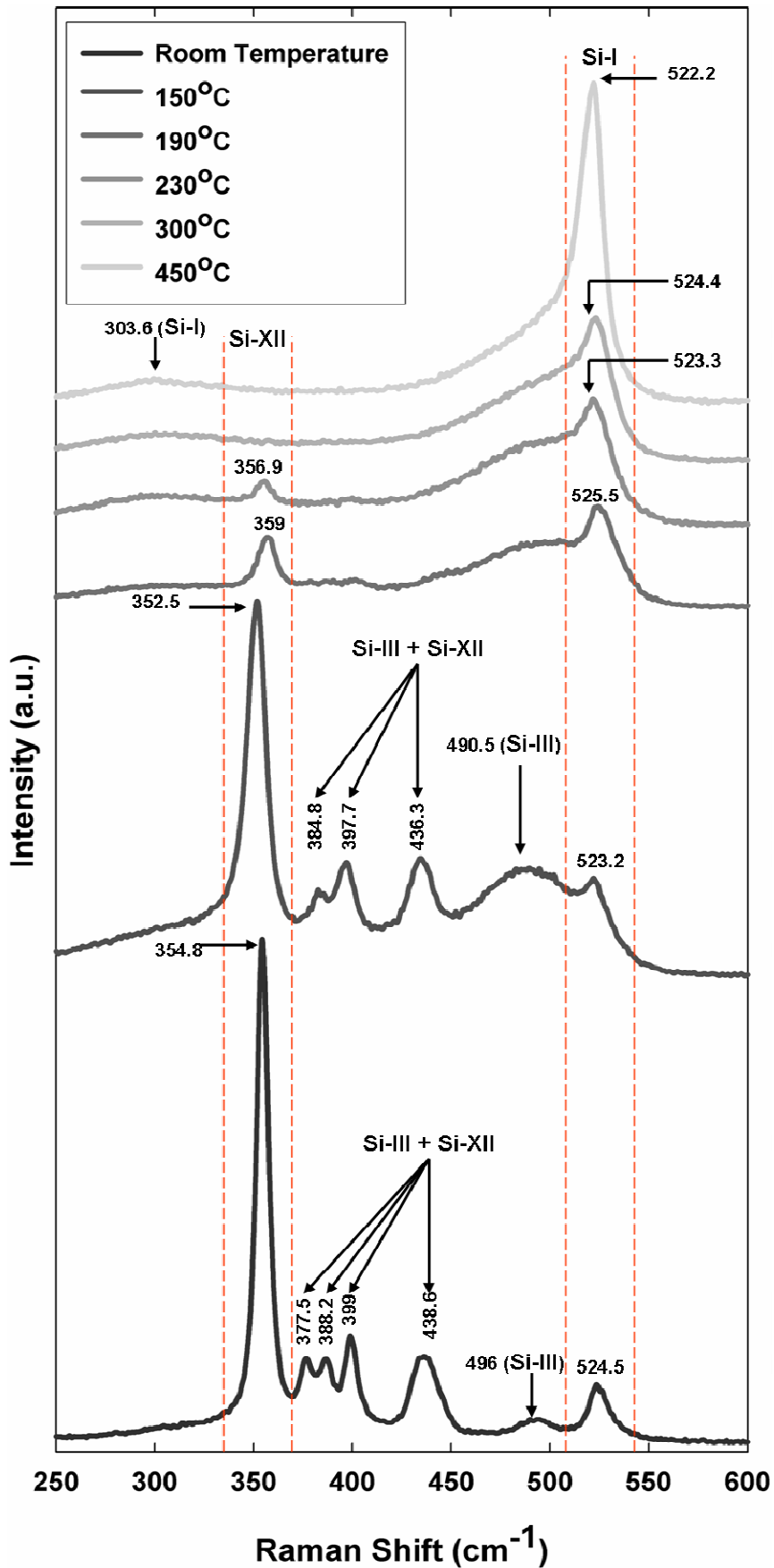


Fig.4.10: Micro-Raman spectra from indented silicon particles (400 mN) in Al-18.5wt.%Si samples and heat treated at five different temperatures for 2 hrs with subsequent air-cooling.

CHAPTER 5: Discussions

5.1. Comparison of Material Properties of Different Second Phases in Al-18.5wt.%Si with Monolithic Silicon: Weibull Statistical Analysis

Material properties, like hardness and fracture toughness, is unaffected by specimen dimensions or type of loading, provided that the specimen dimensions are large enough to accommodate the plastic zone, ensuring plain-strain conditions around the crack tip [101]. But due to the considerable brittle nature of silicon, some amount of scatter was found in the measured hardness and fracture toughness data. Understandably, comparison of these properties obtained from the different second phases in Al-18.5wt.% Si and monolithic silicon was essential by employing Weibull statistics.

5.1.1. Comparison of Hardness Values

Micro-hardness values of silicon particles in Al-18.5wt.%Si were compared with those of single crystal silicon for estimating the variability. The load for the hardness measurements was 300 mN. 30 tests were performed with each sample. The hardness values were ranked for obtaining a Weibull probability plot [Fig. 5.1]. The importance of the Weibull modulus, m , has been described in Section-2.9.1. The experimental values obtained from the two different samples were close and the Weibull moduli showed that the hardness values of the silicon particles ($m = 8.24$) was slightly less consistent than those obtained from single crystal silicon ($m = 8.78$). Apart from this, another Weibull probability plot [Fig. 5.2] was constructed with the hardness values obtained from the other second-phases, namely, $\text{Al}_{15}(\text{Fe},\text{Mn})_3\text{Si}_2$ and the ductile $\theta\text{-Al}_2\text{Cu}$. 20 hardness tests were performed on each of these phases under a load of 100 mN. As expected, a lot of

variation was found in the hardness values of the θ -Al₂Cu phase ($m = 4.1$) compared to the Al₁₅(Fe,Mn)₃Si₂ phase ($m = 8.3$).

5.1.2. Comparison of the Fracture Toughness (K_{IC}) Values

The indentation fracture toughness (K_{IC}) of silicon particles in Al-18.5wt.%Si was measured using the crack-length method described in Section-3.3 using different K_{IC} equations (**Table 3.1**). Similarly, K_{IC} was also calculated for silicon single-crystal, and the values obtained with both samples using different equations were analyzed using Weibull statistical measure. **Figs. 5.3** and **5.4** are Weibull plots comparing sets of K_{IC} data of silicon particles and monolithic silicon obtained using two different K_{IC} equations. Results showed that the scatter in the K_{IC} data of silicon single crystal ($m = 18.9$) was much less compared to that of the alloyed silicon particles ($m = 9.8$). Also, Weibull statistical analysis with the K_{IC} data of the Al₁₅(Fe,Mn)₃Si₂ phase ($m = 10$) in **Fig. 5.5** showed that the values were comparatively less variable than those of the silicon particles in the same alloy.

5.2. Pressure-induced Phase Transformations in Silicon Particles

The results given in Chapter 4 provided a general description of the nature of surface and subsurface crack formation in silicon particles due to the application of a sharp indenter. This section discusses the cause of phase transformations accompanying subsurface damage in the silicon particles by estimating the pressure exerted by the indenter.

A uniform hydrostatic pressure is assumed to exist throughout the plastic core in silicon [**Fig. 4.8(c)**], which is equal in magnitude to the pressure applied due to

indentation. The mean pressure in the plastic core of an indentation, P_m , was derived by Johnson [102] by considering the expansion of an incompressible hemispherical core of material subjected to an internal pressure [Fig. 5.6].

$$P_m = \frac{2Y}{3} \left[1 + \ln \left\{ \frac{\left(\frac{E}{Y \cot \psi} \right) + 4(1-2\nu)}{6(1-\nu)} \right\} \right] \quad (5.1)$$

For a Vickers indenter, $2\psi = 136^\circ$, and for single crystal silicon [103], yield strength (Y) = 7,000 MPa, elastic modulus (E) = 190 GPa [calculated from indentation load-displacement curves as in Fig. 4.1(a) and following Eq.4.1], and Poisson's ratio (ν) = 0.28, Eq.5.1 gives $P_m = 17.6$ GPa. Eq.5.1 is applicable to geometrically symmetrical indentations. Tanaka [104] proposed a model considering a compressible plastic core.

$$P_m = \frac{2Y}{3} \left[1 + \ln \left\{ \frac{\left(\frac{\sqrt{\pi E}}{Y \cot \psi} \right)}{12(1-\nu)} \right\} \right] + \alpha \quad (5.2)$$

where α is the material constant signifying the plastic work that has dissipated to heat in the core. Considering $\alpha = 1/3$ for silicon [104] and inserting the rest of the values in Eq.5.2, $P_m = 19.6$ GPa. An alternative way of calculating the pressure exerted by the indenter is to consider the plastic core radius, c , and calculate the projected area as follows:

$$L = 4\pi c^2 . P_m \quad (5.3)$$

When an indentation load (L) of 475 mN (corresponding to $P_s(L) \approx 0.37$ as calculated in Section 4.1.2) was applied, a plastic core of radius $c = 2.8 \mu\text{m}$ was formed [Fig. 4.8(c)].

According to Eq.5.3, P_m was calculated as 19.3 GPa, which is consistent with the value calculated using Eq.5.2, inferring that the pressure exerted by a symmetrical indenter is load independent, and depends largely on the material properties, namely yield strength, elastic modulus and Poisson's ratio.

Evidently, the pressure exerted by the indenter (19.3 GPa) exceeds the threshold pressure (11.2-12.0 GPa [50]) necessary to induce phase transformation from Si-I to Si-II. Section 3.3 described the silicon phase transformations that occurred in the deformed surface of the residual indent, where the Si-I peak at 522.4 cm^{-1} in the unstressed silicon particle in **Fig. 4.9** shifted to 525.5 cm^{-1} . This observation is consistent with those made on bulk silicon samples [105, 106]. In fact the transformation of original Si-I to Si-II, in the residual indent in silicon particles, is a necessary preceding step for the formation of other metastable crystalline phases of silicon, namely, Si-III and Si-XII (as depicted in **Fig. 4.9**), from Si-II during pressure release. Apart from these crystalline phases, evidence was found for local amorphous silicon (a-Si) regions by high resolution TEM, as discussed in Section 5.3. Also, it is essential to mention here that as seen in **Fig. 4.10**, the metastable phases of silicon disappear at temperatures below 480°C . Thus, it can be concluded that if the metastable phases are present in deformed silicon particles, they revert back to the diamond cubic structured Si-I at temperatures high enough to cause change in silicon particle morphology.

5.3. Analysis of Subsurface Damage Mechanisms

The micromechanisms of damage have been analyzed in detail in this section. The damaged structure under a Vickers indentation exhibited characteristic median and lateral cracks. A cross-sectional, bright field TEM image of the subsurface structure in **Fig.**

5.7(a) shows details of both crack systems together with the defect structure generated under the indenter. The presence of a crystalline state (Si-I) is confirmed; the selected area electron diffraction (SAED) pattern, with [011] as the zone axis [**Fig. 5.7(b)**] taken from a region indicated located immediately underneath the residual indentation impression [marked as (b) in **Fig. 5.7(a)**], reveals diffraction spots that are consistent with Si-I phase. Dislocation networks were generated in the subsurface region of the indented silicon particle and evidence of dislocations has been given in **Figs. 5.7(c)** and **5.7(d)**. As room temperature slip in silicon occurs on the {111} planes, and dislocation interactions prompt the formation of Lomer or Lomer-Cottrell locks [74], nucleation of microcracks in the plastically deformed region is expected. The median crack clearly visible in **Fig. 5.7(a)** could be taken as an example of a crack formed as a result of this process. Two additional regions of interest are shown in bright-field TEM image of **Fig. 10(a)** where further details of indentation-induced phase transformations were depicted at high resolution. Lattice fringes corresponding to the {111} planes of crystalline Si-I phase with an interplanar distance of 0.313 nm are identified in the HRTEM image of **Fig. 5.8(b)**. A still closer look at the crack boundary [region indicated as (c) in **Fig. 5.8(a)**] provided evidence for localized amorphization of silicon [**Fig. 5.8(c)**]. The fast Fourier transform (FFT) derived diffraction pattern [**Fig. 5.8(d)**] obtained from this region, clearly reveals the lack of periodic lattice structure in a narrow zone of 20-30 nm in diameter surrounded by crystalline Si-I structure [**Fig. 5.8(e)**]. At this particular location, a mismatch due to difference in atomic volumes of a-Si ($21.26 \text{ \AA}^3/\text{atom}$ [107]) and its diamond cubic crystalline counterpart, Si-I ($20.76 \text{ \AA}^3/\text{atom}$ [107]), can be expected. It is conceivable that the formation of a-Si at the subsurface crack edges may have contributed

to the formation of the “pop-out” observed during the unloading stage of the indentation [Fig. 4.1(a)]. Increased volume due to localized amorphization may also restrict the closing of median cracks closing process during unloading. “Pop-outs” are often seen in the unloading curves of indentation experiments, but conclusive evidence is lacking as to whether they could be attributed to the phase transformations (from Si-II to Si-III and Si-XII), because these were not observed consistently in every indentation experiment [108].

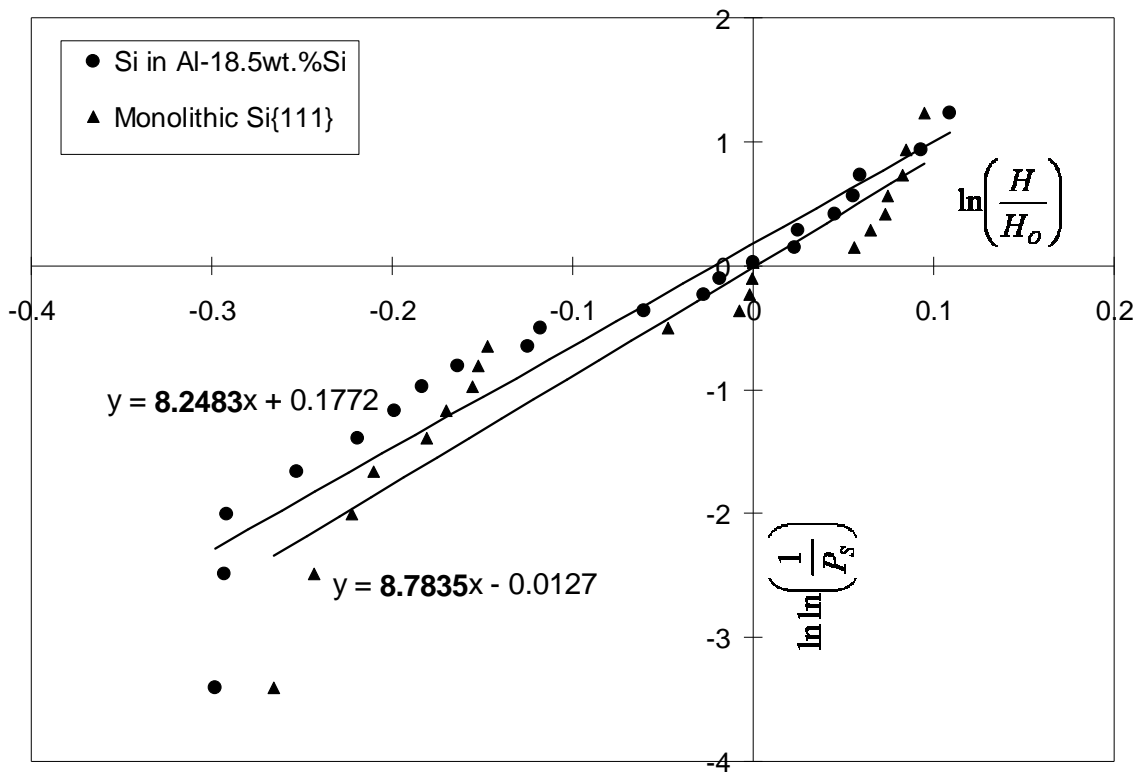


Fig.5.1: Weibull statistical analysis involving the hardness values of Si in Al-18.5wt.%Si ($m = 8.24$) and Si single crystal {111} ($m = 8.78$). The Weibull moduli in both the cases were comparable though the hardness values of Si single crystal were relatively less variable.

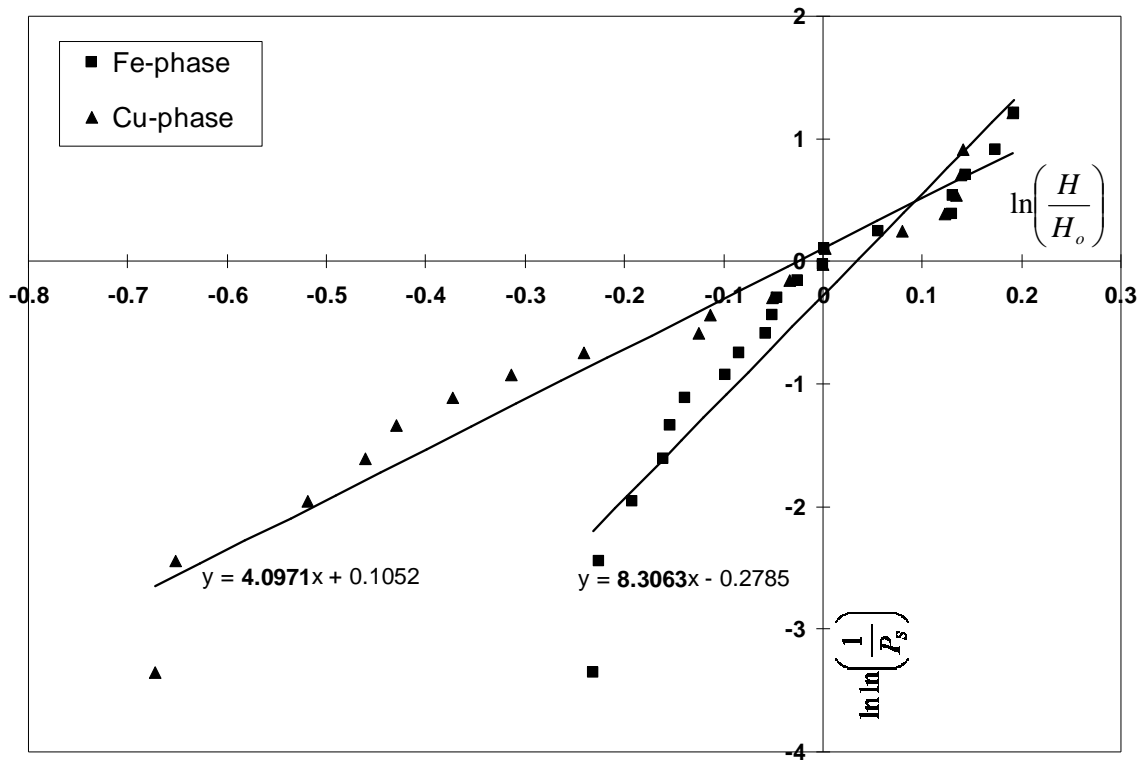


Fig.5.2: Weibull statistical analysis involving the hardness values of $\text{Al}_{15}(\text{Fe,Mn})_3\text{Si}_2$ (Fe-phase; $m = 8.3$) and the $\theta\text{-Al}_2\text{Cu}$ (Cu-phase; $m = 4$) particles in Al-18.5wt.%Si. The Weibull moduli suggested that the hardness values of $\text{Al}_{15}(\text{Fe,Mn})_3\text{Si}_2$ showed much less variation than those of $\theta\text{-Al}_2\text{Cu}$.

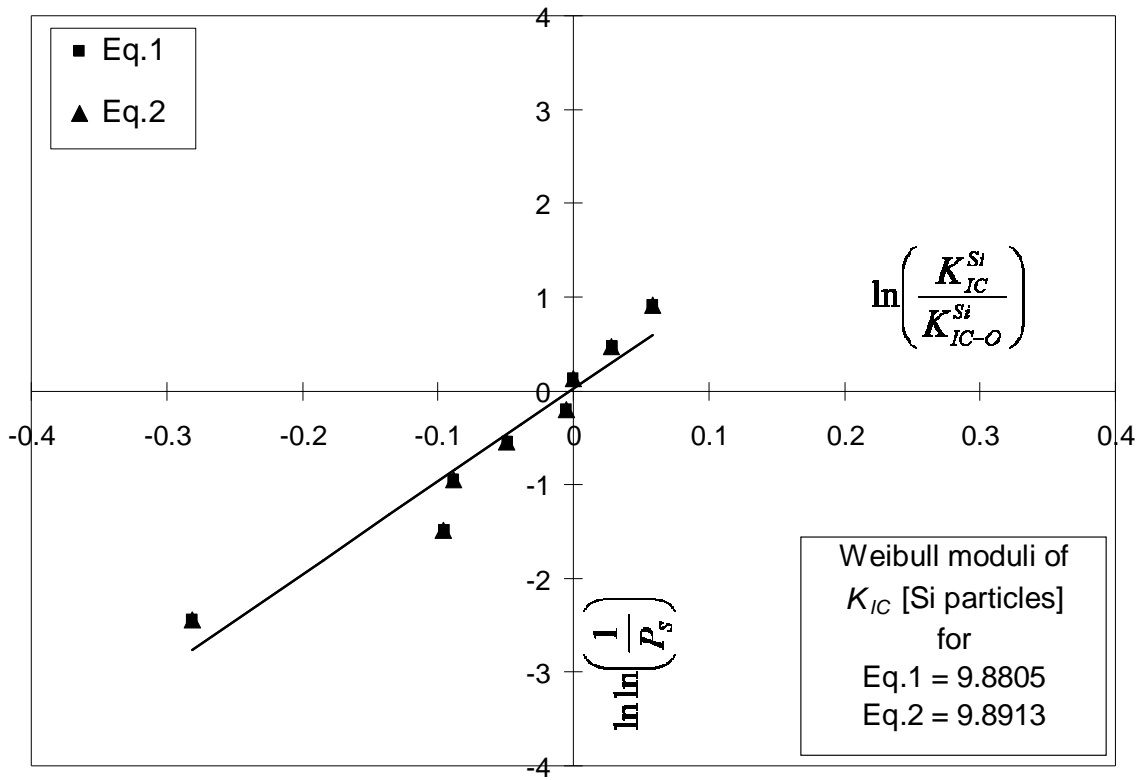


Fig.5.3: Weibull statistical analysis involving the K_{IC} values of Si particles in Al-18.5wt.%Si calculated using Eqs.1 and 2 of **Table-3.1**.

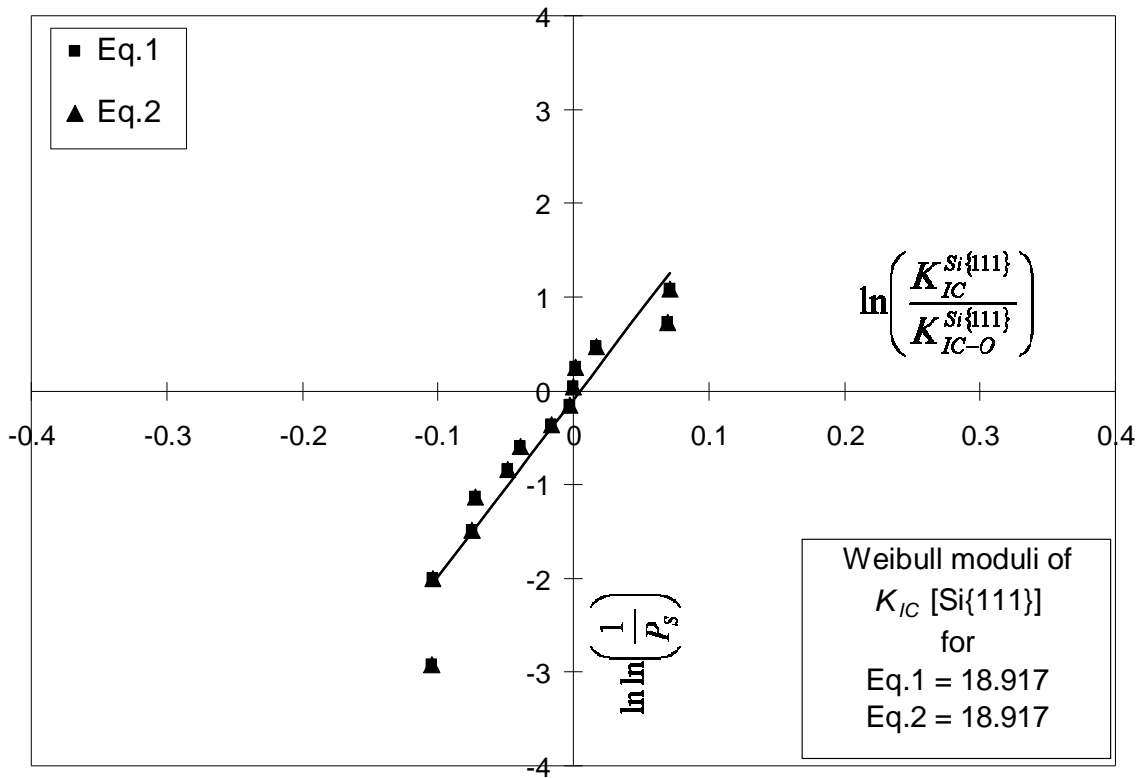


Fig.5.4: Weibull statistical analysis involving the K_{IC} values of Si single crystal {111} calculated using Eqs.1 and 2 of **Table-3.1**. Comparing the Weibull moduli, K_{IC} values in this case were much less variable than the Si particles in Al-18.5wt.%Si (**Fig. 5.2**).

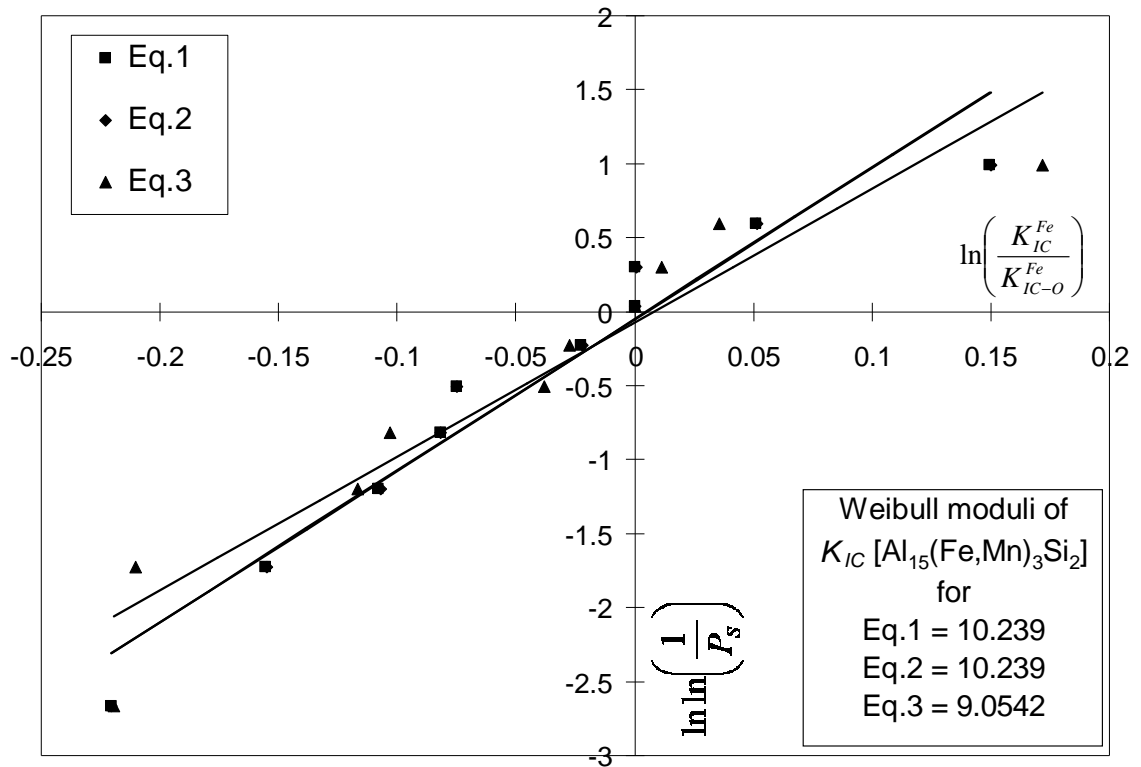


Fig.5.5: Weibull statistical analysis involving the K_{IC} values of $Al_{15}(Fe,Mn)_3Si_2$ in Al-18.5wt.%Si calculated using Eqs.1 - 3 of **Table-3.1**.

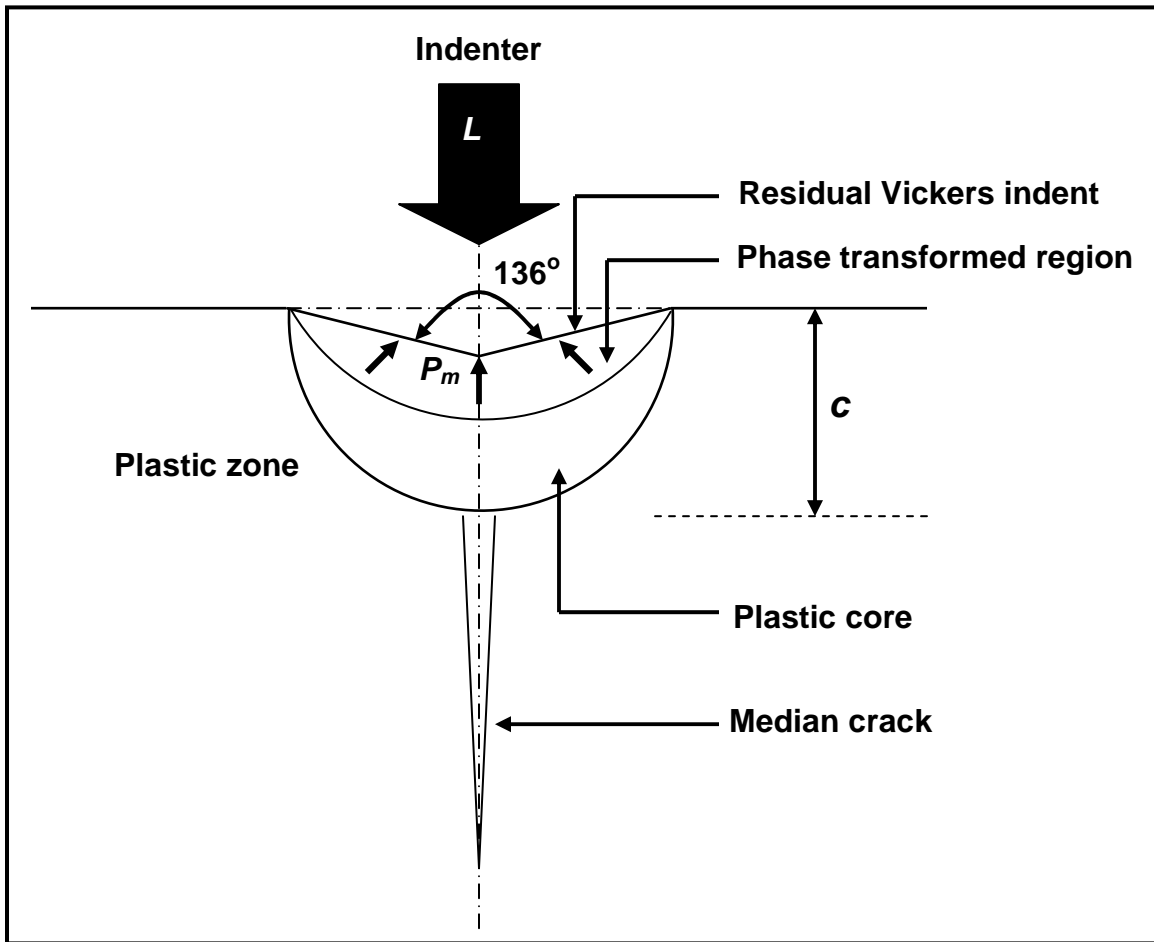


Fig.5.6: A schematic diagram of an indentation model for the calculation of pressure exerted by the plastic core. L , indentation load; P_m , the mean pressure in the plastic core; c , radius of the plastic core.

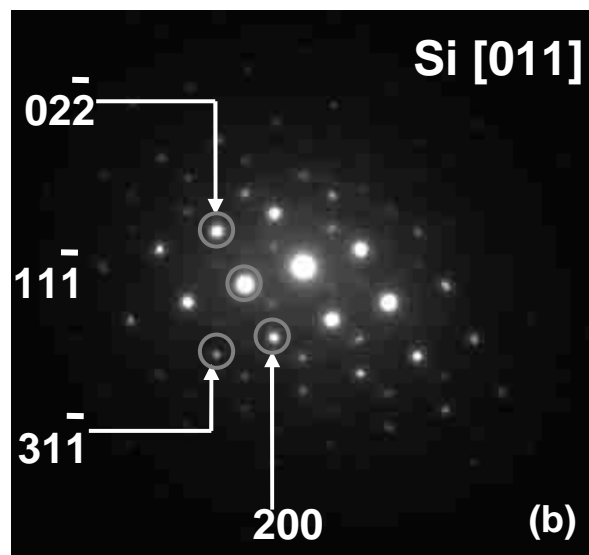
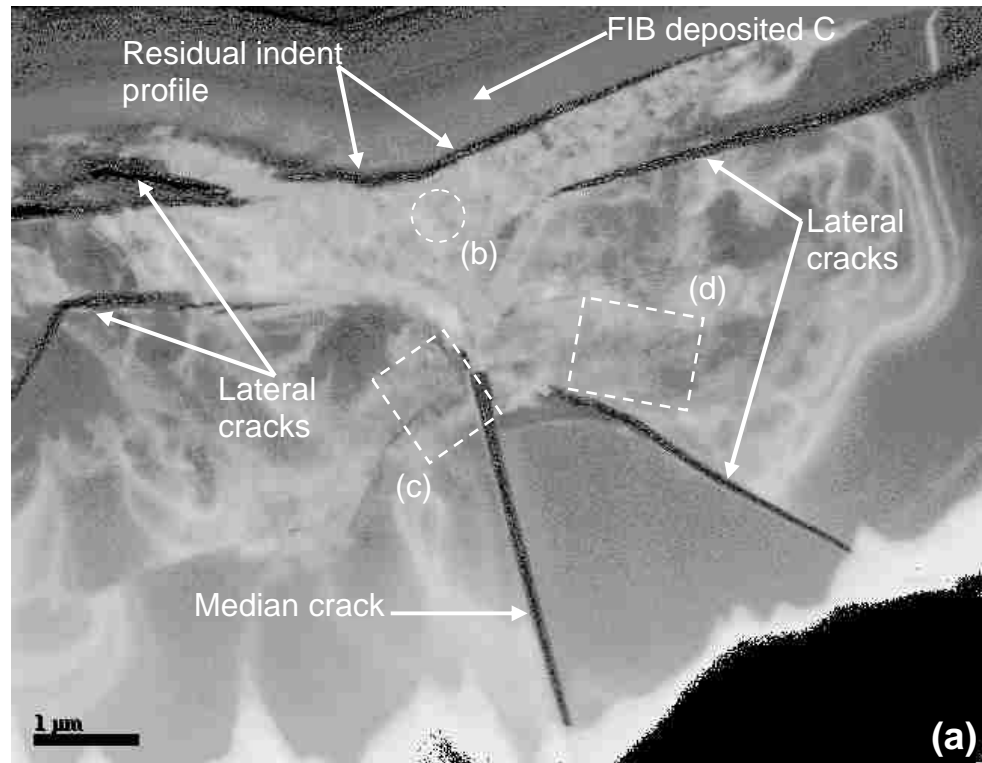


Fig.5.7: (a) A low magnification, bright-field TEM image of the deformed region underneath a 475 mN Vickers indentation. (b) SAED pattern obtained from plastically deformed region indicated as (b) in (a) with [011] zone axis. (c) and (d) are bright-field images of the regions indicated as (c) and (d), respectively, in (a), showing the existence of dislocations in the defect structure.

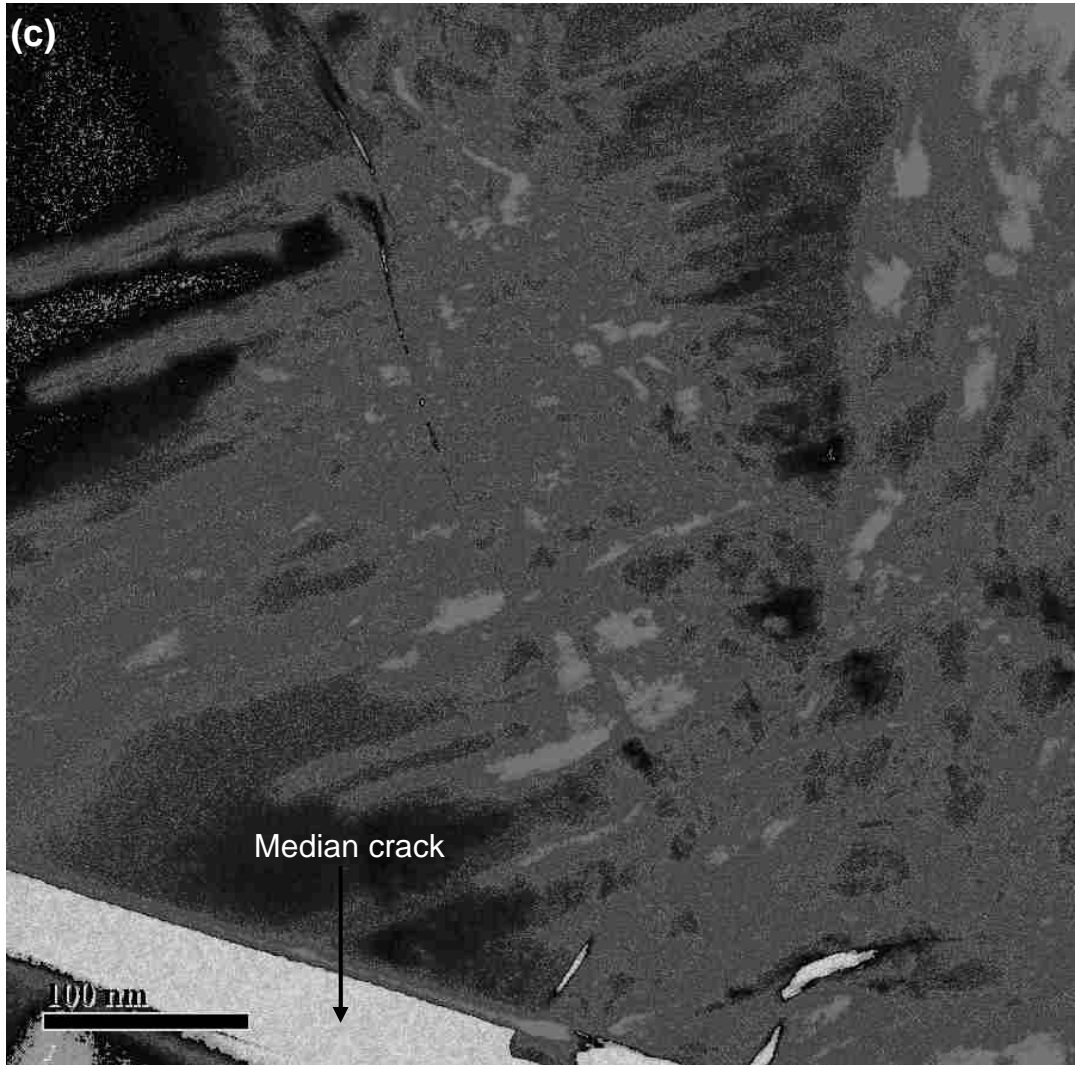


Fig.5.7: Contd.

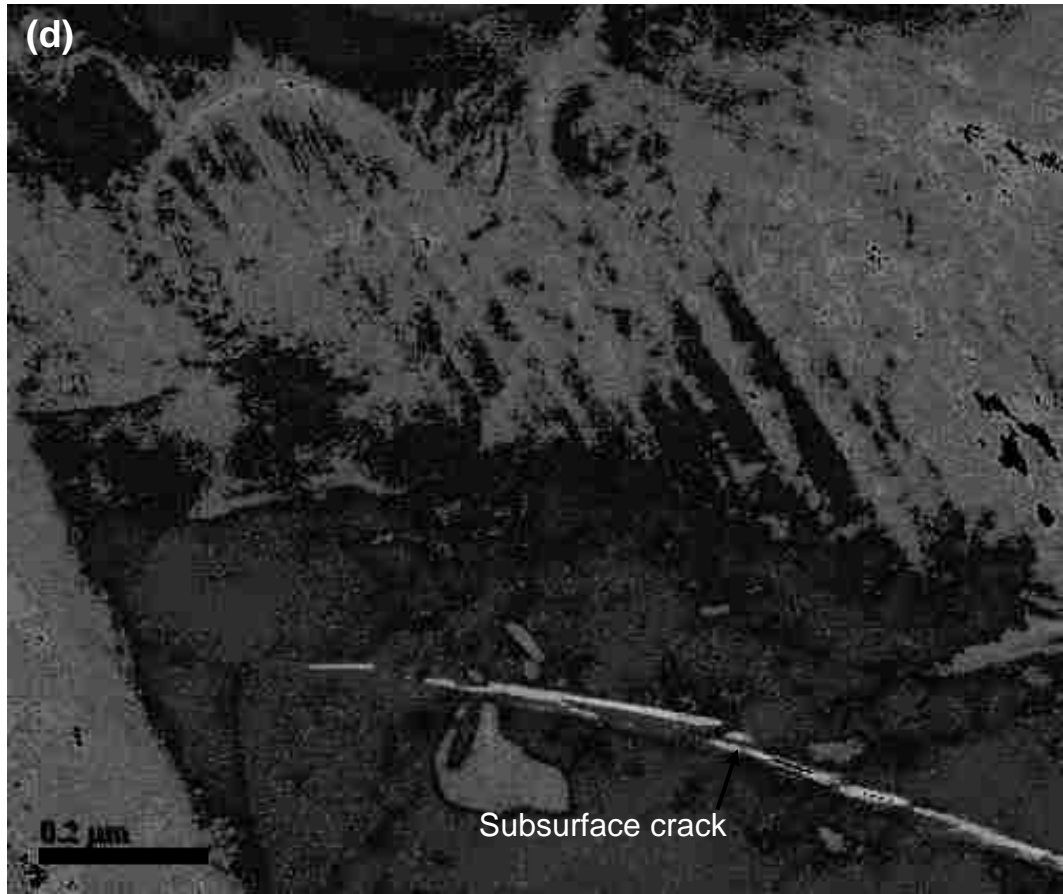


Fig.5.7: Contd.

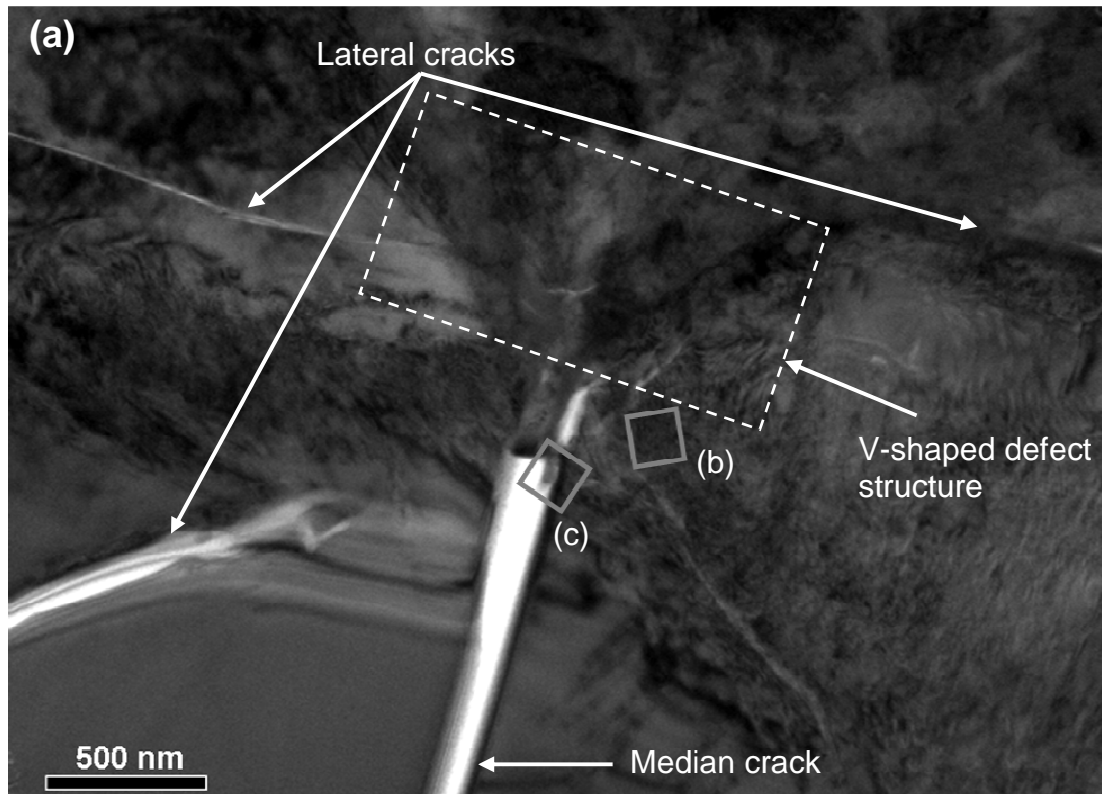


Fig.5.8: (a) A bright-field, TEM image showing the V-shaped, plastically deformed region underneath a Vickers indentation. (b) HRTEM image of the region indicated as (b) in (a), showing the lattice fringes corresponding to the {111} planes of Si-I, with a measured interplanar distance of 0.313 nm. (c) HRTEM image of the regions indicated as (c) in (a), on the median crack boundary showing an amorphous region at the crack edge. (d) and (e) are FFT-derived diffraction patterns confirming the amorphous and crystalline region respectively seen in (c).

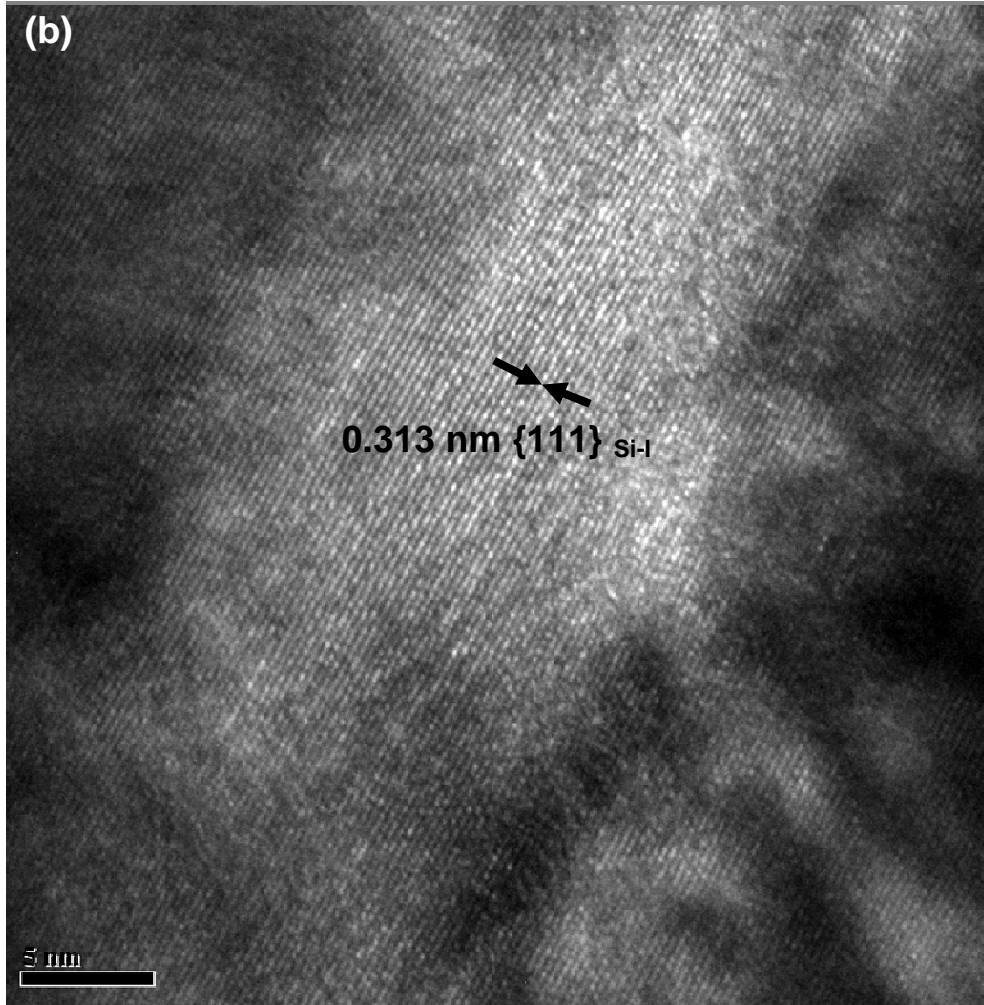


Fig.5.8: Contd.

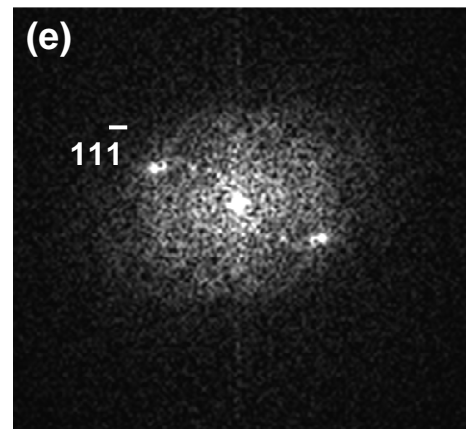
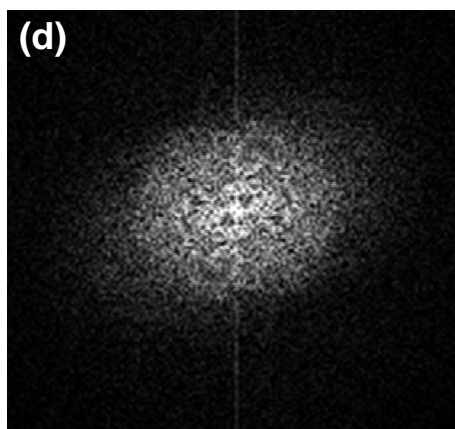
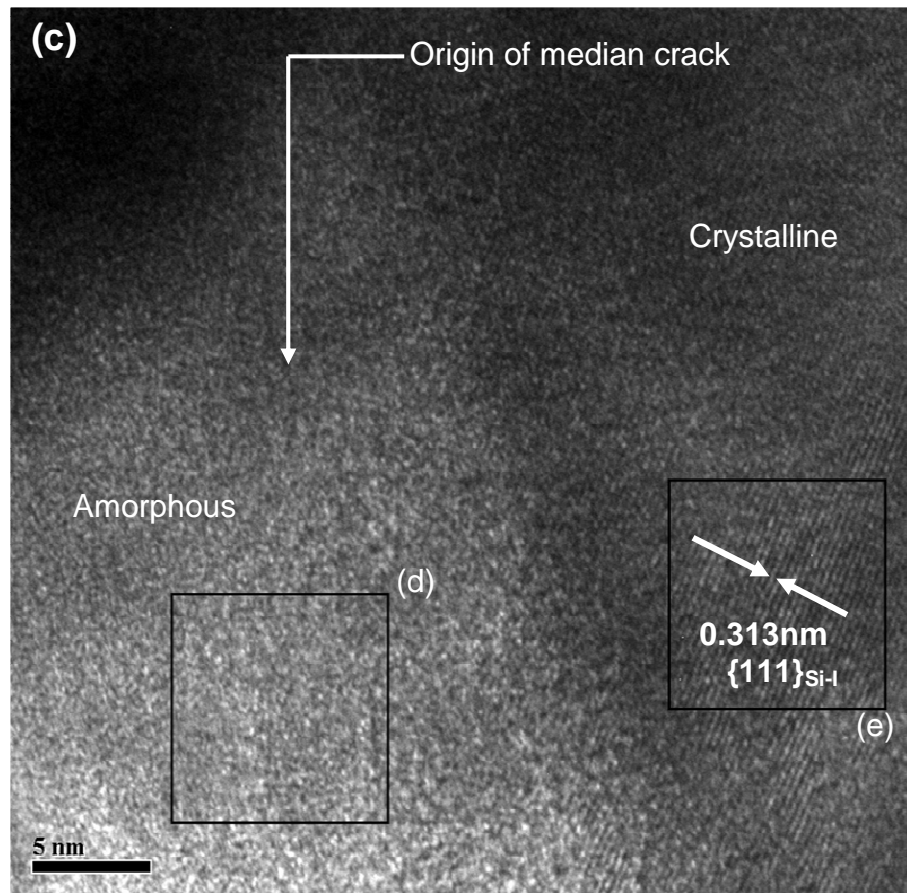


Fig.5.8: Contd.

CHAPTER 6: Summary and Conclusions

6.1. Summary

It is instructive to schematically summarize the results of analyses on phase transformation and mechanical damage events that occur during the loading and unloading stages of the indentation process applied to silicon particles, as in **Fig. 6.1**. The following observations accompany the schematic description in **Fig. 6.1**:

(i) During the loading stage, radial/median cracks appear from the corners of the indentation and also inside the silicon particle. The application of a pressure, estimated as 19.3 GPa, causes transformation of silicon from diamond cubic Si-I, to metallic β -Sn-structured Si-II. Dislocation networks are generated in the indentation defect structure of silicon.

(ii) During the unloading stage, the radial cracks start to close as lateral cracks are nucleated underneath the plastic core, propagating parallel to the surface. Volume mismatch between crystalline Si-I and a-Si at the median crack boundary, in a region immediately below the plastic core is a plausible cause for the nucleation of such cracks. The probability of these nucleated subsurface cracks reaching the surface increases with the load and obey a Weibull probability function. Due to pressure released during unloading, Si-II is transformed into a mixture of metastable crystalline phases of silicon, namely rhombohedral Si-XII and bcc Si-III, as detected in the residual microindents.

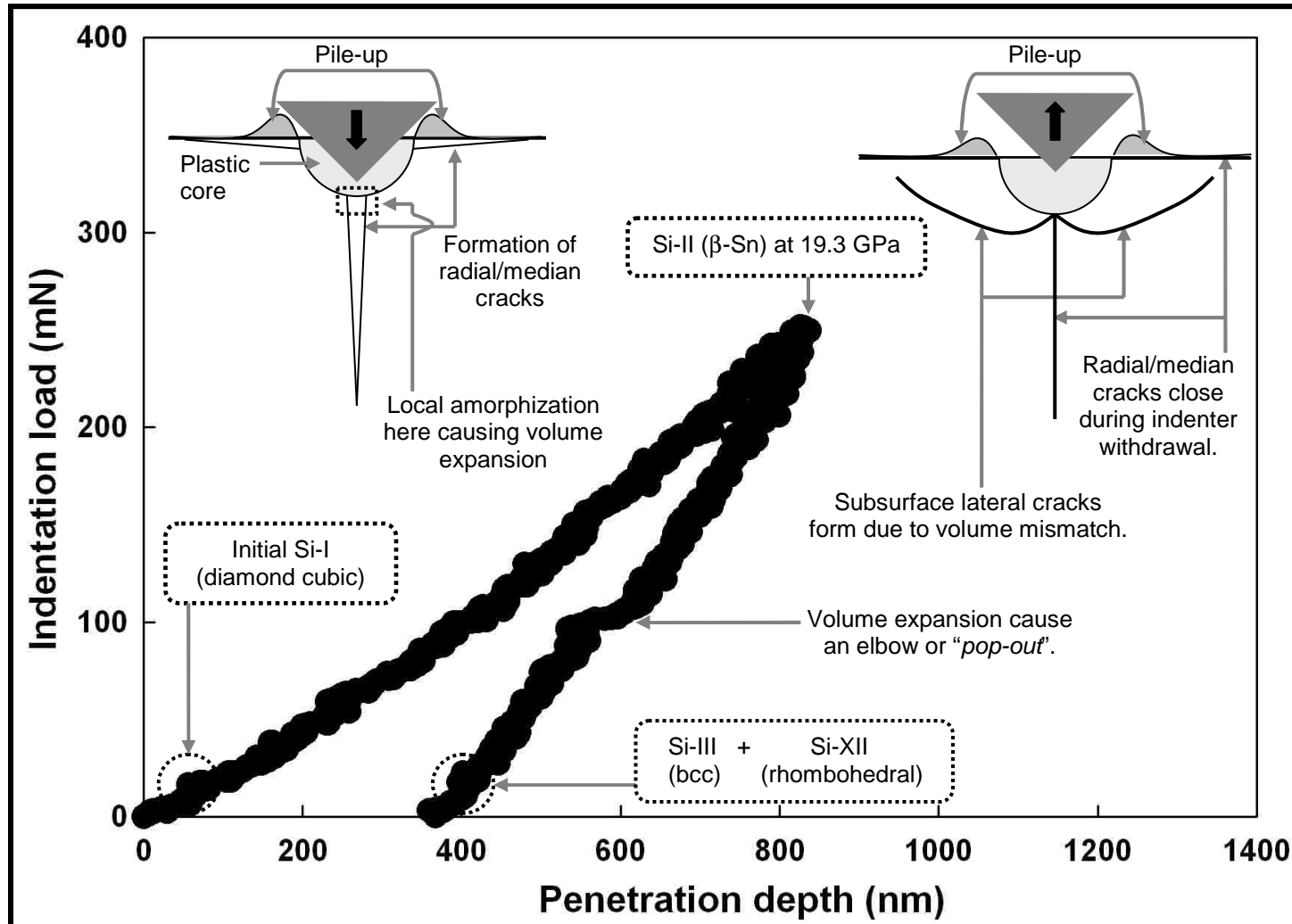


Fig.6.1: A schematic diagram depicting the deformation and phase transformation related phenomena occurring in the silicon particles of Al-18.5wt.%Si during the loading and unloading stages of Vickers indentations.

6.2. Conclusions

Vickers micro-indentations were done on the second-phases of an Al-18.5wt.% Si alloy and on the {111} surface of monolithic silicon. Indentation-induced subsurface damage mechanisms, and phase transformations in the silicon particles in Al-18.5wt.% Si were studied. The main conclusions are as follows:

- 1) The material properties, hardness and indentation fracture toughness (K_{IC}), of Si, $Al_{15}(Fe,Mn)_3Si_2$ and $\theta-Al_2Cu$ phases of Al-18.5wt.%Si were determined and compared with those of monolithic Si {111}. For the silicon particles, the calculated K_{IC} values varied within a range of 0.97 and 1.6 $MPa \cdot m^{0.5}$, whereas for $Al_{15}(Fe,Mn)_3Si_2$, the value was found to vary between 0.74 and 1.01 $MPa \cdot m^{0.5}$. Weibull statistical analyses showed that both the hardness and K_{IC} values of the alloyed silicon particles were more variable compared to those of monolithic silicon.
- 2) Pile-ups were formed around the edges of the Vickers indentations due to the displacement of plastically-deformed silicon at low loads. At higher indentation loads (>650 mN), volume expansion due to subsurface crack formation contributed pile-up formation.
- 3) Lateral crack growth led to “chipping-out” fracture. The probability of these cracks reaching the surface was shown to follow Weibull statistics with a low modulus ($m = 3.5$) inferring high variation in silicon fracture probability within the load range studied.

- 4) The high pressure exerted by the indenter calculated as 19.3 GPa, induced transformation of the original diamond cubic Si-I structure to almost completely into other metastable crystalline forms of silicon, namely bcc Si-III and rhombohedral Si-XII.
- 5) The metastable phases were found to revert back to diamond cubic Si-I at elevated temperatures with the actual transformation taking place between 150°C and 190°C. At temperatures (~450°C) just below 480°C, where the kinetics of particle morphology change initiates, the silicon particles assumes diamond cubic structure, denoting complete phase reversal.
- 6) A localized amorphous silicon (a-Si) region was observed at the median crack boundary immediately below the plastic core, suggesting the possibility of the volume mismatch between a-Si and Si-I to contribute to subsurface crack formation.

6.3. Future Work

Present scenario suggests that silicon indentation contact mechanics is at a highly advanced stage. But still research on the following will add light to our present conceptual understanding of second phase silicon particle fracture in Al-Si alloys.

- 1) Analysis of in-situ high temperature deformation due to sharp indentation on silicon particles. This will be interesting as room temperature indentation deformation mechanism in silicon particles has already been studied meticulously.
- 2) Investigation of the role of phase transformation on fracture of silicon particles at elevated temperatures. This study can be done by detailed high resolution electron microscopy.

- 3) Molecular dynamics simulations for confirming the role of localized amorphous silicon sections on subsurface crack formation in silicon particles during room temperature indentation. The results will make this study entirely complete.

REFERENCES

- [1] C. H. Hager Jr., A. E. Segall, J. C. Conway Jr., H. Dang, M. F. Amateau, *Tribological Transactions*, 46 (2003) 206-210.
- [2] M. Elmadagli, T. Perry, A. T. Alpas, *Wear*, 262 (2007) 79-92.
- [3] H. Ye, *Journal of Materials Engineering and Performance*, 12 (2003) 288.
- [4] M. Scherge, K. Pöhlmann, A. Gervé, *Wear*, 254 (2003) 801-817.
- [5] E. W. Schneider, D.H. Blossfeld, *Nuclear Instruments and Methods in Physics Research A*, 505 (2003) 559-563.
- [6] E.W. Schneider, D.H. Blossfeld, SAE International, 2004-01-2917, 2004.
- [7] B. R. Lawn, E. R. Fuller, *Journal of Materials Science*, 10 (1975) 2016-2024.
- [8] R. F. Cook, G. M. Pharr, *Journal of the American Ceramic Society*, 73 (1990) 787-817.
- [9] B. R. Lawn, D. B. Marshall, *Journal of Materials Research*, 89 (1975) 435-451.
- [10] B. R. Lawn, M. V. Swain, K. Phillips, *Journal of Materials Science*, 10 (1975) 1236-1239.
- [11] N. P. Suh, *Tribophysics*, Prentice Hall Inc., Englewood Cliffs, New Jersey, 1986.
- [12] D. Tabor, *Proceedings of the Royal Society of London*, 192 (1948) 247-274.
- [13] B. R. Lawn, R. Wilshaw, *Journal of Materials Science*, 10 (1975) 1049-1081.
- [14] B. R. Lawn, M.V. Swain, *Journal of Materials Science*, 10 (1975) 113-122.
- [15] D. Tabor, *The Hardness of Metals*, Oxford University Press, NY, 2000.
- [16] Karl-Heinz Zum Garh, *Microstructure and Wear of Materials*, Elsevier, NY, 1987.
- [17] W.C. Oliver, G.M. Pharr, *Journal of Materials Research*, 7 (1992) 1564-1583.
- [18] Y.T. Cheng, C.M. Cheng, *Materials Science and Engineering R*, 44 (2004) 91-149.

- [19] B.R. Lawn, *Journal of Applied Physics*, 39 (1968) 4828-4836.
- [20] A. Arora, D.B. Marshall, B.R. Lawn, M.V. Swain, *Journal of Non-Crystalline Solids*, 31 (1979) 415-428.
- [21] G.R. Anstis, P. Chantikul, D.B. Marshall, B.R. Lawn, *Journal of the American Ceramic Society*, 64 (1981) 533-538.
- [22] V. Milekhine, M.I. Onsøyen, J.K. Solberg, T. Skaland, *Intermetallics*, 10 (2002) 743-750.
- [23] C. B. Ponton, R.D. Rawlings, *Materials Science & Technology*, 5 (1989) 865-872.
- [24] A. R. Riahi, A. T. Alpas, *Materials Science and Engineering A*, 441 (2006) 326-330.
- [25] B.R. Lawn, A. G. Evans, D. B. Marshall, *Journal of the American Ceramic Society*, 63 (1980) 574-581.
- [26] M. Dienwiebel, K. Pöhlmann, M. Scherge, *Tribology International*, 40 (2007) 1597-1602.
- [27] M. Chen, A. T. Alpas, *Wear*, 265 (2008) 186-195.
- [28] S. K. Dey, T. A. Perry, A. T. Alpas, *Wear* (2009), doi:10.1016/i.wear.2008.11.011 (article in press).
- [29] M. Chen, X. Meng-Burany, T. A. Perry, A. T. Alpas, *Acta Materialia*, 56 (2008) 5605-5616.
- [30] S. Xia, Y. Qi, T. Perry, K. S. Kim, *Acta Materialia*, 57 (2009) 695-707.
- [31] B. E. Slattery, T. Perry, A. Edrisky, *Materials Science and Engineering A*, 512 (2009) 76-81.
- [32] W. Weibull, *Ingeniörsvetenskapsakademiens Handlingar Nr 151* (1939) 1-45.
- [33] P. Kittl, G. Díaz, *Res Mechanica* 24 (1988) 99-207.

- [34] J. A. Kies, NRL Report 5093, Naval Research Lab., Washington DC, 1958.
- [35] A. F. Whitehouse, T. W. Clyne, *Acta Metallurgica et Materialia*, 41 (1993) 1701-1711.
- [36] C. A. Lewis, W. M. Stobbs, P. J. Withers, *Materials Science and Engineering A*, 171 (1993) 1-11.
- [37] W. H. J. Hunt, J. R. Brockenbrough, P. E. Magnusen, *Scripta Metallurgica et Materialia*, 25 (1991) 15-20.
- [38] J. Llorca, A. Martin, J. Ruiz, M. Elices, *Metallurgical Transactions A*, 24 (1993) 1575-1588.
- [39] D. Lloyd, *Acta Metallurgica et Materialia*, 39 (1991) 59-71.
- [40] Y. Brechet, J. D. Embury, S. Tao, L. Luo, *Acta Metallurgica et Materialia*, 39 (1991) 1781-1786.
- [41] P. M. Singh, J. J. Lewandowski, *Metallurgical Transactions A*, 24 (1993) 2531-2543.
- [42] J. J. Lewandowski, C. Liu, W. H. Hunt, *Materials Science and Engineering A*, 107 (1989) 241-255.
- [43] C. A. Lewis, P. J. Withers, *Acta Metallurgica et Materialia*, 43 (1995) 3685-3699.
- [44] C. H. Caceres, J. R. Griffiths, *Acta Materialia*, 44 (1996) 25-33.
- [45] R. Danzer, P. Supancic, J. Pascual, T. Lube, *Engineering Fracture Mechanics*, 74 (2007) 2919-2932.
- [46] A. George, *Properties of Crystalline Silicon*, Ed. 20 (INSPEC, London 1999), pp. 104-107.
- [47] R. J. Needs, A. Mujica, *Physical Review B*, 51 (1996) 9652-9670.

- [48] J. Crain, G. J. Ackland, J. R. Maclean, R. O. Plitz, P. D. Hatton, G. S. Pawley, *Physical Review B*, 50 (1994) 13043-13046.
- [49] R. O. Plitz, J. R. Maclean, S. J. Clark, G. J. Ackland, P. D. Hatton, J. Crain, *Physical Review B*, 52 (1995) 4072-4085.
- [50] J. Z. Hu, L. D. Merkle, C. S. Menoni, I. L. Spain, *Physical Review B*, 34 (1986) 4679-4684.
- [51] J. E. Bradby, J. S. Williams, J. Wong-Leung, M. V. Swain, P. Munroe, *Applied Physics Letters*, 77 (2000) 3749-3751.
- [52] U. Dahmen, C. J. Hetherington, P. Pirouz, K. H. Westmacott, *Scripta Materialia*, 23 (1989) 269-272.
- [53] A. Kailer, Y. G. Gogotsi, K. G. Nickel, *Journal of Applied Physics*, 81 (1997) 3057-3063.
- [54] A. Kovalchenko, Y. Gogotsi, V. Domnich, A. Erdemir, *Tribology Transactions*, 45 (2002) 372-380.
- [55] D. Ge, V. Domnich, Y. Gogotsi, *Journal of Applied Physics*, 93 (2003) 2418-2423.
- [56] M. Tachi, S. Suprijadi, S. Arai, H. Saka, *Philosophical Magazine Letters*, 82 (2002) 133-139.
- [57] Y. Q. Wu, G. Y. Shi, Y. B. Xu, *Journal of Materials Research*, 14 (1999) 2399-2401.
- [58] J. E. Bradby, J. S. Williams, J. Wong-Leung, M. V. Swain, P. Munroe, *Journal of Materials Research*, 16 (2001) 1500-1507.
- [59] A. Shimatani, T. Nango, Suprijadi, H. Saka, *Materials Research Society Symposium Proceedings*, 522 (1998) 71-76.

- [60] Jae-il Jang, S. Wen, M. J. Lance, I. M. Anderson, G. M. Pharr, *Materials Research Society Symposium Proceedings*, 795 (2004) 313-318.
- [61] J. P. Hirth, J. Lothe, *Theory of Dislocations*, Ed. 20, Wiley, 1982.
- [62] D. J. H. Cockayne, I. L. F. Ray, M. J. Whelan, *Philosophical Magazine*, 20 (1969) 1265-1270.
- [63] P. B. Hirsch, *Materials Research Society Symposium Proceedings*, (1981) 257-271.
- [64] P. Pirouz, *Scripta Materialia*, 21 (1987) 1463-1468.
- [65] K. Wessel, H. Alexandre, *Philosophical Magazine*, 35 (1977) 1523-1536.
- [66] J. Samuels, P. Pirouz, S. G. Roberts, P. D. Warren, P. B. Hirsch, *Microscopy of Semiconducting Materials*, *Proceedings of the Royal Microscopical Society Conference*, (1985) 49-54.
- [67] S. G. Roberts, P. Pirouz, P. B. Hirsch, *Journal of Materials Science*, 20 (1985) 1739-1747.
- [68] A. Kelly, W. R. Tyson, A. H. Cottrell, *Philosophical Magazine*, 15 (1967) 567-586.
- [69] S. J. Burns, *Scripta Materialia*, 20 (1986) 1489-1494.
- [70] J. R. Rice, R. Thompson, *Philosophical Magazine*, 29 (1974) 73-97.
- [71] S. M. Ohr, *Scripta Materialia*, 20 (1986) 1501-1505.
- [72] J. C. M. Li, *Scripta Materialia*, 20 (1986) 1477-1482.
- [73] P. M. Anderson, J. R. Rice, *Scripta Materialia*, 20 (1986) 1467-1472.
- [74] G. C. Rybicki, P. Pirouz, *NASA Technical Paper 2863*, 1988.
- [75] S. G. Roberts, P. Pirouz, P. B. Hirsch, *Journal De Physique*, 44 (1983) 75-83.
- [76] M. Tachi, S. Suprijadi, S. Arai, H. Saka, *Philosophical Magazine Letters*, 82 (2002) 133-139.

- [77] J. Samuels, P. Pirouz, S. G. Roberts, P. D. Warren, P. B. Hirsch, Institute of Physics: Conference, 76 (1985) 49-54.
- [78] H. Saka, S. Abe, Materials Science and Engineering A, 234 (1997) 552-554.
- [79] D. Ge, V. Domnich, Y. Gogotsi, Journal of Applied Physics, 93 (2003) 2418-2423.
- [80] T. Suzuki, T. Ohnuma, Philosophical Magazine A, 74 (1996) 1073-1084.
- [81] F. C. R. Hernandez, J. H. Sokolowski, J. J. C. Rivera, Advanced Engineering Materials, 9 (2007) 46-51.
- [82] R. Biswas, A. M. Bouchard, W. A. Kamitakahara, G. S. Grest, C. M. Soukoulis, Physical Review Letters, 60 (1988) 2280-2283.
- [83] J. S. Kasper, S. H. Richards, Acta Crystallographica, 17 (1964) 752-756.
- [84] R. J. Kobliska, S. A. Solin, M. Selders, R. K. Chang, R. Alben, M. F. Thorpe, D. Weaire, Physical Review Letters, 29 (1972) 725-728.
- [85] J. M. Besson, E. H. Mokhtari, J. Gonzalez, G. Weill, Physical Review Letters, 59 (1987) 473-476.
- [86] G. Weill, J. L. Mansot, G. Sagon, C. Carlone, J. M. Besson, Semiconductor Science and Technology, 4 (1989) 280-282.
- [87] V. G. Eremenko, V. I. Nikitenko, Physica Status Solidi A, 14 (1972) 317-330.
- [88] P. Pirouz, R. Chaim, U. Dahmen, K. H. Westmacott, Acta Metallurgica et Materialia 38 (1990) 313-322.
- [89] U. Dahmen, K. H. Westmacott, P. Pirouz, R. Chaim, Acta Metallurgica et Materialia, 38 (1990) 323-328.
- [90] R. J. Kobliska, S. A. Solin, Physical Review B, 8 (1973) 3799-3802.

- [91] X. S. Zhao, Y. R. Ge, J. Schroeder, P. D. Persans, *Applied Physics Letters*, 65 (1994) 2033-2035.
- [92] V. Domnich, Y. Gogotsi, *Reviews on Advanced Materials Science*, 3 (2002) 1-36.
- [93] D. Ge, V. Domnich, Y. Gogotsi, *Journal of Applied Physics*, 95 (2004) 2725-2731.
- [94] M. G. S. Naylor, T. F. Page, *Journal of Microscopy*, 130 (1983) 345-360.
- [95] S. K. Arguirova, V. Orlov, W. Seifert, J. Reif, H. Richter, *European Physics Journal -Applied Physics*, 27 (2004) 279-283.
- [96] B.R. Lawn, J.S. Williams, M.V. Swain, *Physica Status Solidi A*, 2 (1970) 7-29.
- [97] Q. Ma, D. R. Clarke, *Journal of Materials Research*, 10 (1995) 853-863.
- [98] I. Chasiotis, S. W. Cho, K. Jonnalagadda, *Journal of Applied Mechanics (Trans. ASME)*, 73 (2006) 714-722.
- [99] G. Lucazeau, L. Abello, *Journal of Materials Research*, 12 (1997) 2262-2273.
- [100] M. M. Khayyat, G. K. Banini, D. G. Hasko, M. M. Chaudhri, *Journal of Physics D: Applied Physics*, 36 (2003) 1300-1307.
- [101] S.D. Antolovich, B.F. Antolovich, *An introduction to fracture mechanics, ASM handbook, fatigue and fracture* 19 (1996) 371-380.
- [102] K. L. Johnson, *Journal of the Mechanics and Physics of Solids*, 18 (1970) 115-126.
- [103] G. T. A. Kovacs, *Micromachine Transducers Sourcebook*, McGraw Hill, 26 (1998).
- [104] K. Tanaka, *Journal of Materials Science*, 22 (1987) 1501-1508.
- [105] K. P. J. Williams, G. D. Pitt, J. E. Smith, A. Whitley, D. N. Batchelder, I. P. Hayward, *Journal of Raman Spectroscopy*, 25 (1994) 131-138.
- [106] M. Bowden, D. J. Gardiner, *Applied Spectroscopy*, 51 (1997) 1405-1409.

[107] M. Durandurdu, D. A. Drabold, *Physical Review B* 67 (2003) 212101(1)-212101(3).

[108] Jae-il Jang, S. Wen, M. J. Lance, I. M. Anderson, G. M. Pharr, *Materials Research Society Symposium Proceedings*, 795 (2004) 313-318.

APPENDIX

Solutions for the stress field in an elastic half-space under normal point loading were first derived by J. Boussinesq in 1885. **Fig. 2.2** has been defined in terms of cylindrical coordinates. If the displacement components of an infinitesimal element along the r , θ and z axes are denoted by u , v and w , respectively, the v component is zero and the u and w components are independent of θ due to symmetry. Consequently, the shear stresses $\sigma_{z\theta}$ and $\sigma_{r\theta}$ are also equal to zero. Other stress components are given by Boussinesq as [11],

$$\begin{aligned}\sigma_{rr} &= \frac{P}{2\pi} \left[(1-2\nu) \frac{1}{r^2} - \frac{z}{r^2(r^2+z^2)^{\frac{1}{2}}} - \frac{3r^2z}{(r^2+z^2)^{\frac{5}{2}}} \right] \\ \sigma_{\theta\theta} &= \frac{(1-2\nu)P}{2\pi} \left[-\frac{1}{r^2} + \frac{z}{r^2(r^2+z^2)^{\frac{1}{2}}} + \frac{z}{(r^2+z^2)^{\frac{3}{2}}} \right] \\ \sigma_{zz} &= -\frac{3P}{2\pi} \frac{z^3}{(r^2+z^2)^{\frac{5}{2}}} \\ \sigma_{rz} &= -\frac{3P}{2\pi} \frac{rz^2}{(r^2+z^2)^{\frac{5}{2}}}\end{aligned}\tag{A1}$$

The displacements are given as [14],

$$\begin{aligned}u &= \frac{(1-2\nu)(1+\nu)P}{2\pi Er} \left[\frac{z}{(r^2+z^2)^{\frac{1}{2}}} - 1 + \frac{1}{1-2\nu} \frac{r^2z}{(r^2+z^2)^{\frac{3}{2}}} \right] \\ w &= \frac{P}{2\pi E} \left[\frac{2(1-\nu^2)}{(r^2+z^2)^{\frac{1}{2}}} + \frac{(1+\nu)z^2}{(r^2+z^2)^{\frac{3}{2}}} \right]\end{aligned}\tag{A2}$$

The principal shear stresses are given by [14],

$$\sigma_{13} = \frac{1}{2}(\sigma_{11} - \sigma_{33})$$

$$\sigma_{12} = \frac{1}{2}(\sigma_{11} - \sigma_{22})$$

(A3)

$$\sigma_{23} = \frac{1}{2}(\sigma_{22} - \sigma_{33})$$

inclined at 45° to the principal directions. Lastly, the magnitude of the component of hydrostatic compression is given by,

$$p = -\frac{1}{3}(\sigma_{11} + \sigma_{22} + \sigma_{33})$$

(A4)

VITA AUCTORIS

NAME: Sandeep Bhattacharya

PLACE OF BIRTH: Calcutta, West Bengal, India

YEAR OF BIRTH: 1982

EDUCATION: Ramakrishna Mission Vidyapith, Purulia, West Bengal, India
1998-2003
Jadavpur University, Calcutta, West Bengal, India
2003-2007; B.E. (First Class-Honours)
University of Windsor, Windsor, Windsor, Ontario, Canada
2007-2009; M.A.Sc.

Publication:

S. Bhattacharya, A. R. Riahi and A. T. Alpas, Indentation-induced subsurface damage in silicon particles of Al-Si alloys, submitted to Materials Science and Engineering: A, 2009.